

**REPUBLIC OF TURKEY
YILDIZ TECHNICAL UNIVERSITY
GRADUATE SCHOOL OF NATURAL AND APPLIED SCIENCES**

**SYNTHESIS OF ALUMINIUM OXIDE NANOPARTICLES
AND IRON BASED MAGNETIC ALUMINIUM OXIDE
NANOCOMPOSITES BY SOLUTION COMBUSTION METHOD
AND APPLICATIONS**



MERVE PEHLIVAN

**MSc. THESIS
DEPARTMENT OF CHEMICAL ENGINEERING
PROGRAM OF CHEMICAL ENGINEERING**

**ADVISER
PROF.DR. BELMA ÖZBEK
CO-ADVISER
PROF.DR. SUNULLAH ÖZBEK**

İSTANBUL, 2018

**REPUBLIC OF TURKEY
YILDIZ TECHNICAL UNIVERSITY
GRADUATE SCHOOL OF NATURAL AND APPLIED SCIENCES**

**SYNTHESIS OF ALUMINIUM OXIDE NANOPARTICLES
AND IRON BASED MAGNETIC ALUMINIUM OXIDE
NANOCOMPOSITES BY SOLUTION COMBUSTION METHOD
AND APPLICATIONS**

A thesis submitted by Merve PEHLIVAN in partial fulfilment of the requirements for the degree of **MASTER OF SCIENCE** is approved by the committee on 19.06.2018 in Department of Chemical Engineering, Program of Chemical Engineering.

Thesis Adviser

Prof. Dr. Belma ÖZBEK
Yildiz Technical University

Co- Adviser

Prof. Dr. Sunullah ÖZBEK
İstanbul Gedik University

Approved By the Examining Committee

Prof. Dr. Belma ÖZBEK
Yildiz Technical University

Prof. Dr. Dilek KAZAN
Marmara University

Assist. Prof. Dr. Emel AKYOL
Yildiz Technical University



This study was supported by the Scientific and Technological Research Council of Turkey (TUBITAK), Grant No: **International ERA.Net RUS Plus - 315M495**.

ACKNOWLEDGEMENTS

I would like to express my deepest appreciation to all those who provided me the possibility to complete this work. I would never have been completed this work without guidance of my advisers and support from my family.

First and foremost, I give special sincerest gratitude to my thesis adviser Prof. Dr. Belma ÖZBEK who has shown attitude of motivating, insight and continuous guidance. Secondly, a special gratitude I give to my co-adviser Prof. Dr. Sunullah ÖZBEK. He provided me with every bit of his assistance, knowledge and expertise when I needed. His patience and kindness have always encouraged me to carry out this study.

The present study was carried at İstanbul Gedik University and supported by the Scientific and Technological Research Council of Turkey (TUBITAK), Grant No: International ERA.Net RUS Plus-315M495. I would like to express my gratitude to TUBITAK for supporting this project.

I would like to thank Research Assistant Sinem ŞİMŞEK KEKEVİ who always supported me during laboratory part of the work. Moreover, she discussed me new ideas and expanded my horizon.

Finally, I would like to thank my family and friends who have always supported and motivated me throughout the work.

June, 2018

Merve PEHLİVAN

TABLE OF CONTENTS

	Page
LIST OF SYMBOLS	viii
LIST OF ABBREVIATIONS.....	ix
LIST OF FIGURES	xi
LIST OF TABLES.....	xiv
ABSTRACT.....	xvi
ÖZET	xviii
CHAPTER 1	
INTRODUCTION	1
1.1 Literature Review.....	1
1.2 Objective of the Thesis	2
1.3 Hypothesis.....	2
CHAPTER 2	
NANOTECHNOLOGY.....	4
2.1 Nanoscale Properties.....	5
2.1.1 Optical Properties.....	5
2.1.2 Chemical Reactivity.....	5
2.1.3 Mechanical Strength	5
2.1.4 Melting Point	5
2.1.5 Quantum Confinement.....	6
2.2 Synthesis Methods of Metal Oxide Nanoparticles.....	6
2.2.1 Top-down Approaches.....	7
2.2.2 Bottom-up Approaches	8
CHAPTER 3	
ALUMINIUM OXIDE	17
3.1 Crystalline Structure and Types of Aluminium Oxide	17
3.2 Aluminium Oxide, Properties and Applications.....	20
3.3 Aluminium Oxide Nanoparticles, Properties and Applications.....	22
CHAPTER 4	
MAGNETIC NANOPARTICLES.....	23

4.1	Iron Based Magnetic Nanoparticles, Properties and Applications	24
4.2	Iron Based Magnetic Aluminium Oxide Nanocomposites, Properties and Applications	26
 CHAPTER 5		
ADSORPTION		29
5.1	Adsorption Types.....	32
5.2	Adsorption Isotherm Models	33
5.2.1	Freundlich Isotherm Model.....	33
5.2.2	Langmuir Isotherm Model	34
5.2.3	Temkin Isotherm Model	35
5.3	Adsorption Kinetic Models.....	35
5.3.1	First Order Reaction Model	35
5.3.2	Pseudo-First Order Reaction Model	36
5.3.3	Second Order Reaction Model.....	36
5.3.4	Pseudo-Second Order Reaction Model.....	37
5.3.5	Elovich Model.....	37
5.3.6	Intra-particle Diffusion Model.....	38
5.4	Types of Adsorption Isotherms.....	38
5.4.1	Classification of Gas Physisorption Isotherms	38
5.5	Dye Removal by Adsorption	40
 CHAPTER 6		
EXPERIMENTAL DESIGN		41
6.1	Response Surface Methodology	42
6.2	Box-Behnken Design Method.....	43
 CHAPTER 7		
LITERATURE SURVEY		45
7.1	Literature Survey on Aluminium Oxide Nanoparticles Synthesis by Solution Combustion Method	45
7.2	Literature Survey on Iron Based Magnetic Aluminium Oxide Nanocomposites Synthesis by Solution Combustion Method.....	51
7.3	Literature Survey on Reactive Blue 19 Dye Removal by Adsorption.....	54
 CHAPTER 8		
MATERIALS AND METHODS.....		61
8.1	Materials	61
8.1.1	Chemicals.....	61
8.1.2	Apparatus	61
8.2	Experimental Studies	64
8.2.1	Synthesis of Aluminium Oxide Nanoparticles	64
8.2.2	Synthesis of Iron Based Magnetic Aluminium Oxide Nanocomposites	67
8.2.3	Adsorption Studies.....	71
8.3	Characterization Studies	72
8.3.1	X-Ray Diffraction Analysis	73
8.3.2	Scanning Electron Microscope	73
8.3.3	Thermogravimetric/Differential Thermal Analysis	75

8.3.4	Surface Area and Porosity Analysis	75
8.3.5	UV-Vis Spectrophotometer	76
8.4	Calibration Data for Reactive Blue 19 Dye	77
 CHAPTER 9		
RESULTS AND DISCUSSION		79
9.1	Characterization Studies of Synthesized Aluminium Oxide Nanoparticles ...	79
9.1.1	X-ray Diffraction Analysis	80
9.1.2	Scanning Electron Microscopy Analysis	82
9.1.3	Thermogravimetric/Differential Thermal Analysis	85
9.2	Characterization Studies of Iron Based Magnetic Aluminium Oxide Nanocomposites	89
9.2.1	X-ray Diffraction Analysis	90
9.2.2	Scanning Electron Microscopy Analysis	95
9.2.3	Scanning Electron Microscopy (SEM) – Energy Dispersive X-ray Spectroscopy (EDS) Analysis	97
9.2.4	Thermogravimetric/Differential Thermal Analysis	99
9.2.5	Surface Area and Porosity Analysis	106
9.3	Reactive Blue 19 Dye Removal by Iron Based Magnetic Aluminium Oxide Nanocomposites	108
9.3.1	Box-Behnken Design Method Analysis	109
9.3.2	Adsorption Isotherm Models	114
9.3.3	Adsorption Kinetic Models	115
 CHAPTER 10		
CONCLUSIONS		118
REFERENCES		127
 APPENDIX-A		
SCANNING ELECTRON MICROSCOPY IMAGES		136
 APPENDIX-B		
DATA OF ADSORPTION ISOTHERM MODELS		139
 APPENDIX-C		
DATA OF ADSORPTION KINETIC MODELS		140
CURRICULUM VITAE		143

LIST OF SYMBOLS

A_T	Temkin isotherm equilibrium binding constant (L/g)
b	Langmuir adsorption constant (L/mg)
b_T	Temkin constant (J/mol)
c_0	Initial concentration of adsorbate (mg/L)
c_e	Equilibrium concentration of adsorbate in the solution (mg/L)
c_i	Constant related to layer thickness ($\text{mg}\cdot\text{g}^{-1}$)
c_t	Concentration at contact time (mg/L)
k	First order adsorption rate constant
k_1	Pseudo-first order adsorption rate constant
k_2	Second order adsorption rate constant
k_f	Freundlich affinity coefficient ($\text{mg}^{1-1/n}\cdot\text{L}^{1/n}\cdot\text{g}^{-1}$),
k_i	Intra-particle diffusion rate constant ($\text{mg}\cdot\text{g}^{-1}\cdot\text{min}^{-2}$)
k_{p2}	Pseudo-second order adsorption rate constant
m	Mass of adsorbent (g)
n	Freundlich exponential coefficient
q_e	Equilibrium adsorbed concentration (mg/g)
q_m	Monolayer adsorption capacity of the adsorbent (mg/g)
q_t	Adsorption capacity of any time (mg/g)
R	Ideal gas constant (J/mol.K)
$R\%$	Removal rate (%)
R^2	Regression coefficient
T	Temperature
T_{ig}	Ignition temperature ($^{\circ}\text{C}$)
T_m	Maximum flame temperature
V	Volume (L)
α	Initial adsorption rate ($\text{mg}\cdot\text{g}^{-1}\cdot\text{min}$)
β	Constant related to extent of surface coverage and the activation energy ($\text{g}\cdot\text{mg}^{-1}$)
σ	Standard deviation

LIST OF ABBREVIATIONS

0D	Zero Dimensional
1D	One Dimensional
2D	Two Dimensional
AC	Activated Carbon
BET	Brunauer Emmet Teller
Conc.	Concentration
CS	Combustion Synthesis
CS-MHAP	Chitosan Coated Magnetic Hydroxyapatite Nanoparticles
EDS	Energy Dispersive X-ray Spectroscopy
SC-FA-U1	Iron Based Magnetic Aluminium Oxide Synthesized by Urea Fuel
SC-FA-U2	Iron Based Magnetic Aluminium Oxide Synthesized by Urea Fuel
SC-FA-U2-H	Iron Based Magnetic Aluminium Oxide Synthesized by Urea Fuel, Calcined and Reduced
SC-FA-G1	Iron Based Magnetic Aluminium Oxide Synthesized by Glycine Fuel
SC-FA-G2	Iron Based Magnetic Aluminium Oxide Synthesized by Glycine Fuel
SC-FA-G2-H	Iron Based Magnetic Aluminium Oxide Synthesized by Glycine Fuel, Calcined and Reduced
SC-FA-S1	Iron Based Magnetic Aluminium Oxide Synthesized by Sucrose Fuel
SC-FA-S2	Iron Based Magnetic Aluminium Oxide Synthesized by Sucrose Fuel
SC-FA-S2-H	Iron Based Magnetic Aluminium Oxide Synthesized by Sucrose Fuel, Calcined and Reduced
FT-IR	Fourier Transform Infra-Red
HAP	Hydroxyapatite
IUPAC	International Union of Pure and Applied Chemistry
MRI	Magnetic Resonance Imaging
MW	Microwave
MWCNT	Multi-Walled Carbon Nanotube
MWS	Modified Wheat Straw
NWS	Natural Wheat Straw
OP	Orange Peel
RB19	Reactive Blue 19 Dye
RSM	Response Surface Methodology
SC-A-U1	Aluminium Oxide Synthesized by Urea Fuel
SC-A-U2	Aluminium Oxide Synthesized by Urea Fuel
SC-A-G1	Aluminium Oxide Synthesized by Glycine Fuel
SC-A-G2	Aluminium Oxide Synthesized by Glycine Fuel
SCS	Solution Combustion Synthesis
SEM	Scanning Electron Microscopy

SHS	Self-propagating High-temperature Synthesis
SOP	Sodium Hydroxide-treated Orange Peel
SPR	Surface Plasmon Resonance
Stoich.	Stoichiometric
SWCNT	Single-Walled Carbon Nanotube
TEM	Transmission Electron Microscopy
Temp.	Temperature
TG/DSC	Thermogravimetric and Differential Scanning Calorimetry
TG/DTA	Thermogravimetric and Differential Thermal Analysis
UV-Vis	Ultraviolet-Visible Spectrophotometer
XRD	X-Ray Diffraction



LIST OF FIGURES

	Page
Figure 2.1 Schematic representation of top down and bottom up approaches	7
Figure 2.2 Precursor concentration versus time of nanoparticles prepared by solution phase methods	8
Figure 2.3 The reactions and processing steps of sol-gel method	10
Figure 2.4 Schematic diagram of the autoclave in hydrothermal synthesis method	11
Figure 2.5 Schematic representation of spray pyrolysis method	12
Figure 2.6 Volume combustion mode of synthesis of a) $\text{Ca}_3\text{Al}_2\text{O}_6$ and b) Fe_2O_3	14
Figure 2.7 Self-propagating combustion mode of nickel nitrite-glycine a) reaction systems and b) time-temperature profile	15
Figure 3.1 The crystal structure of a) $\alpha\text{-Al}_2\text{O}_3$ and b) $\gamma\text{-Al}_2\text{O}_3$ with colour code	18
Figure 3.2 Thermal transformation of various aluminium hydroxides	19
Figure 3.3 X-ray diffraction peaks of a) $\chi\text{-Al}_2\text{O}_3$, b) $\kappa\text{-Al}_2\text{O}_3$, c) $\gamma\text{-Al}_2\text{O}_3$, d) $\delta\text{-Al}_2\text{O}_3$, e) $\theta\text{-Al}_2\text{O}_3$, f) $\eta\text{-Al}_2\text{O}_3$ and g) $\alpha\text{-Al}_2\text{O}_3$	20
Figure 3.4 Acidic and basic site in aluminium oxide surface	21
Figure 4.1 Schematic illustration of the coercivity and particle size relations	24
Figure 4.2 Alignment of the magnetic states	25
Figure 4.3 Scheme of a) magnetic particles design workflow and b) modification of magnetic particles	26
Figure 5.1 Basic terms of adsorption	29
Figure 5.2 Schematic pores classification from IUPAC	32
Figure 5.3 Classification of vapour adsorption isotherms from IUPAC	39
Figure 6.1 The flow chart of experimental design process	42
Figure 6.2 a) Box-Behnken design derived from a cube and b) Box-Behnken representation of 2^2 factorial design.....	44
Figure 8.1 Protherm Furnace.....	62
Figure 8.2 Protherm Tube Furnace.....	63
Figure 8.3 The images of synthesized samples before and after calcination a) SC-A-U1, b) SC-A-U2, c) SC-A-G1 and d) SC-A-G2	66

Figure 8.4	Magnetic attraction of SC-FA-G2	70
Figure 8.5	Magnetic attraction of SC-FA-G2 after adsorption process with commercial magnet.....	72
Figure 8.6	Equipment for X-ray Diffraction Analysis	73
Figure 8.7	Scanning Electron Microscope (SEM)	74
Figure 8.8	Scanning Electron Microscopy-Energy Dispersive X-ray Spectroscopy (SEM-EDS).....	74
Figure 8.9	Thermogravimetric/Differential Thermal Analyzer (TG/DTA)	75
Figure 8.10	UV-Vis Spectrophotometer	76
Figure 8.11	Calibration data of Reactive Blue 19 Dye.....	78
Figure 9.1	XRD patterns of synthesized samples of a) SC-A-U1, b) SC-A-U2, c) SC-A-G1 and d) SC-A-G2.....	81
Figure 9.2	SEM microscopy images of SC-A-U1	83
Figure 9.3	SEM microscopy images of SC-A-U2	83
Figure 9.4	SEM microscopy images of SC-A-G1	84
Figure 9.5	SEM microscopy images of SC-A-G2	84
Figure 9.6	a) TG/DTG and b) DTA curves of SC-A-U1	86
Figure 9.7	a) TG/DTG and b) DTA curves of SC-A-U2	87
Figure 9.8	a) TG/DTG and b) DTA curves of SC-A-G1	88
Figure 9.9	a) TG/DTG and b) DTA curves of SC-A-G2	89
Figure 9.10	XRD patterns of synthesized samples of a) SC-FA-U1, b) SC-FA-U2 and c) SC-FA-U2-H.....	91
Figure 9.11	XRD patterns of synthesized samples of a) SC-FA-G1, b) SC-FA-G2 and c) SC-FA-G2-H.....	93
Figure 9.12	XRD patterns of synthesized samples of a) SC-FA-S1, b) SC-FA-S2 and c) SC-FA-S2-H	94
Figure 9.13	SEM microscopy images of SC-FA-U2-H.....	95
Figure 9.14	SEM microscopy images of SC-FA-G2-H.....	96
Figure 9.15	SEM microscopy images of SC-FA-S2-H	97
Figure 9.16	SEM micrographs and EDS analysis of synthesized samples of a) SC-FA-U2-H, b) SC-FA-G2-H and c) SC-FA-S2-H.....	98
Figure 9.17	a) TG/DTG and b) DTA curves of SC-FA-U1	100
Figure 9.18	a) TG/DTG and b) DTA curves of SC-FA-U2	101
Figure 9.19	a) TG/DTG and b) DTA curves of SC-FA-G1	102
Figure 9.20	a) TG/DTG and b) DTA curves of SC-FA-G2	103
Figure 9.21	a) TG/DTG and b) DTA curves of SC-FA-S1	104
Figure 9.22	a) TG/DTG and b) DTA curves of SC-FA-S2	105

Figure 9.23 a) The adsorption-desorption isotherms and b) Pore volume analysis by BJH desorption method of SC-FA-G2	107
Figure 9.24 Predicted data versus experimental data of RB19 dye removal (%).....	111
Figure 9.25 Response surface plot for the combined effects of pH and temperature on RB19 dye removal (%)	112
Figure 9.26 Response surface plot for the combined effects of pH and adsorbent amount on RB19 dye removal (%)	113
Figure 9.27 Response surface plot for the combined effects of temperature and adsorbent amount on RB19 dye removal (%).....	113
Figure 9.28 Langmuir adsorption isotherm model data of RB19 dye removal onto SC-FA-G2	115
Figure 9.29 The linearized pseudo-second order kinetic model at various adsorbent amounts of a) 50 mg, b) 200 mg and c) 400 mg	117
Figure A.1 SEM microscopy images of SC-FA-U1	136
Figure A.2 SEM microscopy images of SC-FA-U2	136
Figure A.3 SEM microscopy images of SC-FA-G1	137
Figure A.4 SEM microscopy images of SC-FA-G2	137
Figure A.5 SEM microscopy images of SC-FA-S1	137
Figure A.6 SEM microscopy images of SC-FA-S2.....	138

LIST OF TABLES

	Page
Table 2.1	The components used in solution combustion method 13
Table 3.1	Types of aluminium hydroxides 19
Table 5.1	The advantages and disadvantages of various removal methods 30
Table 5.2	Adsorption process in water treatment 31
Table 5.3	IUPAC pore size classifications 32
Table 5.4	Differences between physical and chemical adsorption 33
Table 7.1	Various studies on synthesis of aluminium oxide nanoparticles by solution combustion method 49
Table 7.2	Various studies on synthesis of iron based magnetic aluminium oxide nanocomposites by solution combustion method 53
Table 7.3	Various studies on the adsorption of Reactive Blue 19 dye onto various adsorbents 58
Table 8.1	The oxidizer and fuel amounts and stoichiometric fuel ratios for aluminium oxide nanoparticles synthesized by solution combustion method 64
Table 8.2	The oxidizer and fuel amounts and stoichiometric fuel ratios for iron based magnetic aluminium oxide nanocomposites synthesized by solution combustion method 68
Table 8.3	Specifications of the synthesized samples 69
Table 8.4	Magnetic attraction of the synthesized samples 70
Table 8.5	Reactive Blue 19 dye calibration curve data 77
Table 9.1	The compositional analysis of synthesized samples of SC-FA-U2-H, SC-FA-G2-H and SC-FA-S2-H obtained from EDS analysis 99
Table 9.2	Surface area and porosity analysis of SC-FA-G2 108
Table 9.3	The parameters chosen for experimental design of RB19 dye adsorption 108
Table 9.4	Box-Behnken experimental design matrix and experimental responses of RB19 dye adsorption onto sample of SC-FA-G2 109
Table 9.5	ANOVA analysis data for the model developed 110
Table 9.6	The estimated parameters and statistical values of adsorption isotherm models 114

Table 9.7	The estimated parameters and statistical values of adsorption kinetic models	116
Table 10.1	Comparison of BET surface area and porosity analysis between the present study and Zhang et al.2012	121
Table 10.1	Present study on synthesis of aluminium oxide nanoparticles by solution combustion method.....	123
Table 10.2	Present study on synthesis of iron based magnetic aluminium oxide nanocomposites by solution combustion method.....	124
Table 10.3	Present study on the adsorption of Reactive Blue 19 dye	125
Table B.1	The data obtained from adsorption experiments of RB19 dye onto SC-FA-G2.....	139
Table C.1	The data obtained from adsorption kinetic experiments of RB19 dye onto 50 mg of SC-FA-G2	140
Table C.2	The data obtained from adsorption kinetic experiments of RB19 dye onto 200 mg of SC-FA-G2	141
Table C.3	The data obtained from adsorption kinetic experiments of RB19 dye onto 400 mg of SC-FA-G2	142

**SYNTHESIS OF ALUMINIUM OXIDE NANOPARTICLES
AND IRON BASED MAGNETIC ALUMINIUM OXIDE
NANOCOMPOSITES BY SOLUTION COMBUSTION METHOD
AND APPLICATIONS**

Merve PEHLIVAN

Department of Chemical Engineering

MSc. Thesis

Adviser: Prof. Dr. Belma ÖZBEK

Co-adviser: Prof. Dr. Sunullah ÖZBEK

In recent years, nanotechnology is attracting many researchers due to its increasing applications areas. Nanotechnology provides a variety of applications areas in many branches of science such as material science, chemical engineering, electrical engineering, pharmacology, organic chemistry, molecular biology, micro-fabrication and etc.

Aluminium oxide or alumina as a metal oxide is composed of aluminium and oxygen atoms and its chemical formula is indicated Al_2O_3 . Aluminium oxide has many crystal phases. However, alpha and gamma phase are the most common crystalline phases of aluminium oxide. The alpha phase aluminium oxide is known as the most stable one. The gamma phase aluminium oxide is mostly defined as amorphous and porous structure of aluminium oxide. Aluminium oxide nanoparticles are widely used in several applications due to their large surface area, homogeneous particle size distribution, spherical morphology and porous structure.

There are many novel application areas have appeared in nanotechnology by using magnetic nanoparticles. In particular, iron based aluminium oxide nanocomposites allows for many implementations because of its superior magnetic properties. These nanocomposites are utilized as catalyst, drug carrier, adsorbent and etc.

In the present study, aluminium oxide nanoparticles and iron based magnetic aluminium oxide nanocomposites were synthesized by solution combustion method using various fuels at various fuel amounts. Aluminium oxide nanoparticles were synthesized with two fuel types as urea and glycine at their various amounts, respectively. On the other hand, iron based magnetic aluminium oxide nanocomposites were synthesized with three fuel types as urea, glycine and sucrose at their various amounts, respectively. For the characterization studies of the synthesized samples, the following devices were used: X-Ray Diffraction (XRD), Scanning Electron Microscopy (SEM) and Energy Dispersive X-ray Spectroscopy (EDS), Thermogravimetric and Differential Thermal Analysis (TG/DTA) and Brunauer-Emmett-Teller (BET).

From the characterization studies, aluminium oxide nanoparticles and iron based magnetic aluminium oxide nanocomposites successfully synthesized by solution combustion method with nanoscale particle size. Moreover, iron based magnetic aluminium oxide nanocomposites synthesized by solution combustion method using stoichiometric amount of glycine as a fuel, have higher porous surface, small and homogeneously distributed particle size compared to other synthesized samples.

After evaluation of the data obtained from XRD and SEM analysis and magnetic attraction of the samples synthesized by solution combustion method, the sample synthesized using stoichiometric amount of glycine as a fuel (coded as SC-FA-G2) was chosen for further adsorption studies. For this purpose, Reactive Blue 19 (RB19) dye removal percentages at various process conditions were investigated onto SC-FA-G2 from aqueous solutions. The experimental set was planned by using a Design Expert 11.0 experimental design programme according to the Response Surface Methodology (RSM). According to Box-Behnken Design, 17 experiments were performed to investigate the effects of various process conditions. The effects of pH, temperature and adsorbent amount of SC-FA-G2 were investigated on the adsorption process, and a model was developed using the Box-Behnken methodology. Besides, the adsorption isotherm models and kinetic models were examined according to the data obtained from the adsorption experiments at the optimum process conditions obtained.

As a result, after evaluation of the experimental data obtained from the adsorption studies, RB19 dye removal percentage onto SC-FA-G2, was found as 100 % at pH of 2, 400 mg adsorbent amount/50 mL and 25 °C. The maximum adsorption capacity value (Q_{max}) for this sample was calculated as 55.248 mg/g.

Key words: Aluminium oxide nanoparticle, Iron based magnetic aluminium oxide nanocomposite, Solution combustion method, Response surface methodology, Dye removal

**ALÜMİNYUM OKSİT NANOPARTİKÜLLERİN VE DEMİR BAZLI
MANYETİK ALÜMİNYUM OKSİT NANOKOMPOZİTLERİN
ÇÖZELTİ YAKMA METODU İLE SENTEZİ
VE UYGULAMALARI**

Merve PEHLİVAN

Kimya Mühendisliği Anabilim Dalı

Yüksek Lisans Tezi

Tez Danışmanı: Prof. Dr. Belma ÖZBEK

Eş Danışman: Prof. Dr. Sunullah ÖZBEK

Son yıllarda, nanoteknolojinin kullanıldığı uygulama alanlarının giderek artması ile beraber nanoteknolojiye olan ilgi de artmıştır. Nanoteknoloji malzeme bilimi, kimya mühendisliği, elektrik mühendisliği, farmakoloji, organik kimya, moleküler biyoloji, mikro fabrikasyon vb. gibi birçok bilim dalında çeşitli uygulama alanları sunmaktadır.

Alüminyum oksit veya alümina olarak bilinen metal oksit, alüminyum ve oksijen atomlarından oluşmaktadır ve kimyasal formülü Al_2O_3 şeklindedir. Alüminyum oksitin birçok kristal fazı bulunmaktadır. Fakat, alfa ve gama fazı en çok bilinen alüminyum oksit kristal fazlarıdır. Alfa fazı alüminyum oksitin en stabil fazı olarak bilinir. Gama fazı ise daha çok amorf ve gözenekli bir yapıya sahip alüminyum oksit fazıdır. Alüminyum oksit nanopartikülleri, geniş yüzey alanına, homojen parçacık boyut dağılımına, küresel morfolojiye ve gözenekli yapıya sahip olması nedeni ile birçok uygulamada yaygın olarak kullanılmaktadır.

Nanoteknolojiye manyetik nanopartiküllerin katılmasıyla birçok yeni uygulama alanı oluşmuştur. Özellikle, demir bazlı alüminyum oksit nanokompozitlerinin üstün manyetik özellikleri, birçok uygulama alanında bu nanokompozitlerin kullanımına imkan sağlamaktadır. Bu nanokompozitler katalizör, ilaç taşıyıcı, absorban vb. olarak çeşitli uygulamalarda kullanılmaktadır.

Bu çalışmada alüminyum oksit nanopartikülleri ve demir bazlı manyetik alüminyum oksit nanokompozitleri çözelti yakma metodu ile sentezlenmiştir. Alüminyum oksit

nanopartiküllerinin ve demir bazlı manyetik alüminyum oksit nanokompozitlerinin sentezi sırasında farklı yakıt türleri ve miktarları kullanılmıştır. Alüminyum oksit nanopartikülleri, üre ve glisin olmak üzere iki farklı yakıt türü ve bunların farklı miktarları kullanılarak sentezlenmiştir. Demir bazlı manyetik alüminyum oksit nanokompozitleri ise üre, glisin ve sükröz olmak üzere üç farklı yakıt türü ve bunların farklı miktarları kullanılarak sentezlenmiştir. Sentezlenen numunelerin karakterizasyon çalışmaları için kullanılan cihazlar; X-Işını Difraktometresi (XRD), Taramalı Elektron Mikroskobu (SEM) - EDS Analizi, Termogravimetrik ve Diferansiyel Termal Analiz (TG/DTA), Brunauer-Emmett-Teller (BET) şeklindedir.

Karakterizasyon çalışmalarından elde edilen sonuçlara göre, alüminyum oksit nanopartikülleri ve demir bazlı manyetik alüminyum oksit nanokompozitleri çözelti yakma metodu ile nano boyutta başarılı bir şekilde sentezlenebilmiştir. Buna ek olarak, çözelti yakma metodu ile stokiyometrik oranda glisin yakıtı kullanılarak sentezlenen demir bazlı manyetik alüminyum oksit nanokompozitin, diğer sentezlenen numunelere kıyasla daha yüksek gözeneklilik ile küçük ve homojen dağılımlı partikül boyutuna sahip olduğu görülmüştür.

Sentezlenen numunelerin XRD ve SEM analizlerinin ve manyetik özelliklerinin incelenmesi sonucunda, çözelti yakma yöntemi ile yakıt olarak stokiyometrik miktarda glisin kullanılarak sentezlenen numunenin (SC-FA-G2) adsorpsiyon çalışmalarında kullanılmasına karar verilmiştir. Bu amaçla, çeşitli proses koşullarında SC-FA-G2 numunesi adsorban olarak kullanılarak sulu çözeltilerden Reaktif Mavi 19 (RB19) boya giderme yüzdeleri incelenmiştir. Deney setleri, Cevap Yüzey Metoduna (RSM) göre Design Expert 11.0 deney tasarım programı kullanılarak planlanmıştır. Box-Behnken Tasarımına göre, farklı koşullar altında 17 deney gerçekleştirilmiştir. pH, sıcaklık ve SC-FA-G2 adsorban miktarının adsorpsiyon prosesine olan etkileri incelenmiş ve Box-Behnken Tasarımı kullanılarak elde edilen verilere uyan bir model geliştirilmiştir. Ayrıca, adsorpsiyon deneylerinden elde edilen verilere göre, adsorpsiyon izoterm ve kinetik modelleri optimum koşullarda incelenmiştir.

Sonuç olarak, adsorpsiyon çalışmalarından elde edilen deneysel verilerin değerlendirilmesinden sonra, SC-FA-G2 kodlu numunenin RB19 boya giderme yüzdesi, pH 2, 400 mg adsorban miktarı/50 mL ve 25 °C'da % 100 olarak bulunmuştur. Ayrıca, bu numune için maksimum adsorpsiyon kapasite değeri (Q_{max}) ise 55.248 mg/g olarak hesaplanmıştır.

Anahtar Kelimeler: Alüminyum oksit nanopartikül, Demir bazlı manyetik alüminyum oksit nanokompozit, Çözelti yakma metodu, Cevap yüzey metodu, Boya giderimi

INTRODUCTION

1.1 Literature Review

Nanosize materials can have unique chemical, physical, biological, mechanical and optical properties and etc. in comparison with their macro scale. Such as for nanoceramics, having ultra-small size, large surface area and high reactivity provide them unique physico-chemical features than the bulk materials of same composition [1]. Aluminium oxide (alumina) nanoparticles were become extremely attractive materials due to their large surface area per volume, porosity, chemical reactivity, hardness and strength properties. Therefore, these nanoparticles play an important role in several applications such as electronics, optoelectronics, sensors, catalysis, coating materials and etc [2], [3].

Besides, the outstanding properties of the aluminium oxide nanoparticles, it is also possible to develop more qualified and improved nanocomposites by combining various materials [4]. For example, iron based nanocomposites can be easily separated from liquid phase by applying a magnetic field because of indicating magnetic feature of iron and its alloys [5]. It is obvious that, iron based aluminium oxide magnetic nanocomposites have numerous potential applications such as magnetic recording, ferrofluids, clinic drug delivery, waste water treatment, bio-separation, adsorption and etc. [6].

In textile industry, various quantities of dyes and/or dye by-products remain in waste water [7]. Adsorption is an alternative and environmental friendly method for treatment of industrial effluents [8].

1.2 Objective of the Thesis

Various techniques are available for the preparation of relevant nanomaterials or nanocomposites [9]. Solution combustion, one of these synthesis methods, can be defined as a novel and complex self-sustained chemical process. Metal, metal alloys and metal oxides nanoparticles in various sizes which are used in numerous critical applications can be obtained by this technique [10].

The main objectives of the present study are as follows:

- Synthesis of aluminium oxide nanoparticles using various fuel types and fuel amounts by solution combustion method,
- Synthesis of iron based magnetic aluminium oxide nanocomposites using various fuel types and fuel amounts by solution combustion method,
- Characterization of the synthesized samples such as chemical composition, morphology, thermal properties, surface area and porosity,
- Adsorption of RB19 dye onto synthesized nanocomposites from aqueous solutions under various process parameters such as pH, temperature and adsorbent amount,
- Usage of experimental design programme for investigation of the optimum process conditions,
- Examination of most appropriate adsorption isotherm models and kinetic models according to the data provided from the adsorption experiments of RB19 dye at the optimum conditions obtained.

1.3 Hypothesis

Nanosize materials can be obtained by various synthesis method including precipitation, sol-gel, hydrothermal, solution combustion method and etc. Solution combustion method, which defined as a quick and easy process to synthesize of nanosize materials, is influenced by several parameters such as fuel types, fuel amount, ignition temperature and etc. Utilization of various fuel types and fuel amounts during synthesis may lead to obtain nanocomposites in various chemistry, morphology, size and porosity. This variety can give an opportunity to specialise these particles optionally. Thus, the particles can be synthesized at desired specifications.

Therefore, in the present study, it was aimed i) synthesize of aluminium oxide nanoparticles and iron based magnetic aluminium oxide nanocomposites by solution combustion method using various fuel types and fuel amounts, ii) characterization of the

synthesized samples using X-Ray Diffraction (XRD), Scanning Electron Microscopy (SEM) and Energy Dispersive X-ray Spectroscopy (EDS), Thermogravimetric and Differential Thermal Analysis (TG/DTA) and the Brunauer-Emmett-Teller (BET), iii) choosing the best synthesized sample according to the data obtained from the characterisation studies, iv) using Design Expert 11.0 experimental design programme for designing and optimising of the experiments, v) performing the experiments for RB19 dye adsorption onto chosen sample from aqueous solution, vi) examination of the most suitable adsorption isotherm model and kinetic model according to the data obtained from adsorption experiments performed at optimum conditions.

According to the literature survey, there is no documentation was found about usage of glycine as fuel for the synthesis of iron based magnetic aluminium oxide nanocomposites by solution combustion method. Additionally, no study was found about RB19 dye removal from aqueous solutions by iron based magnetic aluminium oxide nanocomposites synthesis with glycine as fuel by solution combustion method.

NANOTECHNOLOGY

The term of Nanotechnology alludes to building things at the nanometre scale. Nanotechnology is related with controlling and making materials at the nuclear and subatomic level. Size relationships in chemistry, nanomaterials, condensed matter physics and many branches of science are intentionally interests in nanotechnology. For example, chemistry science is the interest of atoms, molecules and matters dimensions [1].

Nanotechnology is being relied upon to assume an important role in numerous scientific disciplines such as chemistry, material science, engineering, physics, biology, and computer technology. Recently, nanotechnology has encountered an exponential development since nanoparticles show superior physical and chemical properties. The nanostructured materials exhibit novel and significant physical, chemical and biological properties, which are not the same as those of materials in the micrometre scale [1], [11].

Lately, nanoparticles and nanocomposites have created huge interest due to their small size and high surface area to volume ratio. There are four main ways in which nanoscale materials can deviate from macroscopic material [1]. These are;

- i.** The gravitational forces become negligible and the electromagnetic forces dominate,
- ii.** Quantum mechanical model is used to describe motion and energy instead of classical mechanical model,
- iii.** Greater surface area / volume ratio and
- iv.** Random molecular motion

2.1 Nanoscale Properties

Nanoscale materials have original chemical, physicochemical, optical and mechanical properties such as ultra-small size, large surface area to mass ratio, high reactivity. These are gained to nanomaterials various and significant properties compared to bulk materials of the same compositions [1].

2.1.1 Optical Properties

The optical properties of a material depend on the interaction of light with the composition and atomic structure of materials. Nanoscale materials have unique optical properties due to their high surface area to volume ratio properties. When light is fall on the very thin film by the right wavelength, the electrons will move in coherent wave, which are named as surface plasmons. Since the high surface area of the nanoscale materials, the Surface Plasmon Resonance (SPR) effect takes place [1].

2.1.2 Chemical Reactivity

Chemical reactions occur at the surface of materials. The material with high surface area has a larger of reaction sites than the material with low surface area. Thus, nanoscale materials have greater chemical reactivity comparison with bulk state due to high surface area to volume ratio properties [12].

2.1.3 Mechanical Strength

Generally, metals are made up small crystalline grains. The boundaries of crystalline grains are slow down or stop of defects, when the metal is stressed. If the grain sizes of metals are made nanoscale, the materials interface area increases and thus materials strength are enhances [1].

2.1.4 Melting Point

Melting point is the temperature of atoms, ions or molecules in a substance have enough energy to overcome the intermolecular forces. Melting at nanoscale occurs over a wide range of temperature. Nanoscale materials surface atoms require less energy compared to bulk phase, because of contact with fewer atoms of the substance. Therefore, the particle size and shape of nanoscale materials play an important role in reducing the melting temperature [1].

2.1.5 Quantum Confinement

Quantum confinement comes from several dimensional confinements such as zero, one and two dimensional. Zero dimensional (0D) confinement is found only in the quantum dot. One dimensional (1D) confinement occurs in nanowires, similarly two dimensional (2D) confinement is only restricted in one dimension. These quantum confinements are responsible for increase in energy difference between energy states and band gap. However, quantum confinement effects can be sighted the diameter of the particle equal to electron wave function wavelength. When the materials scale decrease, their electronic and optical properties deviates and give a blue shift in optical illumination [1], [13].

2.2 Synthesis Methods of Metal Oxide Nanoparticles

Nanoparticles have great technological and scientific importance. Same compositions bulk materials cannot achieve fascinating properties of nanoparticles [14]. Most of the researches dedicated to development of synthesis methods of nanoparticles and nanostructure materials. These efforts gave access to production of wide range of compositions, monodisperse crystalline sizes materials [15].

Metal oxide nanoparticles application areas divided into two main sections: high surface area materials and materials taking advantage of the size-dependence of physical properties. For example, super capacitor materials based on large surface area per weight or film thickness. Metal oxide nanoparticles both high surface area and size-dependent properties are played an important role for using catalysis applications, due to catalytic activity change with size properties. Therefore, they can be also used in high surface area sensors and similar applications such as medical science, capacitor, batteries and etc. [16], [17].

There are various synthesis method for the production of nanosized metal oxide powders, such as precipitation, sol-gel, ball mill, spray pyrolysis, hydrothermal method, laser ablation [17]. The synthesis methods are frequently classified in to two broad categories top-down approach which includes physical methods and bottom-up which includes wet methods. Top-down and bottom-up approaches were presented schematically in Figure 2.1 [18].

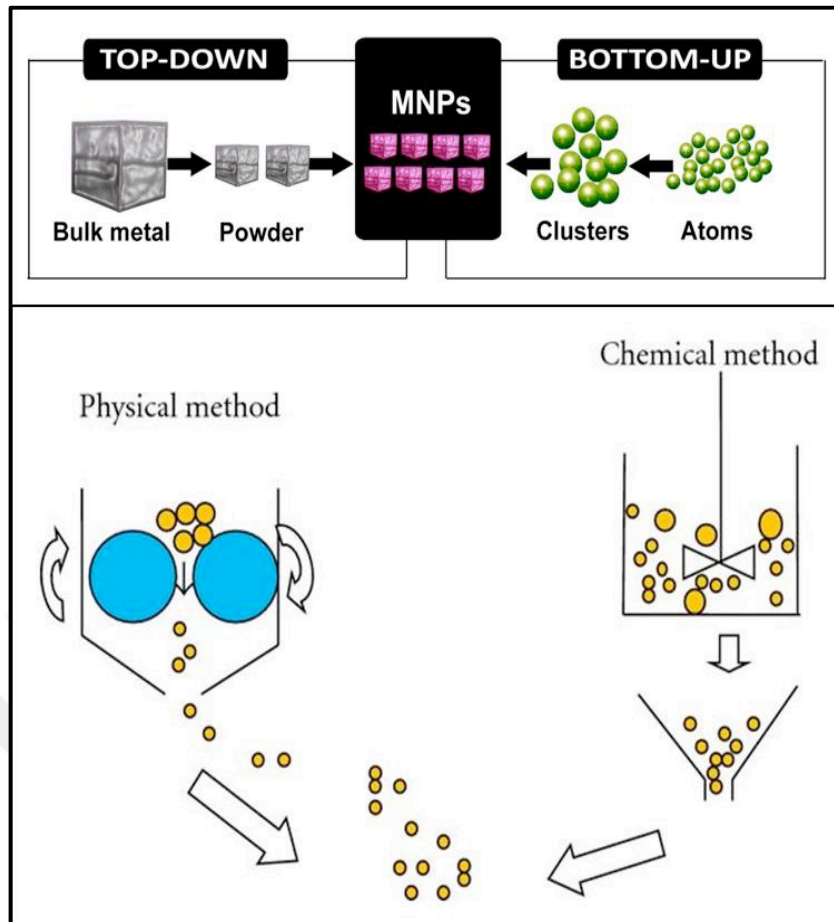


Figure 2.1 Schematic representation of top down and bottom up approaches [18]

2.2.1 Top-down Approaches

Nanoparticles and nanocomposites can be produced in large quantities by top-down approach (physical methods). However, synthesis of equidimensional nanocomposites is not easily achieved [18]. The production methods based on this approaches are defined as lithography and ball milling [19].

Lithography is using applications of printed circuits and computer boards for several decades. This method named as nanolithography and defined as the accumulation or removal of structures from the molecular scale [19].

Ball milling is applied in producing metallic and ceramic nanomaterials [20]. This method based on broken the dusts which between the balls and reduced to nanometres scale. However, the main disadvantages of this method are obtained wide size distributions nanoparticles and remained surface residues due to contamination [19].

2.2.2 Bottom-up Approaches

Methods based on bottom-up approach give uniformity in size of nanoparticles and nanocomposites as controlled particle size can be achieved easily. Moreover, nanocomposites could be synthesized at various shapes (nanorods, nanowires, nanotubes and etc.) by those methods [18]. This approach provides better controlling sizes, shapes and size ranges [20].

Bottom-up approaches include precipitation, sol-gel, spray pyrolysis, hydrothermal and solution combustion and etc. for synthesis of nanostructured metal oxide. These methods are based on the ground of kinetic control of nucleation and growth of the particles in aqueous suspension or on the introduction of spatial constraints. Control of nucleation and the growth of nanoparticles are the key factor of these methods [1].

Metal oxides synthesis in solution phase can be divided four steps including precursor formation, nucleation, growth and aging. The steps of synthesis from the solution were presented in Figure 2.2 [16]. Before nucleation occurs, zero-charge precursor molecules need to comprise for condensation. Nucleation can occur until the precursor concentration is below the nucleation threshold and build-up of precursor molecules results in a supersaturation. Supersaturated solution growth is continued until the saturation concentration of the solid reached. After nucleation and growth steps, the average particle size, morphology and distribution may change by aging [16].

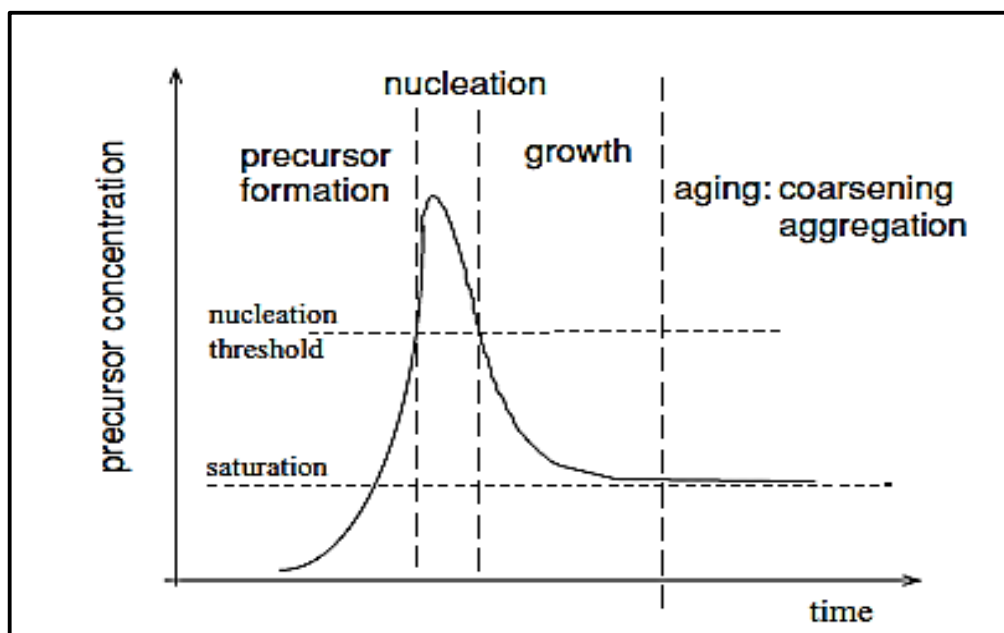


Figure 2.2 Precursor concentration versus time of nanoparticles prepared by solution phase methods [16]

2.2.2.1 Precipitation

Precipitation is defined as a simplistic and convenient method for synthesizing nanocrystalline metal oxides. The precipitation synthesis method includes two steps. In the first step, the precipitation of metal hydroxides from the solution is obtained by rapid injection of precipitant. In the second step, the aging of precipitated metal hydroxides at specified temperature and separation of the metal hydroxides by centrifugation. The prepared product is calcined to obtain nanosize metal oxide particles. Parida et al. [21] investigated in their study that the effect of various precipitation agents on the size and surface area of synthesized aluminium oxide nanoparticles by precipitation method. To synthesize aluminium oxide nanoparticles, ammonium bicarbonate, ammonium carbonate, sodium bicarbonate and sodium carbonate have been used. The chemical reactions [22] between ammonium bicarbonate as a precipitation agent and aluminium nitrate as a precursor used to synthesize aluminium oxide nanoparticles are expressed as follows:



Synthesis of aluminium oxide is generated under room or elevated temperatures with the precipitation method. Also, the chemical composition, size and shape of synthesized nanoparticles are influenced by the type of precursor used and its concentration, reaction temperature, pH value and ionic strength of media [1].

In precipitation method, reactions are hard to control. Even though, controlled precipitation cannot be achieved, precipitated grains may be reagglomerated. This feature of precipitation method indicates that it is not a repeatable method for synthesizing nanoparticles [1], [22].

2.2.2.2 Sol-gel

The sol-gel method is widely studied for synthesis of aluminium oxide as a nanomaterial due to produce particles of high purity and high specific surface area [22]. Moreover, the sol-gel process is a versatile approach for fabrication of materials with various properties such as tough and light materials. In the sol-gel method, the precursor

is exposed to hydrolysis and polymerization reactions series to form colloidal suspension. Thus, particles are condensed in a gel phase. In the sol-gel method, synthesized particles' shape and size are affected from the process parameters; temperature, pH value and etc. In this method, chemical precursors are used to obtain fine powders with high chemical reactivity, high purity, homogeneity [1].

Sol-gel method is also useful for coating materials in the form of films, which can be mono or multilayers. The coating can be applied range of 50-500 nm thicknesses on surfaces. For example, to obtain thicker layers suitable for membranes, during the coating process wetting and drying steps are repeated recurrently. The sol-gel process can also be used to produce fibres.

The important advantage of sol-gel method is the control availability on the chemical composition. Though, this method is a simple and low-cost technique for synthesis of nanometal oxides. There are difficulties during the synthesis such as controlling and drying steps [1], [23]. Moreover, organic contaminations can remain in the gel and the cleaning steps are required [20]. The various reactions and processing steps of the sol-gel were represented in Figure 2.3 [20].

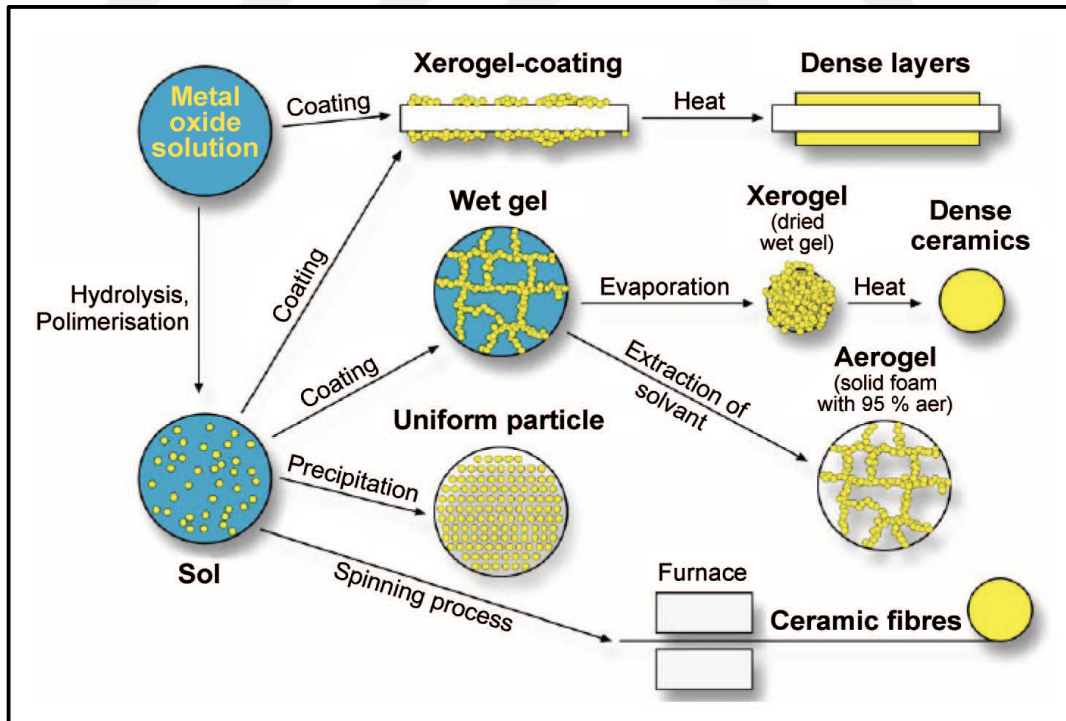


Figure 2.3 The reactions and processing steps of sol-gel method [20]

2.2.2.3 Hydrothermal Synthesis Method

Hydrothermal synthesis is an environmental friendly method and it provides crystalline anhydrous material from aqueous solutions at elevated temperatures and pressures. In this technology, it is not required high-temperature calcination. The reaction occurs at plug steel autoclaves for hydrothermal synthesis method [24].

Suchanek (2010) [24] synthesized alpha phase Al_2O_3 powder with hydrothermal synthesis method. Figure 2.4 shows that schematic diagram of the autoclave in hydrothermal synthesis method to produce $\alpha\text{-Al}_2\text{O}_3$ powders.

Zhou et al. (2013) [25] reported that aluminium oxide hollow microspheres using urea as a precipitating agent and trisodium citrate as a mediating agent by hydrothermal synthesis method. They synthesized successfully well crystalline aluminium oxide hollow microspheres with high specific surface area by hydrothermal synthesis method.

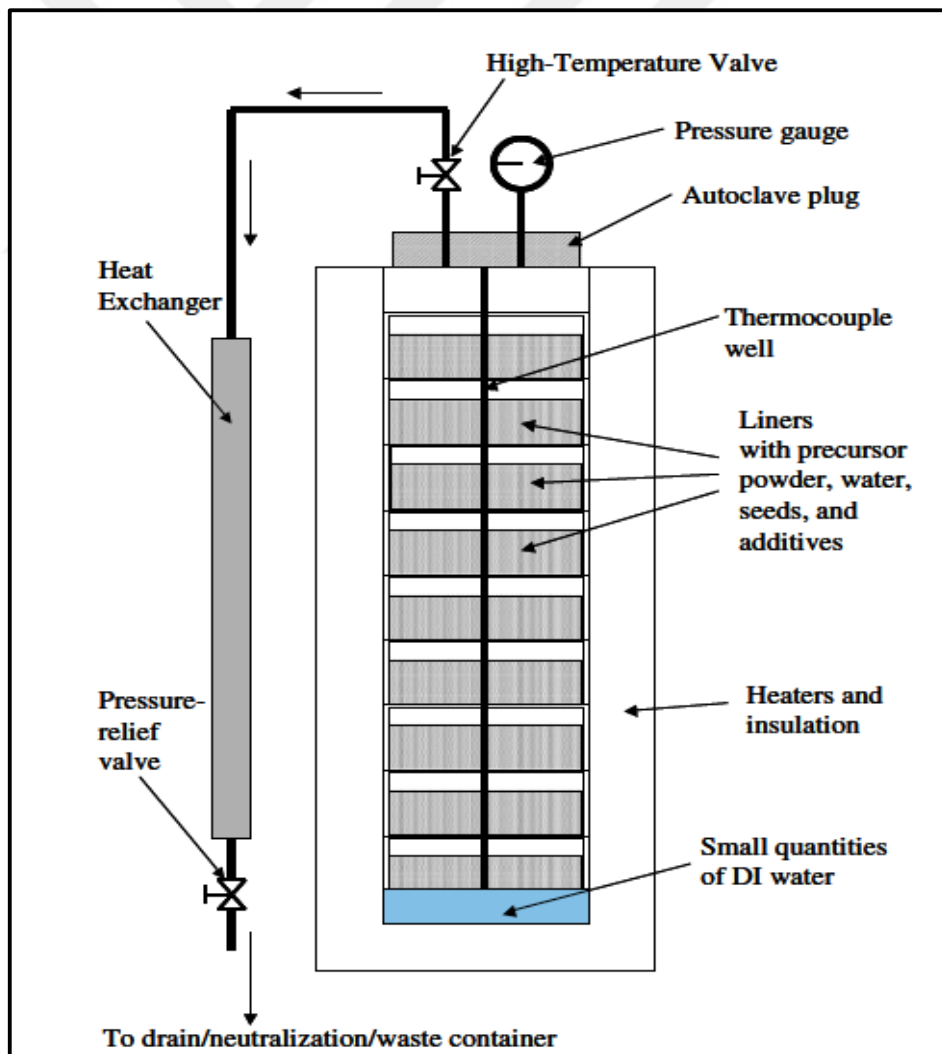


Figure 2.4 Schematic diagram of the autoclave in hydrothermal synthesis method [24]

2.2.2.4 Spray Pyrolysis

Spray pyrolysis is a powerful technique to obtain chemically homogeneous ceramic nanopowders in high purity. Large quantities of oxide powders which are homogeneously distributed small particles, have been synthesized by this method. The key point of this method is choosing the convenient starting solution. In this method, the reaction generally occurred in solution droplet and then the solvent is evaporated [1].

Spray pyrolysis method frequently used to produce nanosize metal oxide powder. The schematic representation of spray pyrolysis method for carbon nanotubes synthesis process was given in Figure 2.5 [26].

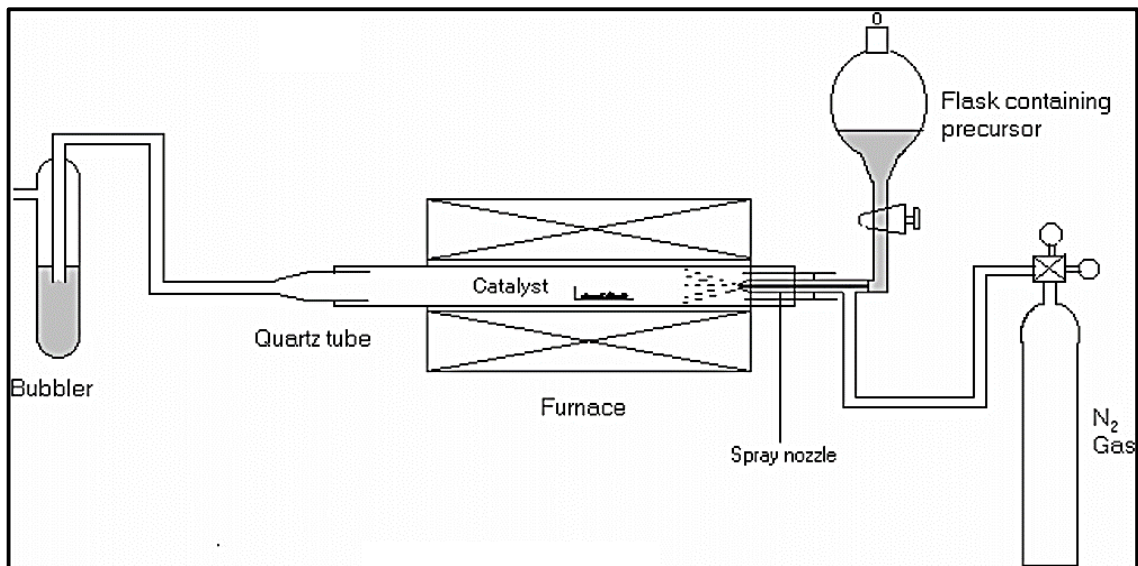


Figure 2.5 Schematic representation of spray pyrolysis method [26]

2.2.2.5 Solution Combustion Method

Solution combustion synthesis (SCS) method was first used in 1980 for production of nanoscale materials. The solution combustion synthesis is a self-sustained thermal process, and the heat which is main source of this method comes from combustion reactions. The solution combustion synthesis includes several exothermic reactions, and the procedure starts with the dehydration reactions and decomposition of the homogeneous reactions thermally. Solution combustion method allows to produce various nanoscale materials for usage of them in several application areas [10]. Solution combustion synthesis is defined as a quick and easy process. Moreover, it was also reported that SCS is an energy saving and eco-friendly synthesis method for preparing high purity grade and homogeneous nanosize materials [22], [27].

Solution combustion synthesis is general form of self-propagating high temperature synthesis (SHS) or simply combustion synthesis (CS). However, SCS process has three main differences from SHS and CS process.

- Firstly, the initial components are mixed in aqueous solution and the ions in the solution are 0.1-1 nm size range at SCS. However, solid powders are used for SHS process and initial powder sizes are from $\sim 10^2$ to 10^5 nm.
- Secondly, for SCS process, the heat is generated from combustion of organic fuels. While in classical SHS process, the heat is generated from the synthesis reaction.
- Thirdly, SCS process creates huge amount of gaseous products. Gasification leads to solid product's expansion and quick decrease at temperature. These features provide a chance to obtain porous and finely dispersed solid product [10].

Moreover, solution combustion synthesis depends on the chemical composition of fuel, oxidizer and solvent. The most frequently used oxidizer, fuel and solvent types are presented in Table 2.1 [10].

Table 2.1 The components used in solution combustion method [10]

Oxidizer	Fuel	Solvent
<ul style="list-style-type: none"> • Metal nitrate or nitrate hydrates • $(Me(NO_3)_x \cdot nH_2O)$ • Ammonium nitrate (NH_4NO_3) • Nitric acid (HNO_3) 	<ul style="list-style-type: none"> • Urea (CH_4N_2O) • Glycine ($C_2H_5NO_2$) • Sucrose ($C_{12}H_{22}O_{11}$) • Glucose ($C_6H_{12}O_6$) • Citric acid ($C_6H_8O_7$) • Hydrazine-based fuels 	<ul style="list-style-type: none"> • Water (H_2O) • Hydrocarbons • Alcohols

Solution combustion synthesis can be performed in two modes as volume and self-propagating combustion, like other combustion synthesis techniques. The first mode is called as volume combustion or thermal explosion. In Figure 2.6, the examples of volume combustion synthesis were given for $Ca_3Al_2O_6$ and Fe_2O_3 [10].

In volume combustion mode; firstly, the reactive mixture is preheated to the boiling point of the solvent (Stage I) and the mixtures of free water are evaporated (Stage II, Figure 2.6b). The next preheating stage is characterized by a high heating rate (Stage III). Followed by, the temperature is increased to ignition temperature (T_{ig}) to reach the maximum value of T_m (IV phase) [10].

During the combustion synthesis reaction, the ignition temperature (T_{ig}) represents the dynamically activated temperature without an additional supply of external heat and maximum flame temperature (T_m) defined as maximum temperature reached in the actual configurations [27]. Final step is the cooling phase of synthesized samples (Stage V) [10].

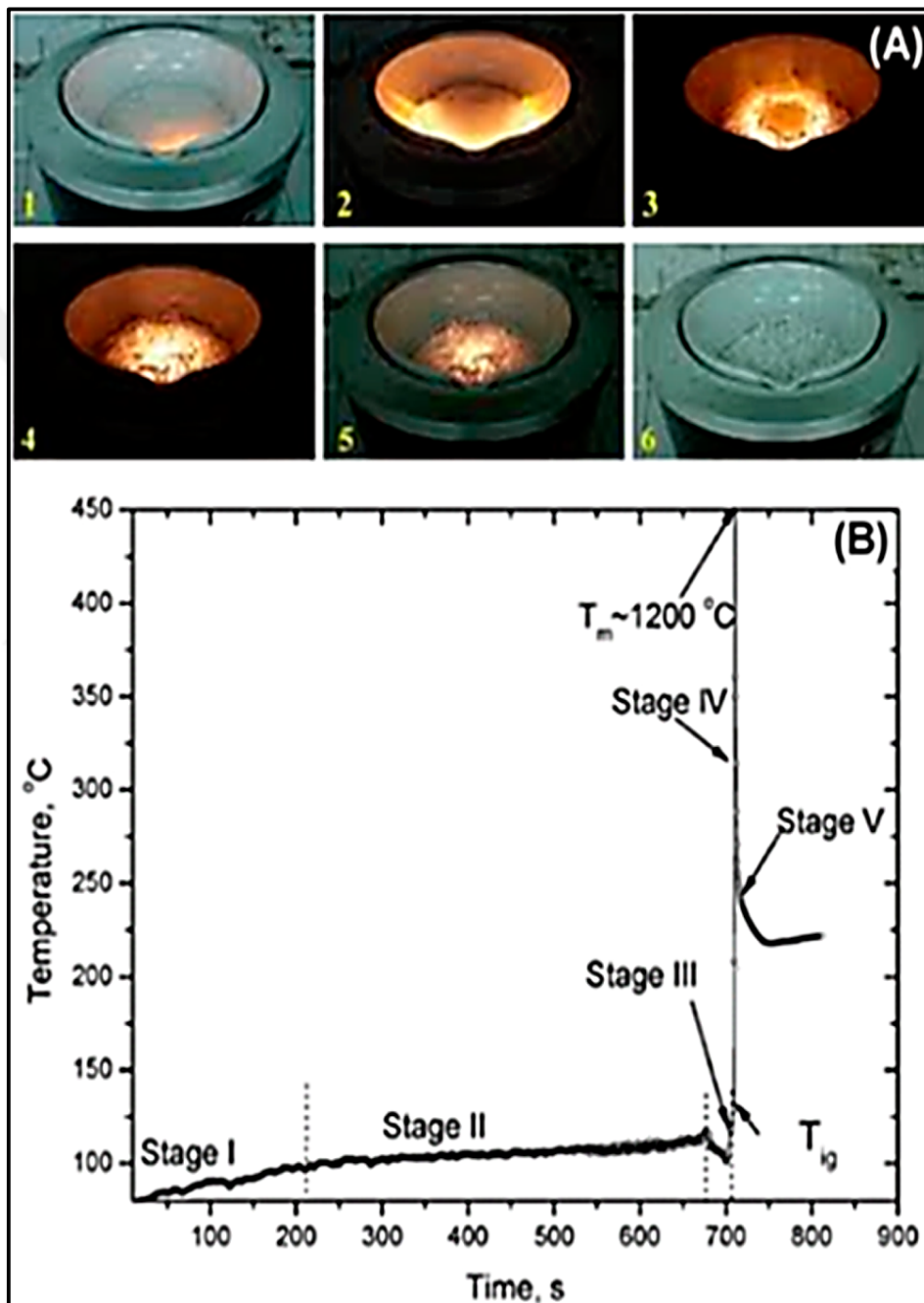


Figure 2.6 Volume combustion mode of synthesis of a) $\text{Ca}_3\text{Al}_2\text{O}_6$ and b) Fe_2O_3 [10]

The second SCS mode is called as a self-propagating combustion mode. In this mode, a small volume reactive solutions or gels is heated locally and the exothermic reactions begin automatically along the rest of the reactive solutions volume. As an example of this mode, the combustion waves and time-temperature profile of nickel nitrite-glycine system were presented in Figure 2.7. The preheating stage of self-propagating combustion mode is relatively shorter than volume combustion mode [10].

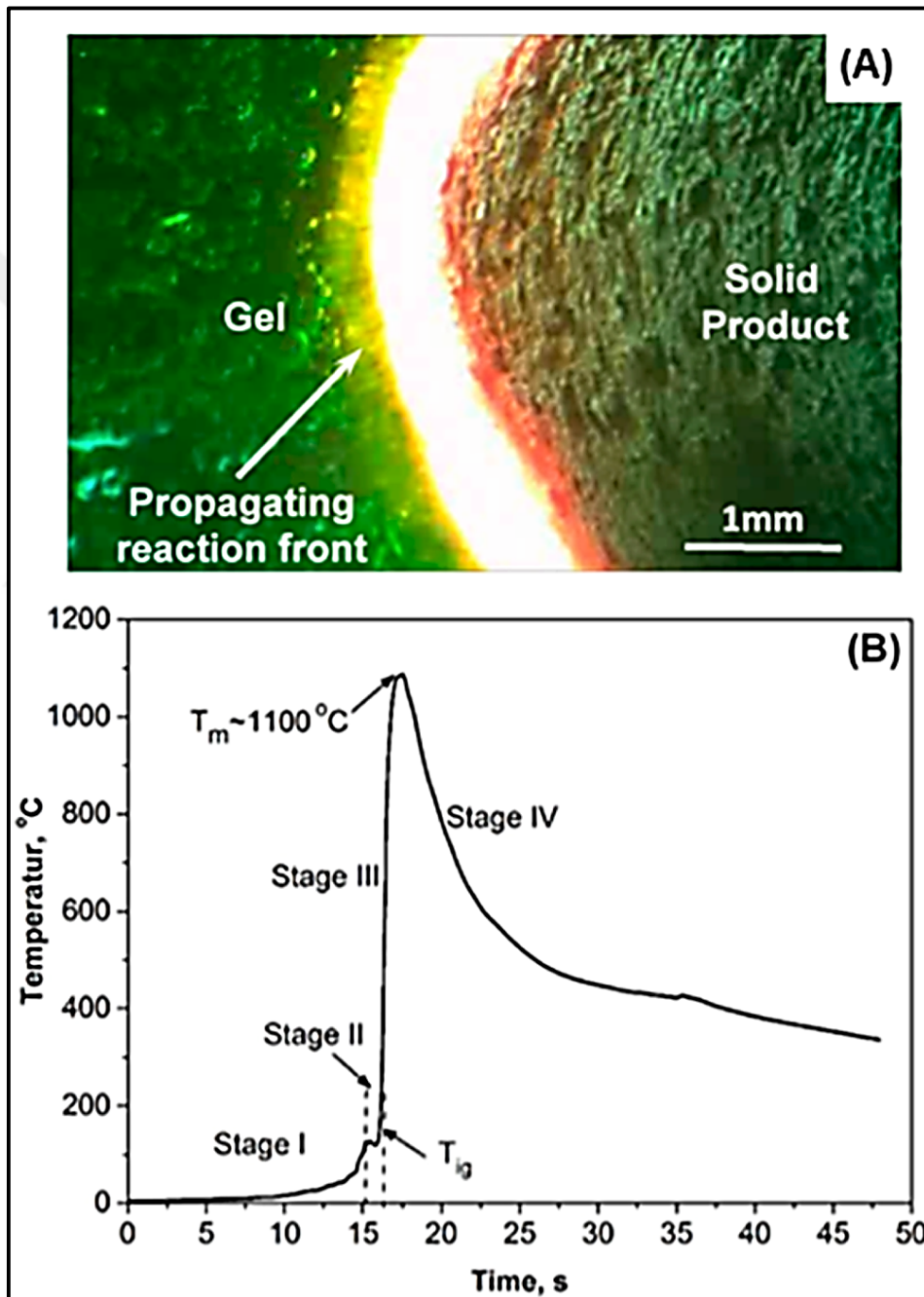


Figure 2.7 Self-propagating combustion mode of nickel nitrite-glycine a) reaction systems and b) time-temperature profile [10]

In general, there are various methods for heating the initial reactions in solution combustion synthesis method. The most easily applicable method is placing the precursor solution in glass or ceramic container on a hot plate or inside a preheated furnace at temperature about 300-500 °C. The heating of the precursor solution, evaporation of the solvent, formation of the gel, combustion and generation of the solid product occur in one step simply. For this reason, this heating method is used commonly for solution combustion synthesis.

Besides, the microwave-assisted heating can be used for preheating the precursor solutions. However, microwave assisted heating differs from conventionally heating mechanism. In this method, heat is generated by the interaction of electromagnetic field. This process continues with volume combustion mode, generally [10].

The reaction mechanism of the combustion reactions is very complex. There are several parameters affecting the reactions such as flame types, fuel types, fuel to oxidizer ratio, ignition temperature and amount of water in precursor mixture.

The exothermic chemical reaction can be performed, when the oxidizer and fuel are mixed in an appropriate proportion in solution combustion process. The fuel to oxidizer ratio is one of the most important parameters in solution combustion method. Because of this ratio influences the pore size and morphology of particles [27]. Solution combustion method are used in various applications such as catalyst, electro catalyst, biotechnology and power applications like fuel cells, supercapacitors, batteries and etc. [28], [29].

ALUMINIUM OXIDE

Aluminium oxide (alumina) is a compound of aluminium and oxygen with chemical formula of Al_2O_3 [30]. It is one of the most important ceramic materials that using a large variety of applications from metallurgy to electronics and optics to nanotechnology [31].

Aluminium oxide has several advantages when compared with other ceramic materials due to their superior mechanical, thermal, chemical and physical properties [32]. Recently, Al_2O_3 has become essential material to several application areas because of its hardness, chemical inertness, high melting point, non-volatility, high refractoriness and resistance to oxidation and corrosion properties [24], [30], [31].

Industrially, more than 45 million tons of Al_2O_3 are produced in the world and consumed for numerous purposes at several applications. Hardness feature of Al_2O_3 provides to utilize it as abrasive materials and similarly, its high melting point gives a chance to use it as refractory materials [32].

3.1 Crystalline Structure and Types of Aluminium Oxide

In nature, Aluminium is found in crystalline oxides, and it is natural, colourless and transparent crystalline. Al_2O_3 called alumina, is an inorganic solid chemical compound and is formed from geological processes of different kind of rocks. Aluminium oxide has several crystalline structures [31]. For example polycrystalline alpha-alumina ($\alpha\text{-Al}_2\text{O}_3$) with a hexagonal structure and it was used for many applications because of its high strength. When the $\alpha\text{-Al}_2\text{O}_3$ phase is single crystal it is called corundum/sapphire. $\gamma\text{-Al}_2\text{O}_3$ phase is an unstable phase and has two different lattices.

The first lattice is comprised of aluminium ions with octahedral and tetrahedral interstitial locations, and the second one (oxygen lattice) is formed with face centre cubic structure. The crystal structures of α - Al_2O_3 and γ - Al_2O_3 were presented in Figure 3.1 (a) and (b), respectively [33].

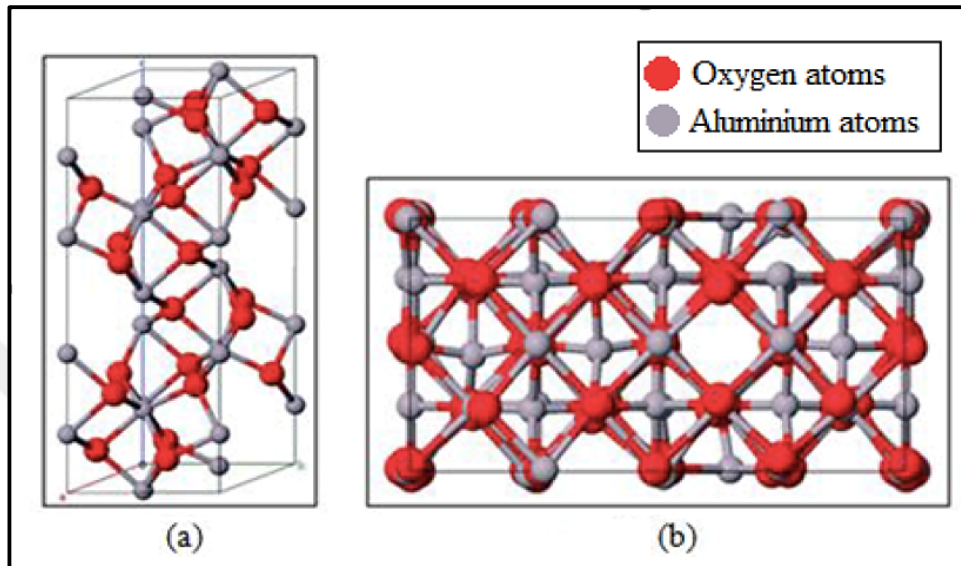


Figure 3.1 The crystal structure of (a) α - Al_2O_3 and (b) γ - Al_2O_3 with colour code [34]

There are five types of aluminium hydroxides which are named as gibbsite, bayerite, nordstrandite, diaspore and boehmite. The aluminium hydroxides names, chemical composition and formulation were presented in Table 3.1 [31]. There are seven synthetic transition aluminium oxides that are indicated by Greek letters: gamma (γ), delta (δ), theta (θ), kappa (κ), chi (χ), eta (η) and rho (ρ) [31]. These forms of aluminium oxide occur during the thermal decomposition of aluminium hydroxides under various conditions.

The thermal transformation of different aluminium hydroxides was presented in Figure 3.2. The phase transformation of aluminium oxide is not reversible. Therefore, thermodynamically more stable aluminium oxide is formed at higher temperatures. Thus, at high temperatures, heat treatment paths will terminate in α - Al_2O_3 [31], [32]. α - Al_2O_3 is last crystalline form of aluminium oxide. γ - Al_2O_3 (gamma aluminium oxide) and α - Al_2O_3 (alpha aluminium oxide) contain the same ratio of Al to O atoms. Only difference between them is their crystal structure.

While gamma aluminium oxide has tetragonal structure, alpha aluminium oxide has hexagonal crystal structure. Conventional $\gamma\text{-Al}_2\text{O}_3$ is formed from the thermal dehydration of boehmite at the temperature of 450 °C. The γ phase is a metastable phase and can be converted to stable form of α phase by heating thermodynamically [30]. Because of the superior features of $\gamma\text{-Al}_2\text{O}_3$ such as large surface area and high catalytic activity, the transformation of boehmite to $\gamma\text{-Al}_2\text{O}_3$ is the most important transition in aluminium oxide. When $\gamma\text{-Al}_2\text{O}_3$ transformed to $\alpha\text{-Al}_2\text{O}_3$, its porous structure and high specific surface area disappear [34].

Table 3.1 Types of aluminium hydroxides [31]

Mineral Name	Chemical Composition	Accepted Standard Crystallographic Designation (1957) [31]
Gibbsite	Aluminium trihydroxide	$\gamma\text{-Al(OH)}_3$
Bayerite	Aluminium trihydroxide	$\alpha\text{-Al(OH)}_3$
Nordstrandite	Aluminium trihydroxide	Al(OH)_3
Diaspore	Aluminium oxide hydroxide	$\gamma\text{-AlOOH}$
Boehmite	Aluminium oxide hydroxide	$\alpha\text{-AlOOH}$

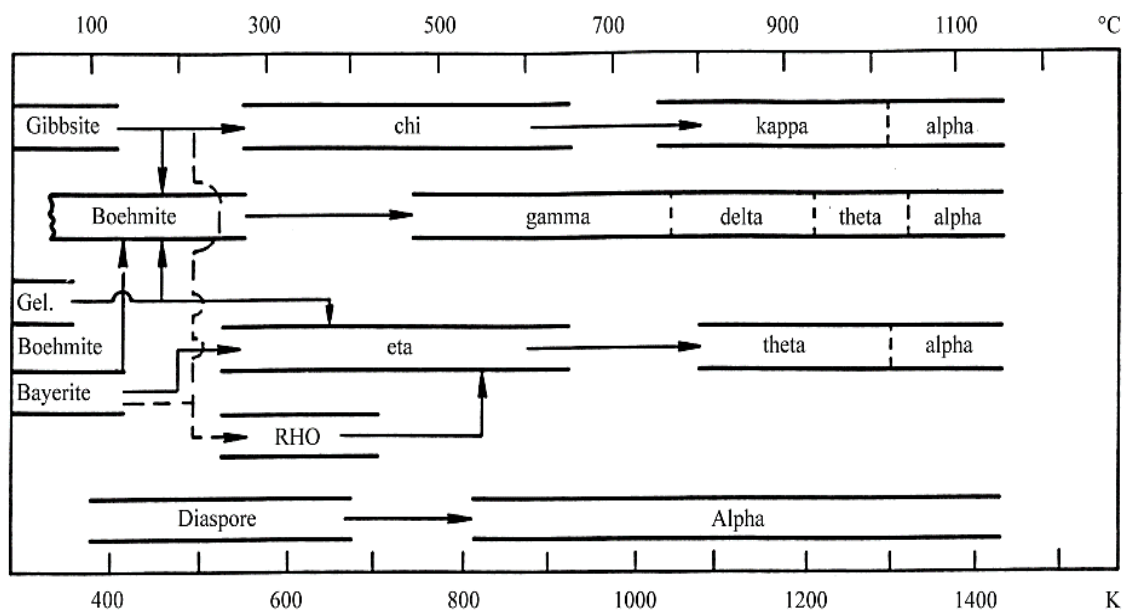


Figure 3.2 Thermal transformation of various aluminium hydroxides [31]

After the thermal dehydration of various aluminium hydroxides, several types of aluminium oxide are formed. Though they have same chemical compositions, their X-ray patterns are different. Figure 3.3 shows that X-ray data of the transition aluminium oxide types including chi- Al_2O_3 , kappa- Al_2O_3 , gamma- Al_2O_3 , delta- Al_2O_3 , theta- Al_2O_3 , eta- Al_2O_3 and alpha- Al_2O_3 . In Figure 3.3, the crystalline structures of aluminium oxide were indicated by well-defined peaks [31].

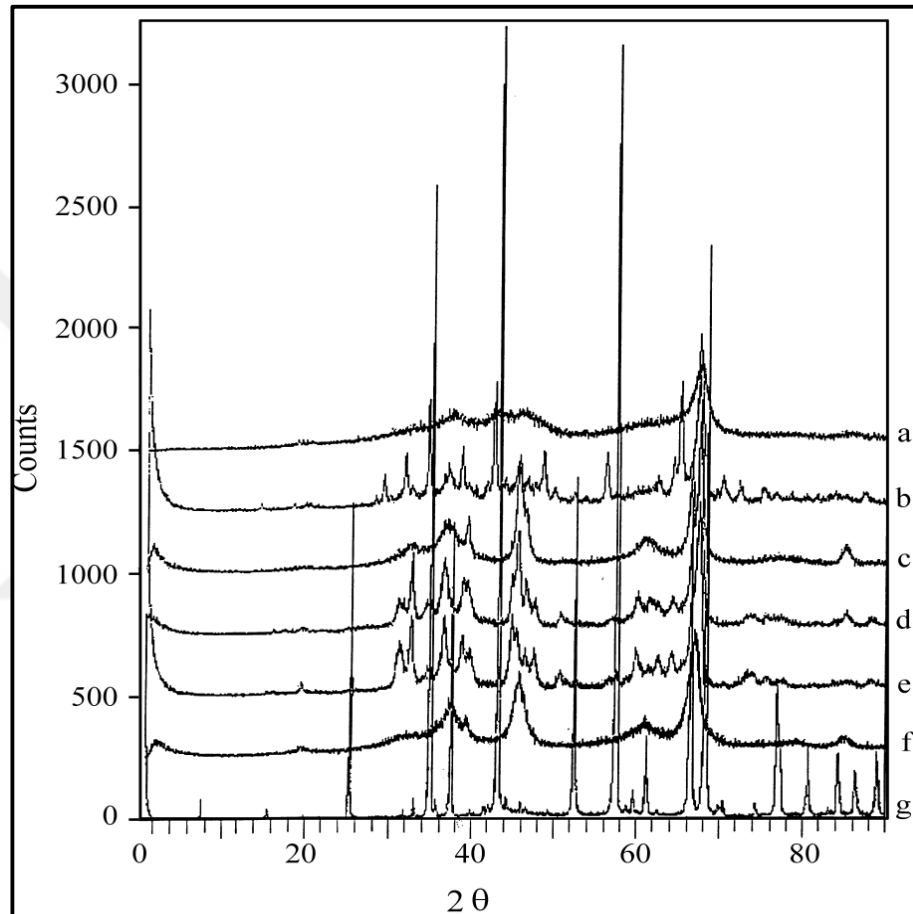


Figure 3.3 X-ray diffraction peaks of a) chi- Al_2O_3 , b) kappa- Al_2O_3 , c) gamma- Al_2O_3 , d) delta- Al_2O_3 , e) theta- Al_2O_3 , f) eta- Al_2O_3 and g) alpha- Al_2O_3 [31]

3.2 Aluminium Oxide, Properties and Applications

Aluminium oxide has a lot of interesting properties, such as high hardness, high stability, high insulation and transparency and these properties ensure different advantages for several application areas [17]. Aluminium oxide has wide area of use such as fire retard, catalyst, insulator, surface protective coating and composite materials areas [17].

The importance of aluminium oxide comes from its utilization in many chemical reactions as catalyst and catalytic support due to its favourable textural properties, large surface area, large pore volume, homogenous size distribution within mesoporous range and intrinsic acid-base characteristics. Acidic and basic sites of aluminium oxide surface were represented schematically in Figure 3.4 [35].

Porosity is necessary and significant for high surface area within the pellet. However, pore shape and size distribution of aluminium oxide are secondary critical factor for diffusion resistance. Controlling the morphological properties of aluminium materials during synthesis has great importance for performance and purpose of materials [35].

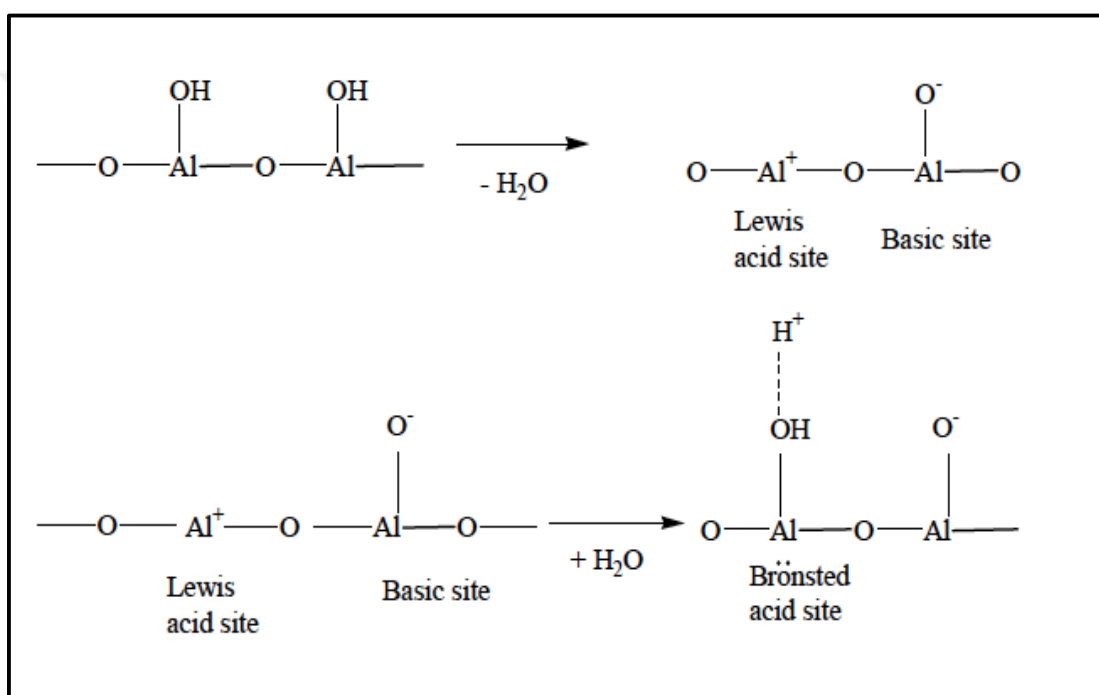


Figure 3.4 Acidic and basic site in aluminium oxide surface [35]

Generally, $\alpha-Al_2O_3$ plays an important role in production of numerous advanced ceramic materials and ceramic-based applications, due to their unique thermostable properties [36]. $\gamma-Al_2O_3$ also widely used as catalyst, catalyst support and adsorbent due to its high surface area in automotive and petroleum industries [35]. The transparency property of aluminium oxide film enabled to using optics application as well. Moreover, Al_2O_3 is an electrical insulator having high thermal conductivity [30].

3.3 Aluminium Oxide Nanoparticles, Properties and Applications

During the last few decades, nanosized aluminium oxide powders are become extremely compelling materials for advanced engineering and several applications such as catalyst of reactions, additive of paints, pigments or ceramics, refractory materials, abrasive grains, metals-alloys manufacturing and etc. [1], [22]. Aluminium oxide nanoparticles have thermal, chemical, electrical, optical and catalytic properties besides its physico-chemical properties like hardness, high thermal resistance, high strength to bases and acids, mechanical strength, eminent insulation and transparency properties [1], [17].

Aluminium oxide nanoparticles have larger surface area than micron sized aluminium oxide particles and these properties ensure unique features like porosity and chemical activity. Aluminium oxide nanoparticles/nanocomposites have been used for drug delivery applications based on its smaller particle size, homogeneous size distribution and spherical morphology. Porous aluminium oxide is interested to be used in versatile applications, including electronic and optical devices, magnetic storage disks, sensors and membranes, like aluminium oxide nanoparticles [1].

Nowadays, aluminium oxide nanoparticles play an important role in various applications such as high tech polymeric devices with its thermal mechanical properties such as high thermal conductivity and stiffness. Moreover, aluminium oxide nanoparticles are used as dispersion strengthening, transparent conductive-optical coating, wear resistant additives, biomaterials, nanocomposites, catalyst support, heat-transfer fluids (suspensions), drug delivery and etc. [37], [38].

MAGNETIC NANOPARTICLES

In the literature, more than 50 articles on magnetic nanoparticle were published for the last decade. In this context, synthesis of magnetic nanoparticles attracted considerable attention [39]. Magnetic nanoparticles have high magnetization and paramagnetic behaviours, and therefore they can be utilized in wide range of application areas [40]. Magnetic nanoparticles related to nanotechnology-based materials which are used in fields of analytical chemistry, biosensing and nanomedicine.

Magnetic nanoparticles also include the group of metallic nanoparticles and nanoalloys. For manufacturing magnetic nanoparticles, iron (Fe), cobalt (Co), nickel (Ni) and some other elements usually combine with several metals to obtain magnetic constituent [39]. Iron and iron oxide nanoparticles such as magnetite (Fe_3O_4) and maghemite ($\gamma\text{-Fe}_2\text{O}_3$) are commonly used nanoparticles for various applications. Highly magnetic materials such as cobalt and nickel have been less interested due to their oxidation sensitivity and toxicity [41].

Magnetic effects of nanoparticles are caused the movement of electrons, protons, holes, positive or negative ions which have mass and also electric charges. The magnetic domain (Weiss domain) refers to a volume of ferromagnetic material in which all magnetons are aligned in the same direction by the exchange forces. According to the magnetic domain theory, critical size of single domain is affected several factors including the value of the magnetic saturation, the strength of exchange forces, domain wall energy and shape of the particles. The reaction of ferromagnetic materials characterized by two main parameters; including remanence and coercivity. For example; when the particle size is reduced, the coercivity reaches the maximum value, and then decreases towards zero (Figure 4.1) [41].

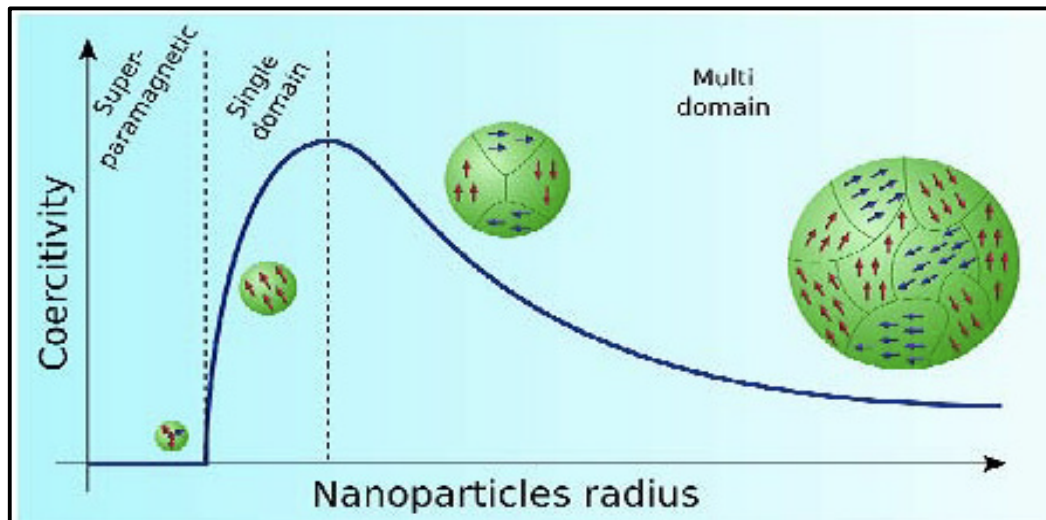


Figure 4.1 Schematic illustration of the coercivity and particle size relations [41]

Single domain particles sizes decrease below a critical diameter, the coercivity becomes zero and particles become superparamagnetic. Thermal effects are caused to become superparamagnetic. Superparamagnetic nanoparticles become in the presence of an external magnet, however returned to a nonmagnetic state when the external magnet is removed [41]. Several methods can be used to synthesize magnetic nanoparticles such as; co-precipitation, micro emulsion, thermal decomposition, solvothermal, chemical vapour deposition, laser pyrolysis and combustion synthesis [39], [41].

4.1 Iron Based Magnetic Nanoparticles, Properties and Applications

There are many types of iron oxide in nature, but the most popular magnetic nanoparticles are zero-valent iron, Fe_3O_4 and $\gamma\text{-Fe}_2\text{O}_3$. They have various physicochemical properties among iron oxide types [42].

- $\gamma\text{-Fe}_2\text{O}_3$ is one of the most frequently used ferromagnetic materials and it is an oxidation product of Fe_3O_4 [4].
- Magnetite, ferromagnetic black colour iron oxide, contains both Fe(II) and Fe(III) [42]. They are the most magnetic of all the naturally occurring minerals on earth. Magnetite is commonly used for biological applications [41].
- Hematite ($\alpha\text{-Fe}_2\text{O}_3$) is another types of iron oxide and the most thermodynamically stable phase. $\alpha\text{-Fe}_2\text{O}_3$ is used in several applications such as catalysts, pigments, gas sensors, optical devices and water purification due to its high surface area and most stable properties [34].

Different magnetic states of individual atoms of iron, which include paramagnetism, ferromagnetism, antiferromagnetism and ferrimagnetism, were presented in Figure 4.2. The paramagnetic state structure has zero net magnetization because of its crystal produces randomly aligned magnetic moments. When the paramagnetic state is exposed to an external magnetic field, the moments align to produce a small net crystal magnetization. At the ferromagnetic and antiferromagnetic states, the individual moments are randomly aligned without an external magnetic field [42].

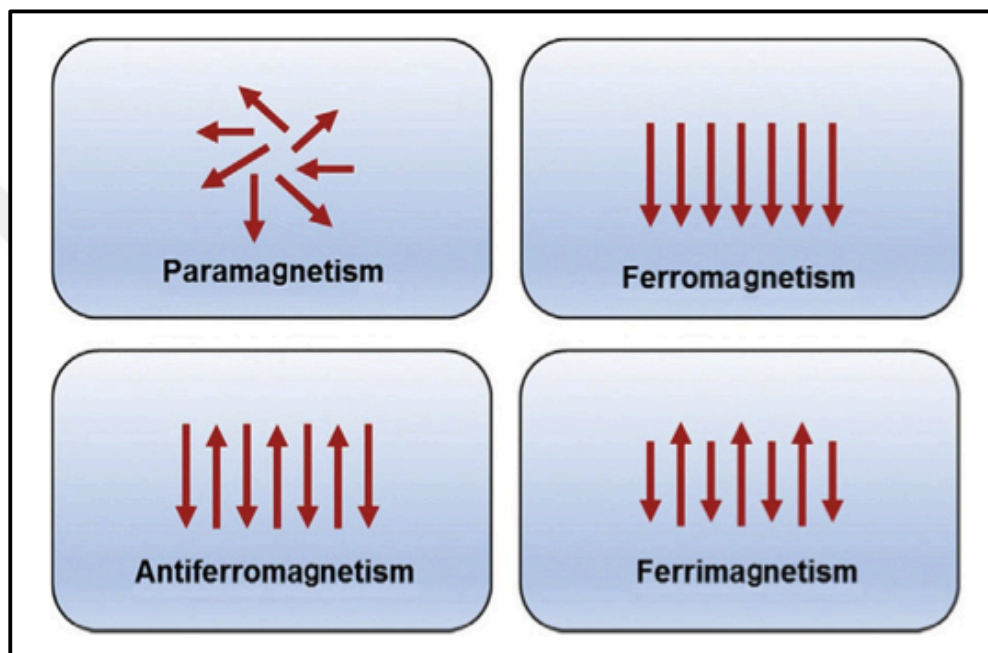


Figure 4.2 Alignment of the magnetic states [42]

Iron based magnetic nanoparticles with cubic, cuboctahedral or rod-like shape have been synthesized and these nanoparticles exhibit interesting properties such as geometric shape anisotropy, large magnetic moments, high magnetic anisotropy and etc. due to their shape. Moreover, iron based magnetic nanoparticles are used in many applications due to their specific shapes [43].

Iron based magnetic nanoparticles inexpensive to produce and demonstrates sufficient physical and chemical stability as well as being biocompatible and environmentally safe. The important aspect of iron based magnetic nanoparticles is their usage in specific bio applications such as magnetic separation, drug delivery, magnetic fluid hyperthermia and thermoablation, magnetic resonance imaging (MRI) and biosensing [39].

Moreover, iron based magnetic nanoparticles are frequently used as synthetic pigments in ceramic and paints. The magnetic encapsulates may find various areas of life and branches of industry. For example, iron based magnetic nanoparticles, especially hematite and magnetite, are used for preparation of NH_3 , desulfurization of natural gas and high temperature water-gas shift reactions [41]. The necessary precursor types, synthesis methods and surface modification for magnetic particles and functionalization for synthesized particles were summarized in Figure 4.3 [39].

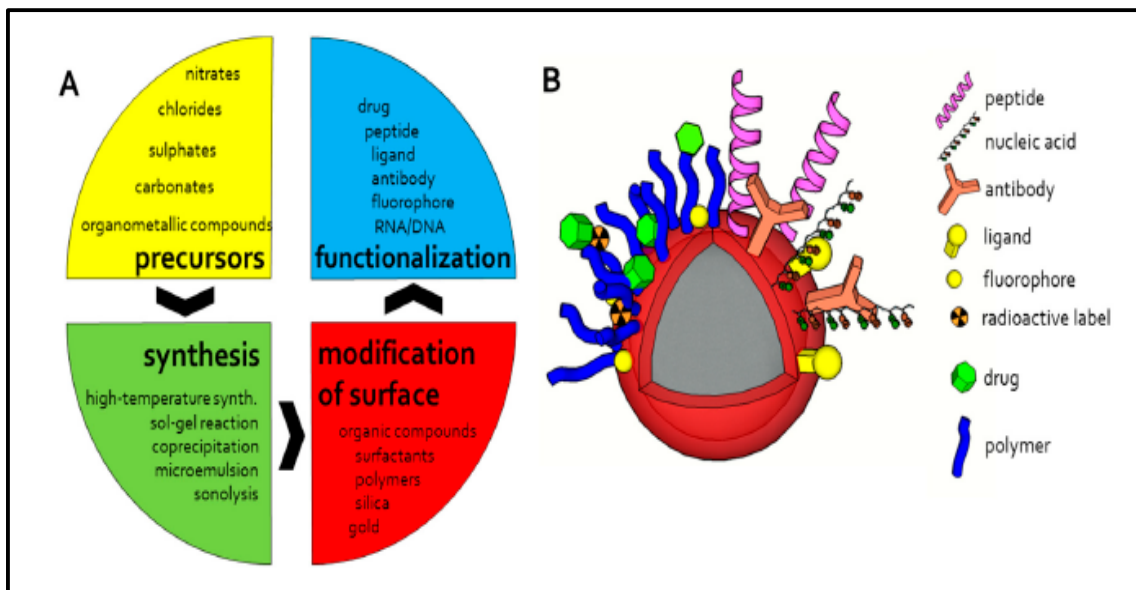


Figure 4.3 Scheme of a) magnetic particles design workflow and b) modification of magnetic particles [39]

4.2 Iron Based Magnetic Aluminium Oxide Nanocomposites, Properties and Applications

By combining two or more kinds of materials, it is possible to develop new nanocomposites with synergetic and improved properties [4]. Metal matrix nanocomposites is one of the advanced materials due to their improved properties such as high specific strength, specific modulus, good wear, damping capacity and corrosion resistance [44].

The magnetic nanoparticles and their composites indicate high saturation magnetization and high coercivity [45]. Therefore, several researches have studied on synthesis of Fe and its alloys as magnetic nanocomposites and analysed their properties [46]. In comparison to other magnetic metal particles, the iron particle has a high magnetization.

However, the oxidation problem and low coercivity are disadvantages of iron particles. The oxidation problem can be prevented by embedding iron nanoparticles into aluminium oxide nanoparticles. The iron nanoparticles exhibit higher coercivity than bulk iron particles and this feature can be a positive impact for commercial applications [45].

The phase transition temperature can be decreased by doping α -Fe₂O₃ with aluminium oxide; because of Fe atoms in solid solutions changed the properties of aluminium oxide [47]. For example, Kobayashi et al. [48] reported that adding a small amount of Fe₂O₃ to Al₂O₃ developed the catalyst stability and catalytic activity of nanocomposites.

Aluminium oxide nanoparticles can be used to enhance weaknesses of Fe and/or Fe related particles. For example, soft magnetic nanocomposites which include highly pure Fe or alloy powders are used for coating and their low melting temperatures can be problematic because of the insufficient insulations of powders. Using of Al₂O₃ on magnetic nanoparticle synthesis provides excellent electrical insulations, thermal conductivity and heat resistance characteristics to nanocomposites [49].

Iron based magnetic aluminium oxide nanocomposites easily separated from the liquid phase by applying a magnetic field with their magnetic properties. In this sense, these nanocomposites are increasing attention for many applications [5]. These features give advantages to magnetic nanocomposites for utilizing them in several applications such as catalyst, ferrofluids, clinic drug delivery magnetic storage media, effective adsorbents and etc. [4], [45], [46]. For example, some nanocomposites are used as adsorbents and magnetic supports in the environmental and biotechnology areas [4].

The magnetic metal oxide nanoparticles are often synthesized by physical methods such as high-energy ball milling and chemical methods, which include sol-gel method, wet impregnation method, hydrothermal method and solution combustion method [4], [45], [50].

- The magnetic phase is formed inside the ceramic matrix using precursors in the form of colloidal magnetic oxides. The aggregations of magnetic nanoparticles can be decreased by sol-gel synthesis [4].
- Wet impregnation method based on impregnated supports calcination to produce magnetic nanocomposites [4].

- In hydrothermal method, nanomaterials or nanocomposites are synthesized at high pressure and elevated temperature. Teflon lined pressure pot which called as autoclave used at hydrothermal synthesis method [50].
- The solution combustion method is used to synthesize aluminium oxide nanopowders and its alloys. The main parameters influencing the reaction are fuel type, oxidizer to fuel ratio, pH of solution, heating rate and etc. [47].

The synthesis method of nanoparticles and nanocomposites were given in Chapter 1.3.



ADSORPTION

Adsorption is widely used phase transfer process, which remove substances from gasses or liquids phases. The most general definition of adsorption is an enrichment of chemical substances on the liquid or solid surface. The schematic view of adsorption theory was represented in Figure 5.1.

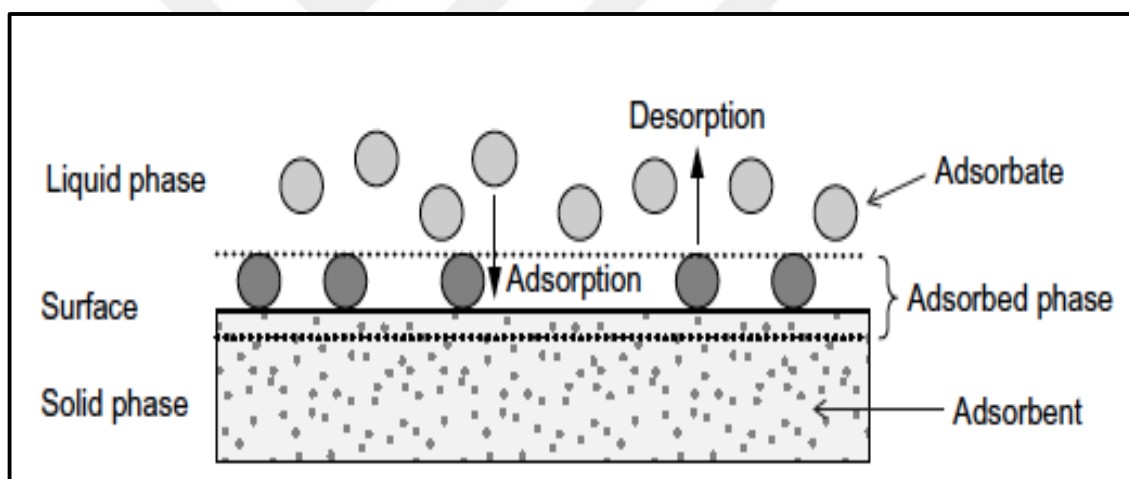


Figure 5.1 Basic terms of adsorption [51]

The solid materials ensure the surface for adsorption is called as adsorbent and the things that will adsorb are named as adsorbate. The adsorbed species can release from the surface of adsorbent to the liquid phase by changing the properties of the liquid phase. This process is named as desorption [51].

There are many chemical, biological and physical treatment techniques to remove pollutants from wastewaters such as adsorption, coagulation, chemical oxidation, membrane separation, electrochemical, microbial degradation and etc. These methods have several disadvantages like utilization of synthetic chemicals, formation of undesired products, being expensive and etc. However, adsorption is commonly

preferred technique due to its cheapness and high-quality of the treated effluents [51], [52]. The advantages and disadvantages of various methods of dye removal were shown in Table 5.1.

Table 5.1 The advantages and disadvantages of various removal methods [52]

Methods	Advantages	Disadvantages
Chemical Treatments		
Oxidative process	Simplicity of application	H ₂ O ₂ required for activation
Ozonation	Application in its gaseous phase	Short half-life (20 min)
Photochemical	Sludge does not produce bad odours	Formation of by-products
Electrochemical destruction	Sludge does not consume chemicals	High flow rates due to dye decreasing rapidly
Biological Treatments		
Decolourization by white-rot fungi	White-rot fungi are able to degrade dyes using enzymes	Enzyme production has also been shown to be unreliable
Adsorption by microbial biomass	Certain dyes have a particular affinity for binding by microbial species	Not effective for all dye types
Anaerobic textile-dye bioremediation systems	Allows azo and other water soluble dyes to be decolorized	Production of methane and hydrogen sulphide
Physical Treatments		
Adsorption by activated carbon	High removal of wide variety of dyes	Very expensive
Membrane filtration	Removal of all dye types	Concentrated sludge production
Ion exchange	No adsorbent loss	Not effective for all dye types
Irradiation	Effective oxidation at lab scale	Requires a lot of dissolved oxygen
Electrokinetic coagulation	Economically feasible	High sludge production

Adsorption process is commonly used in waste water treatment. Treatment process of waste water is required in several fields and targeted pollutants can be various (Table 5.2).

Table 5.2 Adsorption process in water treatment [51]

Application field	Target pollutants to be removed
Drinking water treatment	Organic matter Organic micropollutants Arsenic
Urban wastewater treatment	Phosphate Micropollutants
Industrial wastewater treatment	Specific chemicals
Swimming-pool water treatment	Organic substances
Groundwater remediation	Organic substances
Aquarium water treatment	Organic substances
Landfill leachate treatment	Organic substances

One of the most important parameters on adsorption capacity and mechanism is the pore feature of the adsorbent. Pores can be classified according to pore types or pore sizes. Pore types classification shown in Figure 5.2. As can be seen from Figure 5.2, the pores communicating with the external surface are named open pores, like (b), (c), (d), (e), (f) and the pores do not have any communications with external surface are called as closed pores like (a). Closed pores causes by insufficient heating and are not associated with adsorption and permeability of molecules. However, closed pores influences the mechanical properties of solid materials [53].

There are various classification types of pore sizes described in literature such as IUPAC, Dubinin [54], Cheremskoj [55], Kodikara [56] and etc. The most frequently used pore size classification, IUPAC, was tabulated in Table 5.3.

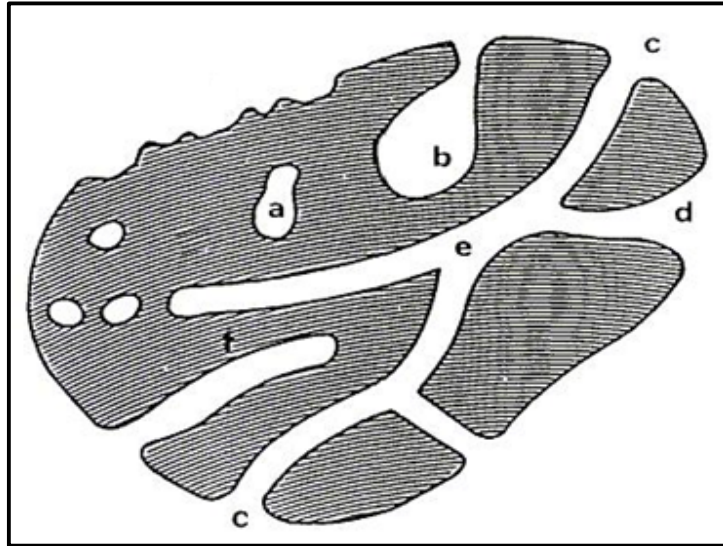


Figure 5.2 Schematic pores classification from IUPAC [53]

Table 5.3 IUPAC pore size classifications [53]

Specified types of pores	Pore Diameter (nm)
Macro-	> 50
Meso-	2 - 50
Micro-	< 2
Supermicro-	0.7 - 2
Ultramicro-	< 0.7
Submicro-	< 0.4

5.1 Adsorption Types

Adsorption can be categorized as physical adsorption (physisorption) and chemical adsorption (chemisorption). Physical adsorption is caused by Van der Waals forces as a weak interaction (dipole-dipole interactions, dispersion forces and induction forces). Physisorption enthalpy is mostly lower than 50 kJ/mol. Chemisorption is based on chemical reactions between the adsorbate and surface of the adsorbent. The adsorption enthalpy is mostly higher than 50 kJ/mol [51]. The difference between physical and chemical adsorption types are listed in Table 5.4.

Table 5.4 Differences between physical and chemical adsorption [57]

Property	Physical adsorption	Chemical adsorption
Activation energy	Very low (close to zero)	High (similar to chemical reactions)
Chemical change of adsorbent	None	A surface compound formation
Specificity of adsorbate-adsorbent interactions	Very low	High
Formation of multilayers	Yes	No
Reversibility	Full reversible	Irreversible

5.2 Adsorption Isotherm Models

The adsorption isotherm models are important for description of how the adsorbate interacts with the adsorbent and the calculation of the adsorbent's adsorption capacity. The surface phase is considered as a monolayer or multilayer [52], [58].

The adsorption capacity was calculated from the following equation:

$$q_e = \frac{(c_0 - c_e) \cdot V}{m} \quad (5.1)$$

Where; q_e is the adsorption capacity (mg/g), c_0 is the initial concentration of adsorbate (mg/L), c_e is the equilibrium concentration of adsorbate in the solution (mg/L), V is the solution volume (L) and m is the mass of adsorbent (g) [58].

5.2.1 Freundlich Isotherm Model

Herbert Max Finley Freundlich was presented an empirical adsorption isotherm in 1906. Freundlich isotherm model definition is the isothermal exchange of adsorption with a unit mass of solid adsorbent of some adsorbent [59]. This empirical model can be applied to multilayer adsorption with non-uniform distribution of adsorption [60]. Freundlich isotherm is presented by the following equation:

$$q_e = k_f \cdot c_e^{1/n} \quad (5.2)$$

Where; q_e is the amount of adsorbate adsorbed at equilibrium (mg/g), k_f is the Freundlich affinity coefficient ($\text{mg}^{1-1/n} \cdot \text{L}^{1/n} \cdot \text{g}^{-1}$), c_e equilibrium concentration (mg/L), and n is the Freundlich exponential coefficient [58].

The linearized form of Equation (5.2) is:

$$\ln q_e = \ln k_f + \frac{1}{n} (\ln c_e) \quad (5.3)$$

5.2.2 Langmuir Isotherm Model

Irving Langmuir developed a relationship between amount of gas adsorbed on the surface and pressure of gas. Langmuir equation is a semi-empirical isotherm and derived from a proposed kinetic mechanism. Langmuir kinetic is based on some assumptions such as uniform surface and constant temperature and the ideal monolayer adsorbed model [52], [58].

Langmuir isotherm equation is represented by the following equation:

$$q_e = \frac{q_m b c_e}{1 + b c_e} \quad (5.4)$$

Where; q_e is the amount of adsorbate adsorbed at equilibrium (mg/g), c_e is the concentration of adsorbate at equilibrium (mg/L), q_m is the maximum adsorption capacity of the adsorbent (mg/g) and b is the Langmuir adsorption constant related to adsorption energy (L/mg) [52].

The linearized form of Equation (5.4) is:

$$\frac{1}{q_e} = \frac{1}{q_m} + \frac{1}{b q_m} \left(\frac{1}{c_e} \right) \quad (5.5)$$

The rearranged form of Equation (5.5) is:

$$\frac{c_e}{q_e} = \frac{c_e}{q_m} + \frac{1}{b q_m} \quad (5.6)$$

5.2.3 Temkin Isotherm Model

Temkin isotherm model is the early model describing the adsorption of hydrogen in the acidic solutions with platinum electrodes. This equation is characterized by a uniform distribution of binding energies. Temkin isotherm model is appropriate for predicting the gas phase equilibrium however, the liquid-phase adsorption as a complex adsorption system are usually not appropriate to be represented [60].

Temkin isotherm model is represented by the following equation:

$$q_e = \frac{RT}{b_T} \ln A_T c_e \quad (5.7)$$

Where q_e is the amount of adsorbate in the adsorbent at equilibrium (mg/g), c_e is the concentration of adsorbate at equilibrium (mg/L), R is the ideal gas constant (8.314 J/mol.K), T temperature (K), b_T is the Temkin constant related to adsorption temperature (J/mol) and A_T Temkin isotherm equilibrium binding constant (L/g) [60].

The linearized form of Equation (5.7) is:

$$q_e = \frac{RT}{b_T} \ln A_T + \frac{RT}{b_T} \ln c_e \quad (5.8)$$

5.3 Adsorption Kinetic Models

Adsorption kinetic models are used to determine the rate of adsorption by using adsorbate concentration at a specific time [58]. The adsorption rate constant is a great important factor on the selection of the adsorbent will be used in the adsorption process. Desired adsorbent should have a large adsorption capacity and fast adsorption rate [52]. First order reaction model, pseudo-first order reaction model, second order reaction model and Pseudo-second order model are used for evaluating the kinetic coefficient of the adsorption phenomena [52], [58].

5.3.1 First Order Reaction Model

First order reaction model based on the solution concentration is given as:

$$-\frac{dc_t}{dt} = k \cdot c_t \quad (5.9)$$

Where; c_t is the concentration at contact time (mg/L), c_0 is the initial concentration (mg/L) and k is the first order adsorption rate constant.

The linearized form of Equation (5.9) is:

$$\ln c_t = \ln c_0 - kt \quad (5.10)$$

5.3.2 Pseudo-First Order Reaction Model

Pseudo-first order reaction model is based on adsorption capacity. Pseudo-first order reaction model can be represented as:

$$\frac{dq_t}{dt} = k_1(q_e - q_t) \quad (5.11)$$

Where; q_e is adsorption capacity at equilibrium time, q_t is the adsorption capacity of any time and k_1 is the pseudo-first order adsorption rate constant [58].

The linearized form of Equation (5.11) is:

$$\log(q_e - q_t) = \log q_e - \frac{k_1}{2.303} t \quad (5.12)$$

5.3.3 Second Order Reaction Model

Second order reaction model fits adsorption process in general and it is expressed as:

$$-\frac{dc_t}{dt} = k_2 c_t^2 \quad (5.13)$$

Where c_t is the concentration at a contact time (mg/L), c_0 the initial concentration (mg/L) and k_2 is the second order adsorption rate constant [58].

Rearranging of Equation (5.13) and integrating it for the boundary conditions $t = 0$ to $t = t$ and $c_t = 0$ to $c_t = c_t$:

$$\frac{1}{c_t} - \frac{1}{c_0} = k_2 \cdot t \quad (5.14)$$

5.3.4 Pseudo-Second Order Reaction Model

Pseudo-second order reaction model is based on the adsorption capacity and can be expressed as:

$$\frac{dq_t}{dt} = k_{p2}(q_e - q_t)^2 \quad (5.15)$$

Where; q_t is the adsorption capacity of any time (mg/g), q_e is the adsorption capacity at equilibrium time (mg/g) and k_{p2} is the pseudo-second order adsorption rate constant [58].

Rearranging of Equation (5.15) and integrating it for the boundary conditions $t = 0$ to $t = t$ and $q_t = 0$ to $q_t = q_t$:

$$\frac{t}{q_t} = \frac{1}{k_{p2} \cdot q_e^2} + \frac{1}{q_e} t \quad (5.16)$$

5.3.5 Elovich Model

The Elovich equation is mainly applicable for chemisorption kinetics. The Elovich model is expressed as:

$$\frac{dq_t}{dt} = \alpha e^{-\beta q_t} \quad (5.17)$$

Where q_t is the adsorption capacity of any time (mg/g), q_e is the adsorption capacity at equilibrium time (mg/g) α is the initial adsorption rate (mg g⁻¹ min) and β is the constant related to extent of surface coverage and the activation energy (g mg⁻¹) [61].

Rearranging of Equation (5.17) and integrating it for the boundary conditions $t = 0$ to $t = t$ and $q_t = 0$ to $q_t = q_t$:

$$q_t = \frac{1}{\beta} \ln(\alpha\beta) + \frac{1}{\beta} \ln t \quad (5.18)$$

5.3.6 Intra-particle Diffusion Model

The intra-particle diffusion model was applied to describe the competitive adsorption. This model is expressed as:

$$q_t = k_i t^{0.5} + c_i \quad (5.19)$$

Where q_t is the adsorption capacity of any time (mg/g), k_i intra-particle diffusion rate constant ($\text{mg g}^{-1} \text{min}^{-2}$) and c_i is the constant related to layer thickness (mg g^{-1}) [61].

5.4 Types of Adsorption Isotherms

5.4.1 Classification of Gas Physisorption Isotherms

There are many experimental adsorption isotherms for different gas-solid systems. Adsorption isotherms characteristic shapes are important, because they provide useful information about the pore structure of the adsorbent. The majority of vapour isotherms may be divided into nine groups in an extended IUPAC classification (Figure 5.3) [62].

- The Type I(a) and I(b) isotherm models are reversible and concave relative pressure (P/P^0) axis. They are obtained with microporous adsorbents. Type I(a) corresponds to filling of narrow micropores, while Type I(b) indicates the presence of wider micropores.
- The Type II isotherms are concave relative pressure axis and their shape are obtained with non-porous or a macroporous adsorbent. Type II(a) isotherm have not adsorption hysteresis and complete reversibility of the desorption-adsorption isotherm. However, Type II(b) have Type H3 hysteresis. A number of powders or aggregates give Type II(b) isotherms such as clays, pigments, cements and etc. [62].
- The reversible Type III isotherm is convex to the relative pressure axis. This type of isotherm is not common and indicates on non-porous or macroporous adsorbent [63].
- The Type IV(a) and IV(b) isotherms are obtained with mesoporous adsorbents. Type IV(a) isotherms are much more common than Type IV(b) and exhibits hysteresis loops. However, the shape of the Type IV(b) hysteresis loops varies from

one system to another. Type IV(b) isotherms are completely reversible and obtained with a few ordered mesoporous structures [62].

- The Type V isotherms are uncommon. They are obtained with certain porous adsorbents; however, it is known that the adsorbent adsorbate interactions are weak.
- The Type VI isotherm have sharpness of the steps depends on the systems and the temperature. They are represents multilayer adsorption on a uniform non-porous surface [63].

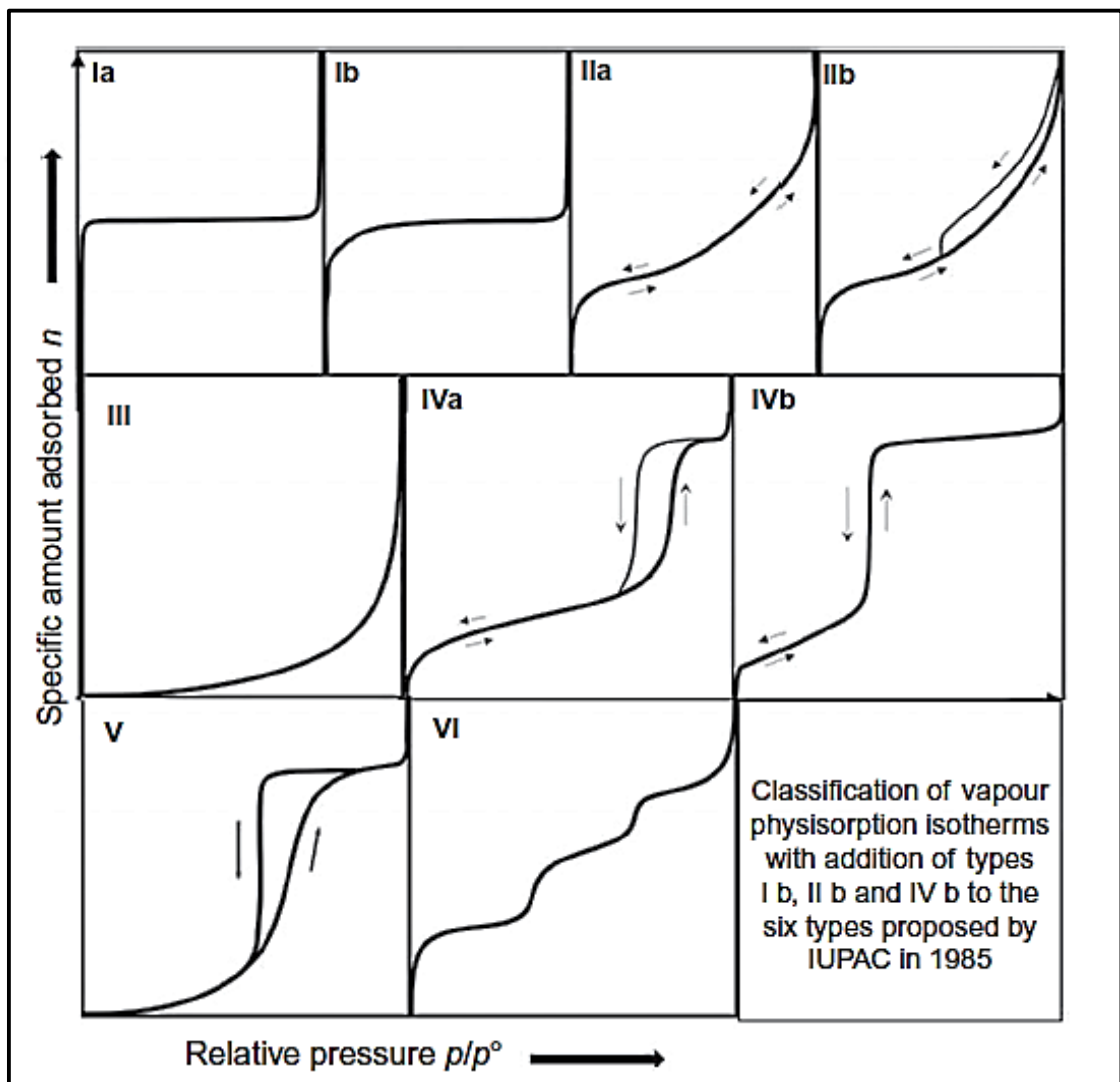


Figure 5.3 Classification of vapour adsorption isotherms from IUPAC [62]

5.5 Dye Removal by Adsorption

There are many techniques, which include adsorption, flocculating combined with flotation, membrane filtration, electrokinetic processes, coagulation, ozonation, oxidation, precipitation and ion-exchange for dye removal from waste water. Adsorption techniques are more preferable among other techniques used because of their stable efficiencies in the removal of pollutants and being affordable processes [52], [64].

Adsorption of dyes depends on the properties of dye and the surface chemistry of the adsorbent. Physical conditions of the solution such as pH, temperature, initial dye concentration and adsorbent amount are main factors on the effectiveness of dye adsorption. Optimization of the process conditions will greatly help to progress of the industrial-scale dye removal treatment [52], [65].

Although all the other parameters have an impact on adsorption process of dye, pH is the most important factor and it is related to the ionic feature of the dye. For example, a high pH value is preferred for cationic dye adsorption while a low pH value is preferred for anionic dye adsorption [52].

EXPERIMENTAL DESIGN

Experimental design, or design of experiments, is a structured and systematic approach to determine the effects of experimental variables on system. Experimental design is useful for developing and optimizing a wide range of engineering systems. Generally, there are four different fields for experimental design such as, comparative, screening/characterization, modelling and optimizing [66], [67].

The conventional and classical methods are also time consuming and require a lot of experiments for determination of optimum condition to be examined. The limitations of these methods can be eliminated by optimizing all the affecting parameters by experimental design such as response surface methodology (RSM) [68].

Experimental design was first introduced by Ronald Fisher in the 1930s though factorial designs for agricultural and biological research. Response surface methodology was first mentioned in the 1950s by Box and Wilson. The experimental design process flow chart was illustrated in Figure 6.1 [67].

The application of experimental design techniques in adsorption process can result in increased product efficiency and confirmation of output response to target requirements, decreased overall costs process instability and time [68].

The experimental design can be classified into two categories. These are one-factor-at-a-time design (single-factor design) and factorial design (multiple-factor design). One-factor-at-a-time design is a traditional design, which investigates one-factor-at-a-time, while keeping the levels of other factors constant. On the contrary, factorial design is able to study the effects of more than one factor at two or more levels [69].

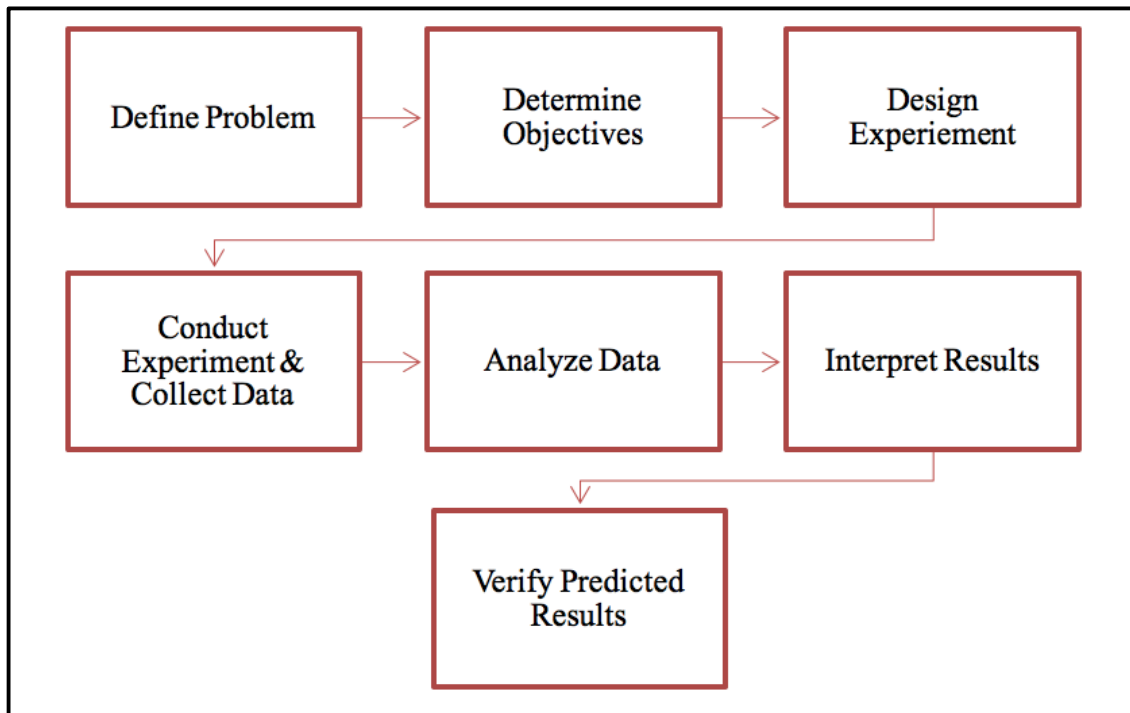


Figure 6.1 The flow chart of experimental design process [70]

6.1 Response Surface Methodology

Response surface methodology is a collection of statistical and mathematical methods for the modelling of engineering problems. Response surface methodology can be used to evaluate the significance of several factors in complex interactions. The main objective of this methodology, optimize to response surface which is influenced by various process parameters. Briefly, the response surface methodology determines the relationship between the input parameters and the obtained response surfaces. The response surface methodology design procedure is as follows:

- Designing of series of experiments for sufficient and reliable measurement
- Developing a mathematical model with best fittings
- Finding the favourable set of experimental parameters
- Representing the direct and interactive effects of process parameters

The response surface can be expressed as follows:

$$y = f(x_1, x_2, x_3, \dots, x_k) \quad (6.1)$$

Where; y is the answer of system, and x_i the variables of action called factors.

To optimize the response variable, y , a second-order model is used in response surface methodology as given in Equation (6.2).

$$y = \beta_0 + \sum_{i=1}^k \beta_i x_i + \sum_{i=1}^k \beta_{ii} x_i^2 + \sum_{i=1}^{k-1} \sum_{j=2}^k \beta_{ij} x_i x_j + \varepsilon \quad (6.2)$$

where x_1, x_2, \dots, x_k are the input factors which influence the response y ; β_0, β_{ii} ($i = 1, 2, \dots, k$), β_{ij} ($i = 1, 2, \dots, k ; j = 1, 2, \dots, k$) are unknown parameters and ε is a random error [71].

6.2 Box-Behnken Design Method

Box-Behnken design is rotatable second-order design based on three-level incomplete factorial designs. This design requires an experiment number according to Equation (6.3);

$$N = k^2 + k + c_p \quad (6.3)$$

Where; k is the factor number and c_p is the replicate number of the central point. Box-Behnken is spherical and revolving design. As shown in Figure 6.2, it consists of a central point and the middle points of the edges. However, it can also be viewed as consisting of three interlocking 2^2 factorial design and central point [71].

The Box-Behnken design method provides an economical alternative compared to the other design methods. Because, it has less factor level and does not include extreme high or low levels.

Based on the analysis of variance (ANOVA) of the estimated models, the significant terms effects on the response can be determined. Besides, the optimal response can be estimated by calculating the derivatives of the model [69].

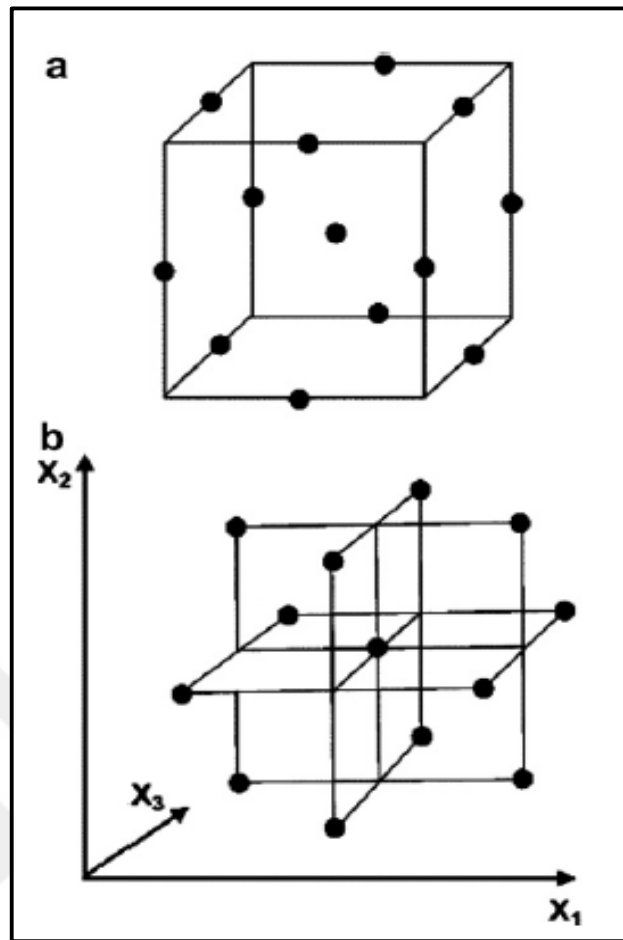


Figure 6.2 a) Box-Behnken design as derived from a cube and b) Box-Behnken representation of 2^2 factorial design [71]

LITERATURE SURVEY

7.1 Literature Survey on Aluminium Oxide Nanoparticles Synthesis by Solution Combustion Method

Synthesis of aluminium oxide nanoparticles is popular because of their superior properties. There are various methods for aluminium oxide nanoparticles synthesis. However, solution combustion method has more advantages than the other synthesis methods as mentioned in Chapter 2.2.2.5. In this section, the studies taken from the literature on the synthesis of aluminium oxide nanoparticles by solution combustion method were summarized.

Fazli et al. (2016) [72] in their study, synthesized aluminium oxide nanoparticles using aluminium nitrate as an oxidizer and urea, ammonium acetate and ammonium nitrate as fuel types. They used stoichiometric amount of starting materials to synthesize aluminium oxide nanoparticles and then, the prepared solutions were heated in a pre-heated furnace at 400°C. The samples synthesized using ammonium acetate and ammonium nitrate were calcined at 700 °C. The fuel effects on properties of aluminium oxide nanoparticles were investigated and characterized by X-ray diffraction (XRD), Scanning electron microscopy (SEM), Thermogravimetric analysis (TG) and Brunauer Emmet Teller (BET). From characterization studies, synthesized sample using ammonium acetate as a fuel was in the form of γ -Al₂O₃ with high specific surface area (200 m²/g) and fine particle size. However, they found that synthesized sample using urea as a fuel was in the form of α -Al₂O₃ with a surface area of 18.4 m²/g.

Farahmandjou and Golabiyani (2015) [73] in their study, aluminium oxide nanoparticles were synthesized using aluminium nitrate as precursor and glycine as fuel by solution combustion method. Their combustion reaction occurred at temperature 100 °C and proceeded for 3 hours. Subsequently, the synthesized samples were subjected to a temperature of 600 °C and 1000 °C for determination of the phase transformation. The samples were characterized by X-ray diffraction (XRD), Transmission electron microscopy (TEM), Field effect scanning electron microscopy (FESEM), and Ultraviolet-visible spectrophotometer (UV-Vis). Synthesized aluminium oxide at 1000 °C was founded as alpha phase according to XRD result and particle size was determined as 80 nm from SEM images.

Sharma et al. (2014) [74] in their study, aluminium oxide nanoparticles were synthesized by solution combustion method at the temperature range from 350 to 450 °C using mixed fuel. They utilized various fuels to oxidizer ratio of urea and glycine. They obtained nanophase aluminium oxide powder with wide range particle size distribution in nanoscale. They concluded that the increase in urea amount promotes crystallinity.

Ramesh et al. (2013) [75] synthesized aluminium oxide particles under different fuel to oxidizer molar ratios by microwave assisted combustion synthesis method. Aluminium nitrate and glycine were used as oxidizer and reducing agent (fuel), respectively. The mixture solution, which include oxidizer and fuel, were introduced into a microwave oven at 2.45 GHz for 4 min. After microwave treatment, samples calcined at 800, 900, 100 and 1200 °C respectively. The prepared powders were analysed by X-ray diffraction (XRD), Fourier transform infra-red (FT-IR), Thermogravimetric and differential scanning calorimetry (TG/DSC) and Transmission electron microscopy (TEM). They reported that microwave assisted combustion synthesis technique provides pure, homogeneous and nanocrystalline Al₂O₃ particles. They concluded that Al₂O₃ powders crystallite size increase 38 nm to 52 nm as the calcination temperature is increasing 900 °C to 1200 °C.

Sherikar and Umarji (2013) [76] reported the synthesis of nanocrystalline γ -Al₂O₃ powders using aluminium nitrate as oxidizer and a mixture of urea and glycine as a fuel by solution combustion method. They prepared samples, which include various amount of glycine in stoichiometric ratio of urea as fuel, in preheated 500 °C furnace. They calculated enthalpy of combustion and the theoretical variation of adiabatic flame

temperature for different ratios of both fuels. XRD, SEM and TEM were used for determining the phase formation and morphology of powders. They obtained single phase gamma aluminium oxide particles from the reaction which also include 20 wt. % of glycine together with urea and average crystalline size of these particles were determined as ~5 nm by XRD.

Sharma et al. (2012) [77] reported synthesis of aluminium oxide powder using various amount of glycine as a fuel. Each sample was subjected to furnace heating in temperature range 350 to 450 °C in solution combustion method. Then the samples they produced were characterised using XRD and SEM. According to XRD analysis of synthesized aluminium oxide powder, it was concluded that the glycine fuel provides the generation of amorphous structure of aluminium oxide.

Moreno-Marcelino et al. (2012) [78] compared the effects of solid combustion and solution-combustion processes on aluminium oxide synthesis. They used various amount of urea as fuel in a muffle furnace at 800 °C for both methods. The characterization of samples was carried out using XRD for phase determination and Brunauer Emmet Teller (BET) for surface area. They reported that γ -Al₂O₃ showed a non-crystalline structure and had very high surface area for the samples with low content of urea. According to BET result, the largest surface area of γ -Al₂O₃ particles obtained by solution combustion method was reported as 275 m²/g.

Saket et al. (2010) [79] compared the furnace and microwave combustion processes for aluminium oxide synthesis. For this purpose, they used specified amount of urea and aluminium acetate as a fuel. The prepared solutions were placed into a microwave oven with power of 900 W and also into a furnace at 350 °C and 400 °C, respectively. They confirmed that synthesis by furnace at 400 °C ensures well crystallized α -Al₂O₃. On the other hand, synthesis by microwave provided non-crystalline aluminium oxide which needed extra heating at 900 °C for 1 h. Moreover, they reported that the crystalline size of the samples which were synthesized by microwave assisted method are smaller than the particles obtained from furnace assisted, as 50 nm and 110 nm, respectively.

Freitas et al. (2006) [80] studied three fuel compositions with stoichiometric, 10 % and 20 % of urea reduction to synthesize α -Al₂O₃ powders by solution combustion method. Each mixture was heated on a hot plate at temperature of 480 °C. Generated aluminium oxide powders were characterized by XRD, specific surface area and average particle

size were determined by BET method. The size distributions of powders were analysed by sedimentation method and microstructure of the samples were characterised by SEM. They confirmed that the single phase crystalline α -Al₂O₃ was formed for each compositions used. Additionally, they reported that according to data obtained from XRD analysis, the crystallinity degree of the particles decreased with the reduction of urea content. From BET analysis, the specific surface areas of synthesized samples increased from 99.98 m²/g to 114.09 m²/g with reduction of urea in the combustion reactions. According to SEM images, the formation of agglomerates with sharp, irregular and fine α -Al₂O₃ particles were obtained.

The main findings of the studies mentioned above on the synthesis of aluminium oxide nanoparticles by solution combustion method were summarized in Table 7.1.

Table 7.1 Various studies on synthesis of aluminium oxide nanoparticles by solution combustion method

Reference	Starting Materials		Stoich. fuel (%)	Combustion Reaction Parameters			Calcination Temp. (°C)	Characterization studies	
	Oxidizer	Fuel		Heating System	Temp. / Power	Time (min)		XRD Analysis	Mean size (nm)
Fazli et al. (2016) [72]	Al(NO ₃) ₃	Urea	Stoichiometric ^(a)	Furnace	400 °C	-	-	α-Al ₂ O ₃	-
		AA					700	γ-Al ₂ O ₃	-
		AN					700	γ-Al ₂ O ₃	-
Farahmandjou and Golabiyan (2015) [73]	Al(NO ₃) ₃	Glycine	-	-	100 °C	180	600	-	35
							1000	α-Al ₂ O ₃	80
Sharma et al. (2014) [74]	Al(NO ₃) ₃	Urea, Glycine	20 G + 20 U ^(a) 10 G + 30 U ^(a) 40 G + 40 U ^(a) 20 G + 60 U ^(a) 60 G + 60 U ^(a) 30 G + 90 U ^(a)	Furnace	350-450 °C	-	-	-	50 - 150
Ramesh et al. (2013) [75]	Al(NO ₃) ₃	Glycine	High level ^(a) Stoichiometric ^(a) Low level ^(a)	MW	2.45 GHz	4	800	-	-
							900	γ, α, δ-Al ₂ O ₃	38 - 52
							1000	γ, α, δ-Al ₂ O ₃	
							1200	α- Al ₂ O ₃	

^(a) G: Glycine U: Urea, AA: Ammonium acetate, AN: Ammonium nitrate molar ratio of fuels, ^(b) G: Glycine U: Urea, weight percentages of fuel, ^(c) The results obtained by Mastersizer particle size analyser, ^(d) The results given for crystalline sizes of particles obtained from XRD analysis

Table 7.1 Various studies on synthesis of aluminium oxide nanoparticles by solution combustion method (cont'd)

Reference	Starting Materials		Stoich. fuel (%)	Combustion Reaction Parameters			Calcination Temp. (°C)	Characterization studies	
	Oxidizer	Fuel		Heating System	Temp. / Power	Time (min)		XRD Analysis	Mean size (nm)
Sherikar and Umarji (2013) [76]	Al(NO ₃) ₃	Urea, Glycine	U + 0 G ^(b) U + 10 G ^(b) U + 20 G ^(b) U + 30 G ^(b) U + 40 G ^(b)	Furnace	500 °C	-	-	α, γ-Al ₂ O ₃	300
Sharma et al. (2012) [77]	Al(NO ₃) ₃	Glycine	40 G ^(a) 80 G ^(a) 120 G ^(a)	Furnace	350-450 °C	-	-	-	50 - 150
Moreno-Marcelino et al. (2012) [78]	Al(NO ₃) ₃	Urea	100 U ^(b) 150 U ^(b) 200 U ^(b) 250 U ^(b)	Muffle furnace	800 °C	-	-	α, γ-Al ₂ O ₃	-
Saket et al. (2010) [79]	Al(NO ₃) ₃	Urea, AA	25 AA+75 U ^(a)	Furnace	350-400 °C	-	-	α, γ-Al ₂ O ₃	12000 ^(c)
				MW	900 W	-	900	α, γ-Al ₂ O ₃	19000 ^(c)
Freitas et al. (2006) [80]	Al(NO ₃) ₃	Urea	100 U ^(a) 90 U ^(a) 80 U ^(a)	Hot plate	480 °C	-	-	α-Al ₂ O ₃	12– 25 ^(d)

^(a) G: Glycine U: Urea, AA: Ammonium acetate, AN: Ammonium nitrate molar ratio of fuels, ^(b) G: Glycine U: Urea, weight percentages of fuel, ^(c) The results obtained by Mastersizer particle size analyser, ^(d) The results given for crystalline sizes of particles obtained from XRD analysis

7.2 Literature Survey on Iron Based Magnetic Aluminium Oxide Nanocomposites Synthesis by Solution Combustion Method

Iron based magnetic aluminium oxide nanocomposites are used in a great variety of application areas such as catalyst, ferrofluids, clinic drug delivery magnetic storage media, effective adsorbents and etc. (detailed given in Chapter 4.2). In this section, the studies taken from the literature on the synthesis of iron based magnetic aluminium oxide nanocomposites by solution combustion method were summarized.

Zhang et al. (2012) [81] used stoichiometric compositions of $\text{Fe}(\text{NO}_3)_3$, $\text{Al}(\text{NO}_3)_3$ as oxidizers and urea as a fuel for preparation of $\text{Fe}_2\text{O}_3/\text{Al}_2\text{O}_3$ nanocomposites. For this purpose, firstly, the mixture which include oxidizer and fuel, stirred on hot plate at 60 °C. Secondly, viscous sol formed was dried at 110 °C and then the sample was transferred to preheated muffle furnace at 600 °C. Finally, burn products calcined at 950 °C for 2 h. The characterization studies of synthesis samples were performed by FT-IR, TGA-DTA, BET, XRD, SEM and TEM. They concluded that calcination for 2 h was necessary step to obtain $\text{Fe}_2\text{O}_3/\text{Al}_2\text{O}_3$. The average pore size and surface area were found as 64.76 nm and 4.01 m^2/g , respectively.

Kakooei et al. (2012) [47] prepared iron-doped Al_2O_3 ($\text{Fe-Al}_2\text{O}_3$) using stoichiometric amounts of aluminium nitrate ($\text{Al}(\text{NO}_3)_3$), iron nitrate ($\text{Fe}(\text{NO}_3)_3$) and sucrose ($\text{C}_{12}\text{H}_{22}\text{O}_{11}$). The prepared mixture was heated on a hot plate until the excess water evaporated and then, subjected to heat treatment at 900 °C and 1100 °C separately to obtain $\alpha\text{-Al}_2\text{O}_3$ powders. Synthesized powders characterized by XRD, DTA, SEM and EDS. $\alpha\text{-Al}_2\text{O}_3$ was formed at 1100 °C and its average crystalline size was obtained as 38.94 nm according to characterization studies. They concluded that sucrose was good dispersion agent and carbon source for synthesis of iron aluminium oxide nanoparticles.

Wang et al. (2011) [82] prepared $\text{Fe}_2\text{O}_3/\text{Al}_2\text{O}_3$ by combining sol-gel technique and solution combustion synthesis using stoichiometric compositions of $\text{Al}(\text{NO}_3)_3$ and $\text{Fe}(\text{NO}_3)_3$, and urea as a fuel. The mixture of $\text{Al}(\text{NO}_3)_3$, $\text{Fe}(\text{NO}_3)_3$, and urea was stirred on a hot plate at 75 °C for aged until viscous colloidal suspension (sol) obtained. Then, the sol dried at 80 °C and 135 °C. Next, prepared dried gel was transferred in preheated muffle furnace at 600 °C and kept for 15 min and finally, as-burned product was calcined in same furnace at 950 °C for 2 hours. The characterization studies of

synthesized samples were performed using FT-IR, TGA-DTA, XRD and N₂ isothermal adsorption desorption method. They concluded that calcination was necessary step to obtain α -Fe₂O₃ and α -Al₂O₃.

The main findings of the studies mentioned above on the synthesis of iron based magnetic aluminium oxide nanocomposites by solution combustion method were summarized in Table 7.2.



Table 7.2 Various studies on synthesis of iron based magnetic aluminium oxide nanocomposites by solution combustion method

Reference	Starting Materials		Combustion Reaction Parameters			Calcination Temp. (°C)	Characterization studies	
	Oxidizer	Fuel	Heating System	Temp. (°C)	Time (min)		XRD Analysis	Mean size (nm)
Zhang et al. (2012) [81]	Al(NO ₃) ₃ and Fe(NO ₃) ₃	Urea	Hot plate + Muffle furnace	60 + 110	-	600	α-Al ₂ O ₃ α-Fe ₂ O ₃	100
Kakooei et al. (2012) [47]	Al(NO ₃) ₃ and Fe(NO ₃) ₃	Sucrose	Furnace	350 - 450	-	900	Fe-(γ-Al ₂ O ₃)	38.94 ^(a)
						1100	Fe-(α-Al ₂ O ₃)	
Wang et al. (2011) [82]	Al(NO ₃) ₃ and Fe(NO ₃) ₃	Urea	Hot plate + Muffle furnace	75 + 600	- + 15	950	α-Fe ₂ O ₃ α-Al ₂ O ₃	-

^(a) The results given for crystalline sizes of particles obtained from XRD analysis.

7.3 Literature Survey on Reactive Blue 19 Dye Removal by Adsorption

Removal of Reactive Blue 19 (RB19) dye from textile waste water by adsorption is gained importance in recent years. The numerous adsorbents are used in the adsorption process such as some agricultural and industrial wastes, organic or inorganic based materials. In this section, the studies taken from the literature on the adsorption of Reactive Blue 19 dye were summarized.

Xu et al. (2018) [83] in their work, synthesized chitosan-based magnetic adsorbent (poly(2-(dimethylamino) ethyl methacrylate) grafted magnetic chitosan microspheres, GMCMS) and then, RB19 dye adsorption capacity was investigated onto GMCMS. The effects of initial solution pH and contact time were examined on dye adsorption. Langmuir isotherm model was described the uptake of the Reactive Blue 19. The kinetic studies showed that the removal of Reactive Blue 19 fitted to pseudo-second order model.

Mustafa et al. (2017) [84] in their work used White-rot fungus (*Panus tigrinus*) as a biosorbent for the decolorization of Reactive Blue 19 aqueous solutions. In this process, effects of various parameters such as initial dye concentration (50-150 mg/L), contact time (30-90 min) and pH (2-6) were examined on the dye adsorption. The *Panus tigrinus* showed the maximum removal percentage of relevant dye at pH of 2 as 83.18 %, a contact time of 90 min and an initial concentration 50 mg/L. Langmuir isotherm model was described the uptake of the Reactive Blue 19 dye better than Freundlich isotherm model. The pseudo-second order rate expression was found the best one for describing the kinetic behaviours of dye adsorption process.

Demirhan (2017) [85] optimized the removal of reactive blue 19 dye by using peanut shells. The influences of pH (2, 3 and 4), temperature (25, 35 and 45 °C) and adsorbent amount (0.5, 1 and 1.5/100 mL) were examined by using Box-Behnken design. The removal % of RB19 dye by peanut shell was reported as 93.45 % at pH of 2, 35 °C and 1.5 g/100 mL. Langmuir isotherm model was found better for describing the obtained equilibrium data than Freundlich and Temkin isotherm model. The kinetic studies showed that the removal of Reactive Blue 19 fitted to pseudo-second order model.

Mousa and Taha (2016) [86] carried out the adsorption process for using natural wheat straw (NWS), modified wheat straw (MWS) and activated carbon (AC). The effects of pH (2.5 – 10.5) and the initial dye concentration (5, 20, 30, 50, 70 and 90 mg/L) were determined on adsorption process of Reactive Blue 19 dye. The removal percentages of reactive blue were 68 %, 92.17 % and 90.5 % by using wheat straw, modified wheat straw and activated carbon, respectively. Freundlich isotherm model was described the adsorption of reactive blue dye by using both NWS and MWS. However, Langmuir isotherm defined better the adsorption process of RB19 dye by using AC. Adsorption of Reactive Blue 19 dye was fitted with intra-particle diffusion kinetic model for NWS and MWS and Pseudo-second order kinetic model for AC.

Ciobanu et al (2016) [87] studied the adsorption of Reactive Blue 19 dye on the hydroxyapatite (HAP) nanopowders. The effects of adsorbent dosage, contact time, dye solution, pH and temperature on adsorption process were investigated. The maximum dye uptake was specified as 95.58 % and 86.95 % for uncalcined and calcined HAP, respectively at pH of 3 and 20 °C, after 3 h of contact time. The Langmuir isotherm model was represented the best equilibrium for uncalcined and calcined HAP. The kinetic studies indicated that the Reactive Blue 19 adsorption on relevant samples suits the pseudo-second order model.

Bindary et al. (2015) [88] investigated the adsorption behaviour of Reactive Blue 19 on rice straw fly ash from aqueous solutions. The maximum removal of dye by rice straw fly ash was reported as more than 85 % at pH of 1, for 0.09 g adsorbent dose and 30-100 mg/L dye concentration for 60 min. From the experimental results, the Freundlich isotherm model was determined as the best model for adsorption of reactive blue 19 dye by using rice straw ash as adsorbent. The kinetic data was match to pseudo-second order kinetic model with high correlation coefficients.

Balarak et al. (2015) [89] investigated the effects of various parameters such as contact time (10-180 min), pH of the solution (3-11), adsorbent dosage (0.1-1 g/100 mL) and dye concentration (10-500 mg/L) on adsorption of RB19 dye by using *Lemna Minor* as low-cost adsorbent. They were found that the equilibrium time was 75 min and the maximum dye removal efficiency was obtained at pH of 3. It was reported that Langmuir isotherm model is the best one for describing the measured experimental data.

Dehvari et al (2015) [90] in their study, pomegranate seed powder was used for adsorption of Reactive Blue 19 dye. Pomegranate seed powder was prepared after the steps of washing, boiling, drying, milling and pulverizing. They investigated the effects of the parameters on dye adsorption such as adsorbent dosage, pH and retention time, initial concentration of dye and agitation rate. The removal efficiencies of Reactive Blue 19 dye were equal to 3.21 mg/L (68 %), 4.525 mg/L (81.7 %) and 6.8 mg/L (86 %) at dye concentrations of 10, 25 and 50 mg/L, respectively, at pH of 3. They stated that the increase of adsorbent dose led to decrease of adsorption capacity.

Khoshhesab and Ahmadi (2015) [91] investigated the adsorption potential of NiO nanoparticles for RB19 dye removal from aqueous solutions. During the experimental studies, the effects of adsorbent dosage, dye concentration, solution pH, contact time and temperature were examined. It was reported that NiO nanoparticles exhibited sufficient adsorptive features such as high adsorption capacity, short contact time and independency of pH for RB19 dye removal.

Ghaneian et al. (2014) [92] aimed to define the isotherm and kinetic models for the adsorption of Reactive Blue 19 onto Jujube stems powder from synthetic textile wastewater. They investigated the effects of initial dye concentration, pH, adsorbent dose and contact time during the experimental studies. The maximum removal % of Jujube stems powder was reported as 84 % at pH of 10, 25 mg/L dye concentration and 0.6 g/100 mL adsorbent dose for 180 min. According to the data obtained from the experiments, Langmuir isotherm model was found as the most proper model and the pseudo-second order reaction model was specified as the most fitted kinetic model for the relevant study.

Nguyen and Pho (2014) [93] prepared chitosan coated magnetic hydroxyapatite nanoparticles (CS-MHAP) for the removal of Ni⁺² ions and Reactive Blue 19 textile dye. Effects of contact time, initial dye concentration, CS-MHAP dosage and pH were examined for adsorption of Reactive blue 19 dye. They reported that the all the parameters examined were effective on the absorption capacity of Ni⁺² ions. The best results were obtained at pH of 5 for RB19 dye removal.

Rafiee and Jahangiri-rad (2014) [94] used multi-walled and single-walled carbon nanotubes as adsorbents for removal of Reactive Blue 19 textile dye from aqueous solutions. The effects of pH, shaking time, temperature on adsorption capacity were

investigated. The highest adsorption capacities of multi-walled carbon nanotube (MWCNT) and single-walled carbon nanotube (SWCNT) for RB19 dye removal were found as 450 mg/g and 550 mg/g at pH of 3, 50 °C for 120 minute, respectively. The results indicated that Liu isotherm model was fitted to the experimental data in a good agreement.

Radaei et al. (2014) [95] optimized the removal of Reactive Blue 19 onto activated carbon from pomegranate by using response surface methodology (RSM). The effects of initial pH (3-11), adsorbent dose (0.75-1.75 g/L), initial dye concentration (100-500 mg/L) and contact time (1-9 min) were examined during the adsorption experiments. Reactive Blue 19 removal was reported as 98.7 % at initial pH of 11, 1.025 g/L adsorbent dosage, 100 mg/L initial dye concentration and 6.8 min contact time.

Asgher and Bhatti (2012) [96] used lignocellulosic waste of *Citrus sinensis* as biosorbent to remove Reactive Blue 19 dye from aqueous solution. The optimum removal conditions of Reactive Blue 19 were investigated under various experimental terms such as dye concentration (50-300 mg/L), adsorbent amount (0.005-1.5 g), pH (1-6) and temperature (30-70 °C). The Langmuir and Temkin adsorption isotherm models described the adsorption of RB19 dye very well.

Ahmed et al. (2012) [97] used orange peel (OP) and modified orange peel, which include sodium hydroxide-treated orange peel (SOP), Cetyltrimethylammonium bromide modified orange peel (CTAB-modified OP) and Cetyltrimethylammonium bromide modified sodium hydroxide-treated orange peel (CTAB-modified SOP), as adsorbent for adsorption of anionic dyes like Reactive Blue 19. According to the experimental data, the effects of contact time, temperature and pH were found significant on the adsorption of Reactive Blue 19 dye. The Langmuir adsorption isotherm model described the adsorption of RB19 dye onto OP and SOP and, Temkin adsorption isotherm model described the adsorption of RB19 dye onto CTAB-modified OP and CTAB-modified SOP, very well.

The main findings of the studies mentioned above on the Reactive Blue 19 dye adsorption onto various adsorbents used at optimum experimental conditions were summarized in Table 7.3.

Table 7.3 Various studies on the adsorption of Reactive Blue 19 dye onto various adsorbents

References	Adsorbent	Optimum Conditions						Adsorption Isotherm Model	Adsorption Kinetic Model
		Adsorbent Amount (g/L)	Initial Dye Conc. (mg/L)	Time (min)	Temp. (°C)	pH	Removal (%)		
Xu et al. (2018) [83]	Chitosan-based magnetic adsorbent	5	100	-	30	2	90.00	Langmuir	Pseudo-second order
Mustafa et al. (2017) [84]	<i>Panus trignus</i>	15	50	90	-	2	83.18	Langmuir	Pseudo-second order
Demirhan (2017) [85]	Peanut shell	15	300	-	35	2	93.45	Langmuir	Pseudo-second order
Mousa and Taha (2016) [86]	Natural wheat straw	5	100	300	-	6.5	68.00	Freundlich	Pseudo-first order
	Modified wheat straw	5					92.17	Freundlich	Second order
	Activated carbon	5					90.50	Langmuir	Pseudo-second order
Ciobanu et al. (2016) [87]	Uncalcined HAP nanopowders	2	65	180	20	3	95.58	Langmuir	Pseudo-second order
	Calcined HAP nanopowders						86.95		
Bindary et al. (2015) [88]	Rice straw fly ash	3.6	100	60	25	1	85.00	Freundlich	Pseudo-second order

Table 7.3 Various studies on the adsorption of Reactive Blue 19 dye onto various adsorbents (cont'd)

References	Adsorbent	Optimum Conditions						Adsorption Isotherm Model	Adsorption Kinetic Model
		Adsorbent Amount (g/L)	Initial Dye Conc. (mg/L)	Time (min)	Temp. (°C)	pH	Removal (%)		
Balarak et al. (2015) [89]	<i>Lemna minor</i>	5	20	75	-	3	-	Langmuir	Pseudo-second order
Dehvari et al. (2015) [90]	Pomegranate seeds powder	1 - 5	100	60	25	3	-	Freundlich	Pseudo-second order
Khoshhesab and Ahmadi (2015) [91]	NiO nanoparticles	2.2	75	60	25	-	-	Sips model	Pseudo-second order
Ghaneian et al. (2014) [92]	Jujube stems powder	6	125	180	-	10	84	Langmuir	Pseudo-second order
Nguyen and Pho (2014) [93]	Chitosan coated magnetic hydroxyapatite nanoparticles	2	50	-	-	6	93	-	-
Rafiee and Jahangiri-rad (2014) [94]	multi-walled carbon nanotube (MWCNT)	0.6	20 - 200	120	50	3	-	Liu	-
	single-walled carbon nanotube (SWCNT)								

Table 7.3 Various studies on the adsorption of Reactive Blue 19 dye onto various adsorbents (cont'd)

References	Adsorbent	Optimum Conditions						Adsorption Isotherm Model	Adsorption Kinetic Model
		Adsorbent Amount (g/L)	Initial Dye Conc. (mg/L)	Time (min)	Temp. (°C)	pH	Removal (%)		
Radaei et al. (2014) [95]	Activated carbon	1.025	100	6.8	-	11	98.1	-	-
Asgher and Bhatti (2012) [96]	Lignocellulosic waste	0.05 - 1.5	50 - 300	-	30	2	-	Langmuir, Temkin	Pseudo-second order
Ahmed et al. (2012) [97]	Orange Peel (OP)	4	20 - 300	30	30	4	-	Langmuir	Pseudo-second order
	Sodium hydroxide-treated Orange Peel (SOP)			30			-	Langmuir	
	CTAB-modified OP			60			-	Temkin	
	CTAB-modified SOP			60			-	Temkin	

MATERIALS AND METHODS

8.1 Materials

8.1.1 Chemicals

Aluminium nitrate nonahydrate ($\text{Al}(\text{NO}_3)_3 \cdot 9\text{H}_2\text{O}$), iron (III) nitrate nonahydrate ($\text{Fe}(\text{NO}_3)_3 \cdot 9\text{H}_2\text{O}$) and sucrose ($\text{C}_{12}\text{H}_{22}\text{O}_{11}$) were purchased from Merck. Urea (98+%) (NH_2CONH_2) and Glycine (99 %) ($\text{NH}_2\text{CH}_2\text{CO}_2\text{H}$) were purchased from Alfa Aesar. Reactive Blue 19 dye was obtained from Gulecin Kimya A.S., Istanbul, Turkey.

8.1.2 Apparatus

- **Analytical Balance**

RADWAG AS 220.R2 analytical balance was used during the experiments. Its capacity is maximum 220 g with 0.1 mg readability.

- **Magnetic Stirrer**

DAIHAN MaXtir 500 S digital magnetic stirrer was used for mixing the solutions at various speed and temperature. The speed range of the digital magnetic stirrer is between 80 and 1500 rpm and its temperature range is adjustable from ambient temperature to 500 °C.

- **Centrifuge**

→ Nüve NF 615 was used to centrifuge the samples during the washing steps of the synthesis. Its speed range is between 2000 to 5000 rpm. It has hold six rotors with 15 mL capacity per one.

→ HETTICH MICRO 20 was used for centrifugation of dye solutions. It has 12 rotors with 2.2 mL capacity per one and its speed range was adjustable from 0 to 13000 rpm.

- **Vortex**

Isolab advanced vortex was used for rapid vortexing of the samples. Its variable speed range is between 0 and 3000 rpm.

- **Oven**

Memmert drying oven was used for drying of samples, and it can be operated from ambient temperature to 200 °C.

- **Furnace**

Protherm PLF 120/5 Furnace was used for calcination step of the samples. The maximum operating temperature of the furnace is 1200 °C. It has 2.0 kW power with ± 2 °C accuracy. Protherm Furnace used were presented in Figure 8.1.



Figure 8.1 Protherm Furnace

- **Tube Furnace**

Protherm Tube Furnace in Marmara University was used to reduce the samples in hydrogen atmosphere. The temperature was set as a function of time during Tube Furnace usage (Figure 8.2).



Figure 8.2 Protherm Tube Furnace

- **pH meter**

EUTECH alpha pH 800 pH/ORP Controller was used for pH adjustment of the solutions with an accuracy of 0.1.

- **Orbital shaker**

IKA KS 3000 control incubator orbital shaker was used to mix the dye solutions during adsorption experiments. Its speed rate is adjustable from 10 to 500 rpm, and its temperature range is between 5 and 80 °C.

8.2 Experimental Studies

8.2.1 Synthesis of Aluminium Oxide Nanoparticles

Aluminium oxide (alumina) nanoparticles were synthesized by using aluminium nitrate ($\text{Al}(\text{NO}_3)_3$) as an oxidizer, urea ($\text{CO}(\text{NH}_2)_2$) and glycine ($\text{C}_2\text{H}_5\text{NO}_2$) as a fuel by solution combustion method.

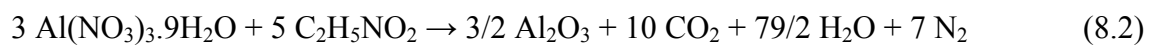
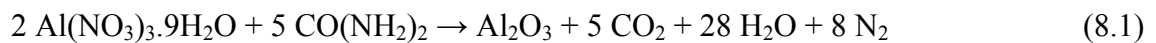
Firstly, precursor solutions were prepared for the synthesis of relevant nanoparticles. For this purpose, 15 g of $\text{Al}(\text{NO}_3)_3$ and 24 mL of distilled water were mixed until obtaining homogenous solution, thus 1.67 M (mole/L) precursor solution was prepared. Similarly, urea and glycine solutions containing 16.67 and 3.33 molar concentrate (mole/L), respectively, were prepared as fuel solution.

Secondly, 1.5 mL of 16.67 M (mole/L) urea solution was added to 11 mL of oxidizer ($\text{Al}(\text{NO}_3)_3$) solution, and then the solution was continuously stirred at 500 rpm with magnetic stirrer for preparing the sample coded SC-A-U1. Similarly, for the preparation of the samples coded SC-A-U2, SC-A-G1 and SC-A-G2, 3 mL of urea, 4.5 mL and 9 mL of glycine solutions were added to 11 mL of $\text{Al}(\text{NO}_3)_3$ solution, respectively. SC-A-U1 and SC-A-G1 samples were synthesized using 50 % of stoichiometric amount of fuel. On the other hand, SC-A-U2 and SC-A-G2 samples were synthesized using stoichiometric amount of fuel (100 %). The oxidizer, fuel types and stoichiometric fuel ratios for aluminium oxide nanoparticles synthesized by solution combustion method were given in Table 8.1.

Table 8.1 The oxidizer and fuel amounts and stoichiometric fuel ratios for aluminium oxide nanoparticles synthesized by solution combustion method

Sample Name	Oxidizer	Fuel Types		Stoichiometric Fuel Ratio (%)
	$\text{Al}(\text{NO}_3)_3$ solution (mL)	Urea solution (mL)	Glycine solution (mL)	
SC-A-U1	11	1.5	-	50
SC-A-U2	11	3	-	100
SC-A-G1	11	-	4.5	50
SC-A-G2	11	-	9	100

For preparation of each sample given in Table 8.1, the solution mixture containing specified amounts of oxidizer and fuel type were stirred at 500 rpm for 15 mins. at room temperature to obtain homogenous solutions on magnetic stirrer without any heating. Then, each mixed solution was heated up to 400 °C on a hot plate without any mixing until the solution become free from water to form final foam-like sample. The reactions [74] occurred between oxidizer and fuels (urea and glycine) were shown in Equations (8.1) and (8.2), respectively.



Before the calcination process, each final foam-like samples were grinded by using mortar and pestle, washed with distilled water for three times. During the washing step, distilled water was added to samples, then these mixtures were blended by vortex and centrifuged to remove impurities. After that, the samples were dried in oven at 100 °C for 1 hour. Finally, dried samples were calcined in a furnace at 1000 °C for 1 hour for phase transformation and removing the rest of the impurities as well. In Figure 8.3, the images of SC-A-U1, SC-A-U2, SC-A-G1 and SC-A-G2 before and after calcination steps were presented.

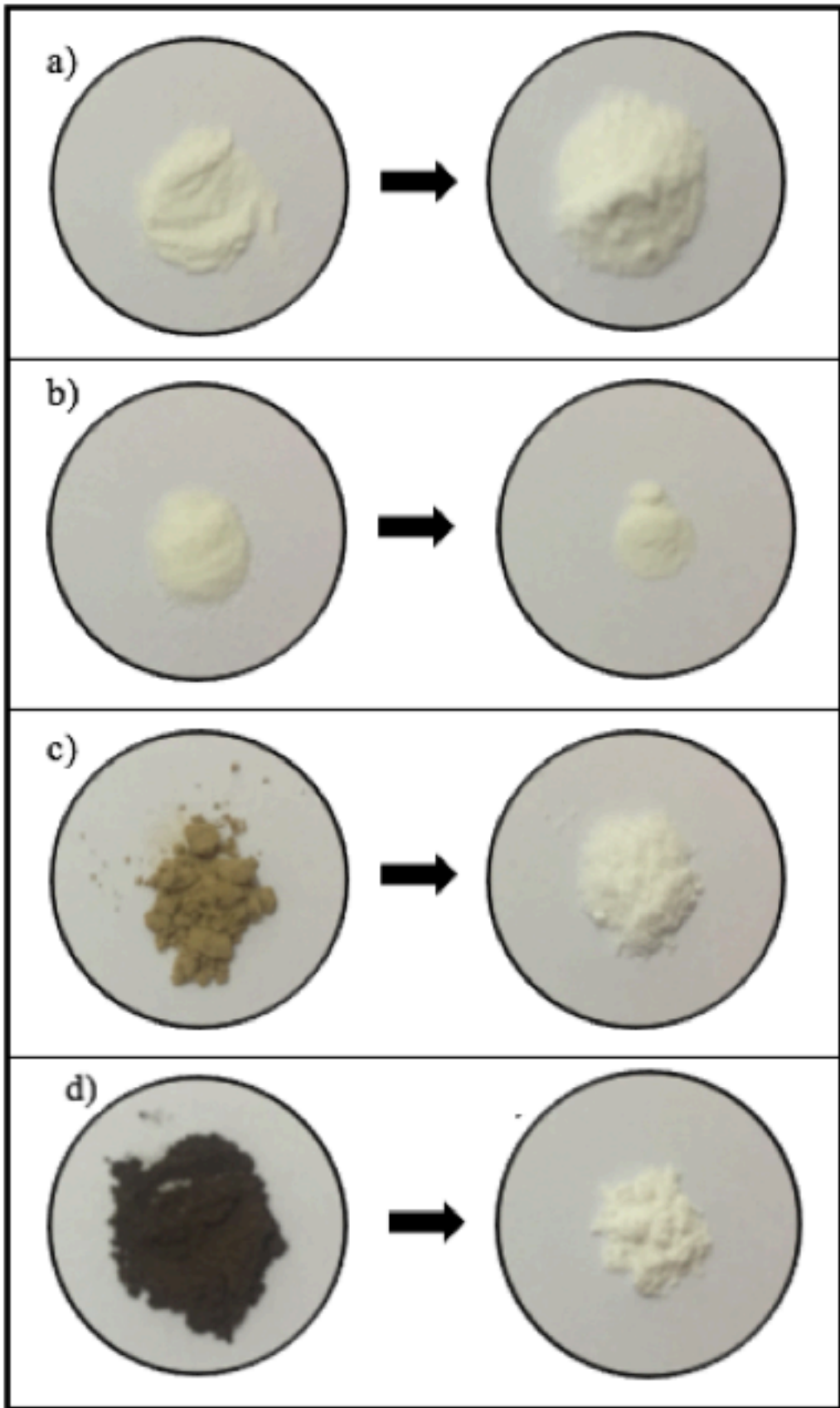


Figure 8.3 The images of synthesized samples before and after calcination
a) SC-A-U1, b) SC-A-U2, c) SC-A-G1 and d) SC-A-G2

8.2.2 Synthesis of Iron Based Magnetic Aluminium Oxide Nanocomposites

Magnetic aluminium oxide nanocomposites were prepared from two oxidizers, aluminium nitrate ($\text{Al}(\text{NO}_3)_3$) and iron nitrate ($\text{Fe}(\text{NO}_3)_3$), by using solution combustion synthesis. Besides, urea ($\text{CO}(\text{NH}_2)_2$), glycine ($\text{C}_2\text{H}_5\text{NO}_2$) and sucrose ($\text{C}_{12}\text{H}_{22}\text{O}_{11}$) were used as fuel.

Firstly, precursor solutions were prepared for the synthesis of relevant nanocomposites. For this purpose, the first oxidizer solution was prepared by adding 15 g of $\text{Al}(\text{NO}_3)_3$ to 24 mL of distilled water, and mixed until obtaining homogenous solution. Similarly, the second one was prepared by adding 15 g of $\text{Fe}(\text{NO}_3)_3$ to 24 mL of distilled water, and mixed until obtaining homogenous solution. On the other hand, 16.67 M urea, 3.33 M glycine and 2.92 M sucrose homogeneous solution were prepared to be used as fuel solution.

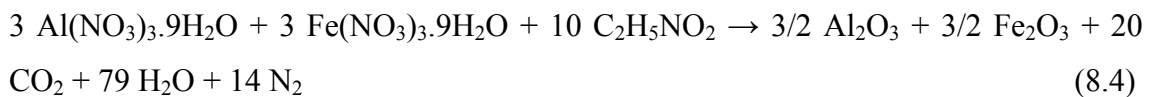
Secondly, 11 mL of $\text{Al}(\text{NO}_3)_3$ solution was mixed with 11 mL of $\text{Fe}(\text{NO}_3)_3$ solution and stirred at 500 rpm by using magnetic stirrer without any heating. Then, after adding 3 mL of 16.67 M urea solution, the final mixture was stirred for another 15 minutes without any heating for preparation of the sample coded SC-FA-U1. Similarly, 9 mL of glycine and 2.25 mL of sucrose solutions were added to precursor mixture ($\text{Al}(\text{NO}_3)_3$ and $\text{Fe}(\text{NO}_3)_3$) for preparation of the samples coded SC-FA-G1 and SC-FA-S1, respectively. Accordingly, 6 mL of urea, 18 mL of glycine and 4.5 mL of sucrose solution were added precursor solution and mixed continuously for the synthesis of SC-FA-U2, SC-FA-G2 and SC-FA-S2 samples, respectively. SC-FA-U1, SC-FA-G1 and SC-FA-S1 were synthesized using 50 % of stoichiometric amount of fuel. On the other hand, SC-FA-U2, SC-FA-G2 and SC-FA-S2 were synthesized using stoichiometric amount of fuel (100 %). The oxidizers, fuel types and stoichiometric fuel ratios for iron based magnetic aluminium oxide nanocomposites synthesized by solution combustion method were given in Table 8.2.

For preparation of each sample given in Table 8.2, the solution mixture containing specified amounts of oxidizers and fuels were stirred at 500 rpm for 15 mins at room temperature to obtain homogeneous solution on magnetic stirrer without any heating. Then, each mixed solution was heated up to 400 °C on a hot plate without any mixing until the solution become free from water to form final foam-like product.

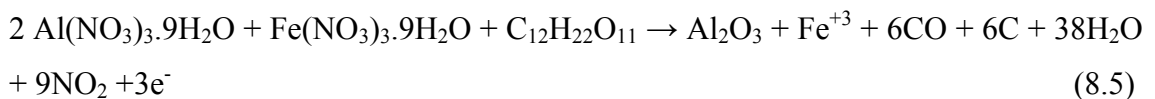
Table 8.2 The oxidizer and fuel amounts and stoichiometric fuel ratios for iron based magnetic aluminium oxide nanocomposites synthesized by solution combustion method

Sample Name	Oxidizer		Fuel Types			Stoichiometric Fuel Ratio (%)
	Al(NO ₃) ₃ solution (mL)	Fe(NO ₃) ₃ solution (mL)	Urea solution (mL)	Glycine solution (mL)	Sucrose solution (mL)	
SC-FA-U1	11	11	3	-	-	50
SC-FA-U2	11	11	6	-	-	100
SC-FA-G1	11	11	-	9	-	50
SC-FA-G2	11	11	-	18	-	100
SC-FA-S1	11	11	-	-	2.25	50
SC-FA-S2	11	11	-	-	4.5	100

Equations (8.3) and (8.4) were to describe the expected reactions occurred between oxidizers (Al(NO₃)₃ and Fe(NO₃)₃) and fuels (urea or glycine), respectively. These equations were given as follow;



The reaction [47] occurred between oxidizers (Al(NO₃)₃ and Fe(NO₃)₃) and sucrose was given in Equation (8.5).



Moreover, the general thermal dissociation equations of Al(NO₃)₃ [74] and Fe(NO₃)₃ [98] were given in Equations (8.6) and (8.7), respectively.



Before the calcination process, each final foam-like samples were grinded by using mortar and pestle, washed with distilled water for three times. During the washing step, distilled water was added to samples, then these mixtures were blended by vortex and centrifuged to remove impurities. After that, the samples were dried in oven at 100 °C for 1 hour. The samples obtained after drying process were coded SC-FA-U1, SC-FA-U2, SC-FA-G1, SC-FA-G2, SC-FA-S1 and SC-FA-S2. Among the synthesized samples, according to their XRD analysis, SC-FA-U2, SC-FA-G2 and SC-FA-S2 were chosen further for calcination and reduction process.

For the calcination process, the samples were calcined in a furnace at 1000 °C for 1 hour for removing the rest of impurities. In addition to this calcination step, the samples were reduced at 1000 °C in tube furnace under hydrogen atmosphere for 1 hour. Then, these samples (SC-FA-U2, SC-FA-G2 and SC-FA-S2 after calcination and reduction process) were coded as SC-FA-U2-H, SC-FA-G2-H and SC-FA-S2-H. The nominations of the synthesized samples were presented in Table 8.3.

Table 8.3 Specifications of the synthesized samples

Sample Name	Specifications of synthesized samples
SC-FA-U1	synthesized by 50 % of stoichiometric amount of urea as a fuel
SC-FA-U2	synthesized by stoichiometric amount of urea as a fuel (100 %)
SC-FA-U2-H	synthesized by stoichiometric amount of urea as a fuel (100 %), calcined and then reduced under hydrogen atmosphere
SC-FA-G1	synthesized by 50 % of stoichiometric amount of glycine as a fuel
SC-FA-G2	synthesized by stoichiometric amount of glycine as a fuel (100 %)
SC-FA-G2-H	synthesized by stoichiometric amount of glycine as a fuel (100 %), calcined and then reduced under hydrogen atmosphere
SC-FA-S1	synthesized by 50 % of stoichiometric amount of sucrose as a fuel
SC-FA-S2	synthesized by stoichiometric amount of sucrose as a fuel (100 %)
SC-FA-S2-H	synthesized by stoichiometric amount of sucrose as a fuel (100 %), calcined and then reduced under hydrogen atmosphere

Magnetic attractions of synthesized samples were observed by using commercially available neodymium (NdFeB) magnet. The image of magnetic attraction of synthesized SC-FA-G2 sample with neodymium magnet was shown in Figure 8.4. For all synthesized nanocomposites were checked for their magnetic attraction (Table 8.4).



Figure 8.4 Magnetic attraction of SC-FA-G2

Table 8.4 Magnetic attraction of the synthesized samples

Sample Name	Magnetic attraction
SC-FA-U1	No attraction
SC-FA-U2	Attracted
SC-FA-U2-H	Attracted
SC-FA-G1	Attracted (Low)
SC-FA-G2	Attracted
SC-FA-G2-H	Attracted
SC-FA-S1	No attraction
SC-FA-S2	Attracted (Low)
SC-FA-S2-H	Attracted

8.2.3 Adsorption Studies

SC-FA-G2 synthesized using glycine as fuel by solution combustion method was chosen for further adsorption studies according to the results obtained from XRD and SEM analysis and as well as its magnetic attraction property. In this part of the study, Reactive Blue 19 (RB19) dye was chosen for investigation of the adsorption capacity onto SC-FA-G2 from aqueous solutions at various process conditions. For this purpose, an experimental set was planned using Design Expert 11.0, experimental design programme, according to the Response Surface Methodology (RSM). According to Box-Behnken Design, 17 experiments were performed under various process conditions. The effects of pH, temperature and adsorbent amount of SC-FA-G2 were investigated on the adsorption process.

At the preliminary step of the experiments, RB19 dye stock solution was prepared with distilled water at a concentration of 100 mg/L. For each individual experiment, 50 mL of this solution was placed in a 100 mL Erlenmeyer flask. According to the experimental design, each experiment was performed under defined conditions. The initial pH of the dye solution was adjusted with 10 M HCl or 0.1 M NaOH solution. The flasks were placed in an orbital shaker at 100 rpm for 60 minute. The effects of the pH (2, 4 and 6), adsorbent amount (4, 8 and 12 g/L) and temperature (25, 35 and 45 °C) on the dye adsorption were investigated. During the experiments, the samples were taken from the flasks at specified time intervals and centrifuged to remove adsorbent at 12000 rpm for 4 min. After centrifuging, the optical densities of the samples were measured by using UV-vis spectrophotometer at 592 nm wavelength to determine the remaining RB19 dye concentration.

The dye adsorption capacity (q_e , mg/g) and removal rate (R %) were calculated by following equations:

$$q_e = \frac{c_0 - c_e}{m} \cdot V \quad (8.8)$$

$$R \% = \frac{c_0 - c_e}{c_0} \cdot V \quad (8.9)$$

Where; C_0 and C_e (mg/L) are the initial and equilibrium dye concentration, respectively. V (L) is the volume of the dye solution, and m (g) is the amount of the adsorbent.

After the adsorption processes, SC-FA-G2 sample (iron based magnetic aluminium oxide nanocomposite) was checked again its magnetic attraction property, and it was found that it still preserves its magnetic attraction property (Figure 8.5).

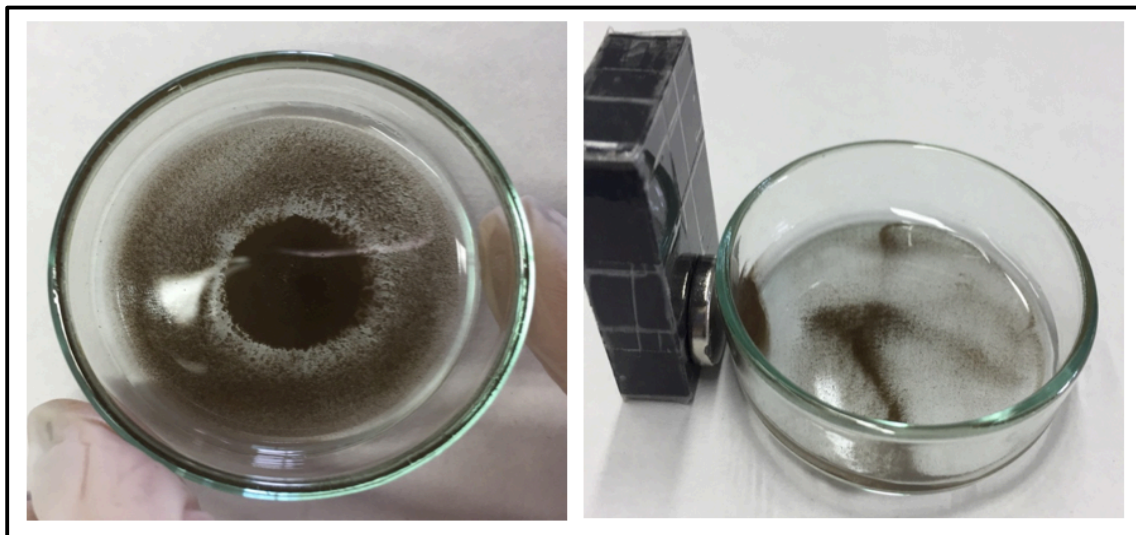


Figure 8.5 Magnetic attraction of SC-FA-G2 after adsorption process with commercial magnet

8.3 Characterization Studies

The characterization studies were carried out by X-Ray Diffraction (XRD), Scanning Electron Microscope (SEM), Thermogravimetric/Differential Thermal Analysis (TG/DTA), BET surface area and UV-Vis analysis.

- XRD analysis were used to evaluation of the chemical and phase compositions of synthesized aluminium oxide and iron based magnetic aluminium oxide samples.
- SEM images were used to analysis the particles sizes, surface features and morphologies of the synthesized samples.
- TG/DTA was used to observe the thermal decomposition and phase transformation of samples.
- BET surface area and porosity analyser was used to examine the surface area, pore volume and average pore diameter.
- UV-Vis spectrophotometer was used for the determination of the remaining dye concentration during the adsorption experiments.

8.3.1 X-Ray Diffraction Analysis

PANalytical X'Pert Pro analyser was used to obtain X-Ray diffraction patterns of the synthesized aluminium oxide powders and iron based magnetic aluminium oxide nanocomposites (Figure 8.6). XRD analyser was equipped with Cu-K α radiation source. XRD diffraction patterns were obtained with scanning angle 2θ ranged between 10° and 90° with $1^\circ/\text{min}$ scanning rate at 45 kV and 40 mA.



Figure 8.6 Equipment for X-ray Diffraction Analysis

8.3.2 Scanning Electron Microscope

The following Scanning Electron Microscope devices were used;

- Zeiss EVO LS10 operating in beam mode at 20 kV with secondary electron detector was used to characterization of the samples (Figure 8.7).
- JEOL JSM 6335F Scanning Electron Microscope with Oxford Instruments XMaxN 80 the energy dispersive X-ray spectroscopy (SEM-EDS) in TUBITAK Marmara Research Centre was used for characterization of the samples (Figure 8.8).



Figure 8.7 Scanning Electron Microscope (SEM)



Figure 8.8 Scanning Electron Microscopy-Energy Dispersive X-ray Spectroscopy (SEM-EDS)

8.3.3 Thermogravimetric/Differential Thermal Analysis

EXSTAR SII TG/DTA6300 instrument was used for thermogravimetric and differential thermal analysis (TG/DTA) of the samples (Figure 8.9). It can be operated from ambient temperature to 1500°C. The TG measurement range is 200 mg with $\pm 0.2 \mu\text{g}$ accuracy. It works in air or inert atmosphere. The measurements were carried out from room temperature to 1200 °C with a heating rate of 20°C/min under air atmosphere.



Figure 8.9 Thermogravimetric/Differential Thermal Analyzer (TG/DTA)

8.3.4 Surface Area and Porosity Analysis

Quadasorb SI surface area and pore size analyser was used for the characterization of the synthesized samples. Nitrogen or any other non-corrosive gas was used as adsorbate for BET analysis. Figure 8.10 indicates the Quadeasorb SI surface area and pore size analyser.



Figure 8.10 BET Surface Area and Porosity Analyser

8.3.5 UV-Vis Spectrophotometer

UV-1800 spectrophotometer produced by SHIMADZU was used to determine the absorbance value of the samples in the range of 190-1100 nm (Figure 8.11). The centrifuged samples were diluted with distilled water at a defined ratio, and disposable polystyrene cuvettes were used during the spectrophotometric measurements.

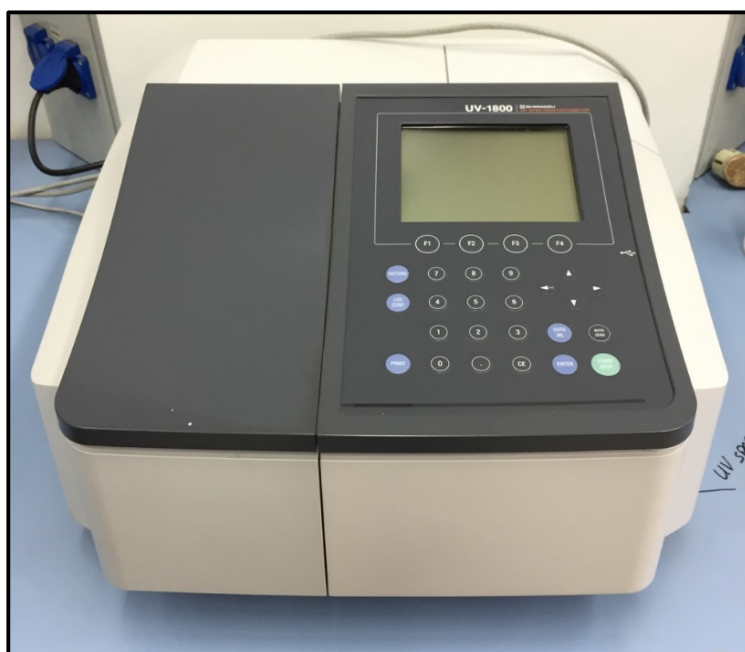


Figure 8.11 UV-Vis Spectrophotometer

8.4 Calibration Data for Reactive Blue 19 Dye

The calibration curve of Reactive Blue 19 was determined at various dye concentrations. The absorbance values of RB19 dye solutions were measured using UV-Vis spectrophotometer at 592 nm wavelength (Table 8.5). The measurements were repeated three times and the averages of the obtained data were taken. Linear regression analysis was made to obtain Equation (8.10), and this equation was used to calculate the dye concentration values. The regression coefficient (R^2) and standard deviation (σ) were found as 0.9996 and 0.6107, respectively. The data between the dye concentration values versus absorbance values were presented in Figure 8.12.

$$\text{Dye concentration } \left(\frac{\text{mg}}{\text{L}}\right) = 73.49 \times (\text{Adsorbance value}) \quad (8.10)$$

Table 8.5 Reactive Blue 19 dye calibration curve data

Dye Concentration (mg/L)	Average Absorbance Values
0.00	0.000
4.16	0.063
8.33	0.129
12.50	0.178
16.67	0.239
20.83	0.299
25.00	0.356
29.17	0.413
33.33	0.467
50.00	0.690
66.67	0.909
83.33	1.127
100.00	1.338

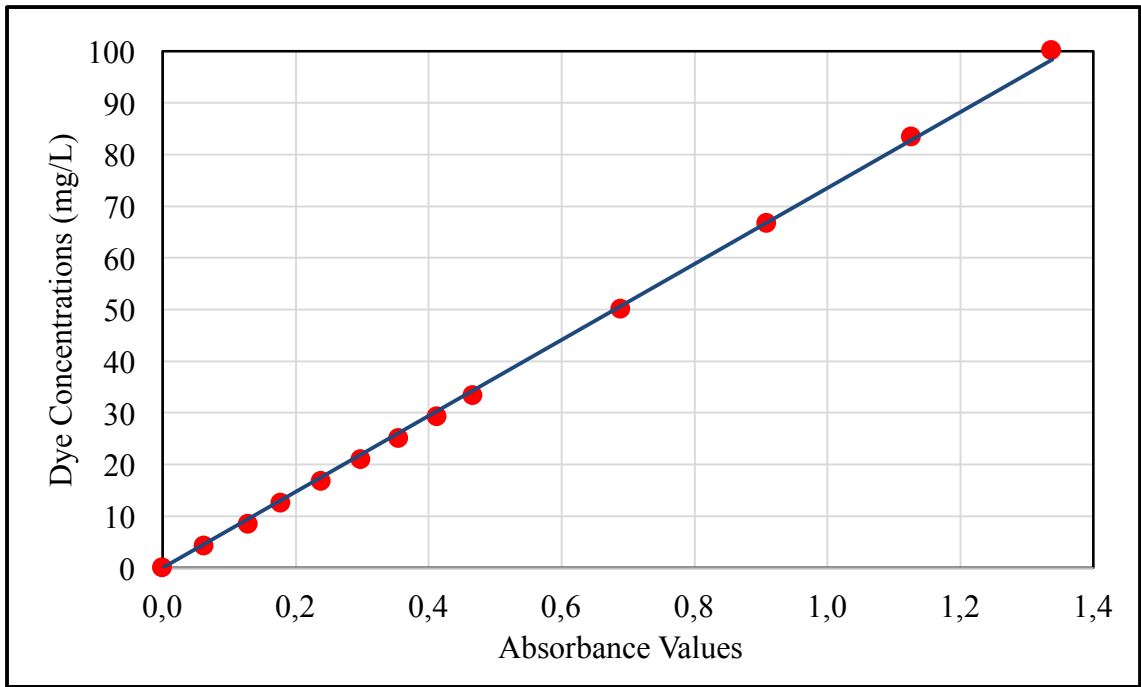


Figure 8.12 Calibration data of Reactive Blue 19 Dye

RESULTS AND DISCUSSION

In the present study, aluminium oxide and iron based magnetic aluminium oxide were synthesized by solution combustion method using various fuel types and amounts. Then, the synthesized samples were characterized for their physical and chemical properties. After characterization of the samples produced, the results suggested that the sample SC-FA-G2 fulfils the requirements among the synthesized samples. Among the synthesized samples, according to data obtained from the characterization studies, SC-FA-G2 sample was chosen as an adsorbent for further studies on Reactive Blue 19 dye adsorption from aqueous solutions.

The statistical method of Response Surface Methodology (RSM) was used for the modelling and optimization of the adsorption process parameters. The detailed evaluation of the characterization studies and the adsorption process for the synthesized samples were given in the following sections.

9.1 Characterization Studies of Synthesized Aluminium Oxide Nanoparticles

Aluminium oxide samples were synthesized by solution combustion method, using two fuel types (urea and glycine) at two fuel amounts, (stoichiometrically 50 % and 100 %) for each types of fuel. The effects of the fuel types and fuel amounts on the chemical and physical properties of synthesized particles were investigated and characterized using XRD, SEM and TG/DTA.

- XRD analyses of the samples were carried out for determining their chemical compositions and identification of phases formed.
- The surface structures and morphologies of the samples were analysed with SEM micrographs.

- The thermal behaviours of the samples before calcination were analysed by TG/DTA.

9.1.1 X-ray Diffraction Analysis

The X-ray diffraction patterns of the synthesized samples of SC-A-U1, SC-A-U2, SC-A-G1 and SC-A-G2 were shown in Figure 9.1a-d, respectively.

The X-ray diffraction peaks of SC-A-U1, synthesized by solution combustion method, using 50 % of stoichiometric amount of urea as a fuel were presented in Figure 9.1a. The diffraction peaks were displayed at 2θ values of 25.86° , 35.42° , 38.04° , 43.61° , 52.80° , 57.74° , 60.05° , 61.49° , 66.75° , 68.45° and 77.11° . XRD analysis suggested that the sample produced is an alpha phase aluminium oxide ($\alpha\text{-Al}_2\text{O}_3$) (96-100-0033 entry number).

The X-ray diffraction peaks of SC-A-U2, synthesized by solution combustion method, using stoichiometric amount of urea as a fuel (100 %) were presented in Figure 9.1b. According to the X-ray analysis of SC-A-U1 and SC-A-U2 samples, they have similar X-ray patterns (Figure 9.1a and b). The diffraction peaks were displayed at 2θ values of 25.59° , 35.16° , 37.79° , 43.36° , 46.17° , 52.56° , 57.49° , 59.75° , 61.26° , 66.48° , 68.20° and 77.12° . XRD analysis suggested that the sample produced is an alpha phase aluminium oxide ($\alpha\text{-Al}_2\text{O}_3$) (96-100-0033 entry number).

The X-ray diffraction peaks of SC-A-G1, synthesized by solution combustion method, using 50 % of stoichiometric amount of glycine as a fuel were presented in Figure 9.1c. These peaks were related with the amorphous phase aluminium oxide. XRD analysis suggested that the sample produced is a theta phase aluminium oxide ($\theta\text{-Al}_2\text{O}_3$) (96-120-0006 entry number).

The X-ray diffraction peaks of SC-A-G2, synthesized by solution combustion method, using stoichiometric amount of glycine as a fuel (100 %) were presented in Figure 9.1d. The diffraction peaks were displayed at 2θ values of 39.51° , 45.93° and 67.07° which indicated that 96-101-0462 entry number of gamma phase aluminium oxide ($\gamma\text{-Al}_2\text{O}_3$).

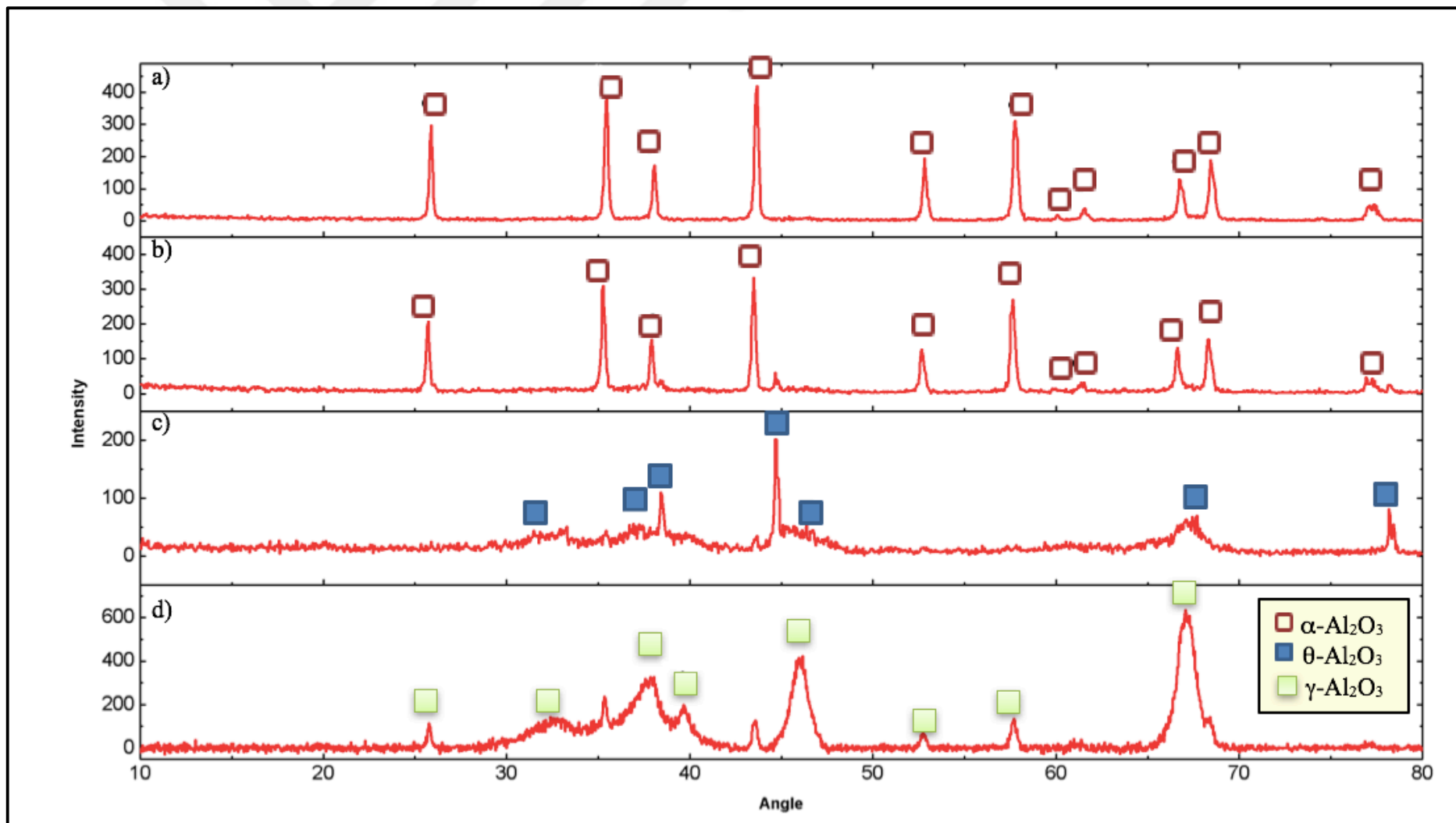


Figure 9.1 XRD patterns of synthesized samples of a) SC-A-U1, b) SC-A-U2, c) SC-A-G1 and d) SC-A-G2

9.1.2 Scanning Electron Microscopy Analysis

SEM analysis were taken for the morphological evaluation of the samples synthesized by solution combustion method.

The SEM images of SC-A-U1, synthesized by solution combustion method, using 50 % of stoichiometric amount of urea as a fuel with calcination were shown in Figure 9.2. From SEM images of SC-A-U1, sample was agglomerated and its particle size distribution was obtained in the range of 151.3 to 735 nm.

The SEM images of SC-A-U2, synthesized by solution combustion method, using stoichiometric amount of urea as a fuel (100 %) with calcination were shown in Figure 9.3. From SEM images, particle size of SC-A-U2 was found smaller than the particle size of SC-A-U1 synthesized using 50 % of stoichiometric amount of urea. Moreover, SC-A-U2 was less agglomerated compared to SC-A-U1 (Figure 9.3).

The SEM images of SC-A-G1, synthesized by solution combustion method, using 50 % of stoichiometric amount of glycine as a fuel with calcination were given in Figure 9.4. From SEM images of SC-A-G1, it was observed that using glycine solution as a fuel during synthesis caused the formation of porous structure. This case can be explained by the formation of gases during solution combustion synthesis reaction. Moreover, XRD analysis suggested that the presence amorphous structure (Figure 9.1).

The SEM images of SC-A-G2, synthesized by solution combustion method, using stoichiometric amount of glycine as a fuel (100 %) with calcination were given in Figure 9.5. From SEM images of SC-A-G2, it was observed that using glycine solution as a fuel during synthesis caused the formation of more porous structure. The formation of more porous structure can be associated with using glycine as a fuel may cause more vigorous solution combustion reaction than the reaction using urea as a fuel. Additionally, SC-A-G2 has smaller particle sizes in the range of 143.4 to 303 nm (Figure 9.5).

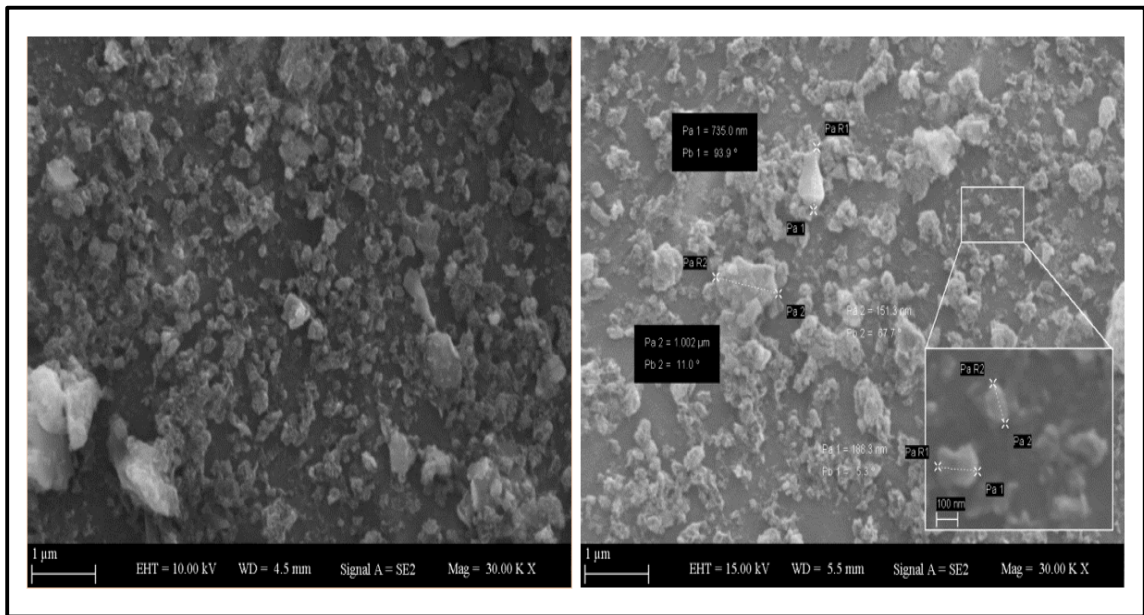


Figure 9.2 SEM microscopy images of SC-A-U1

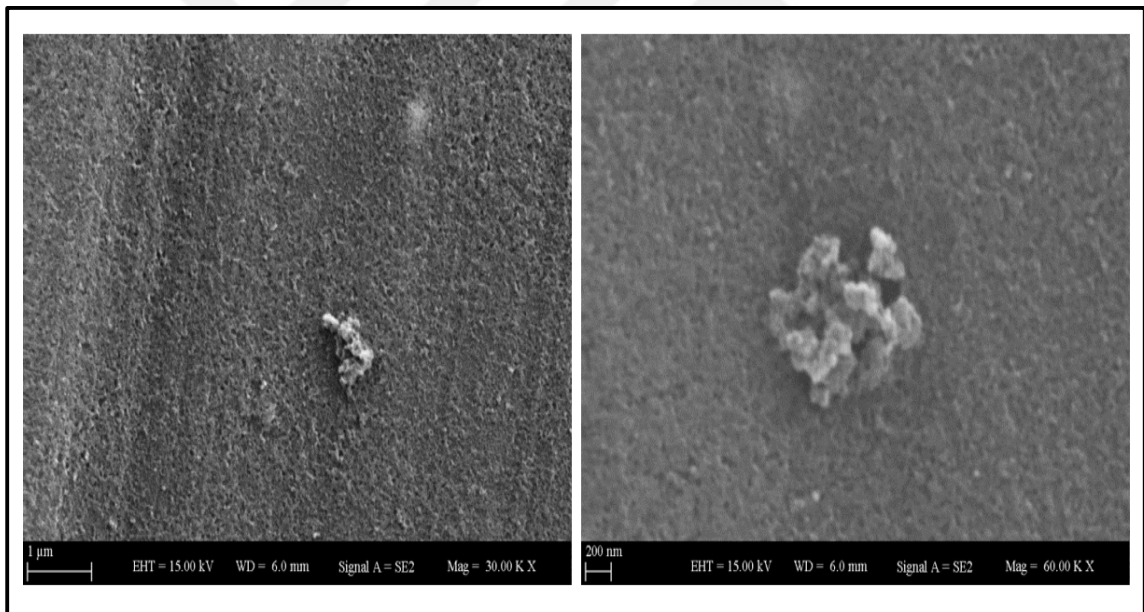


Figure 9.3 SEM microscopy images of SC-A-U2

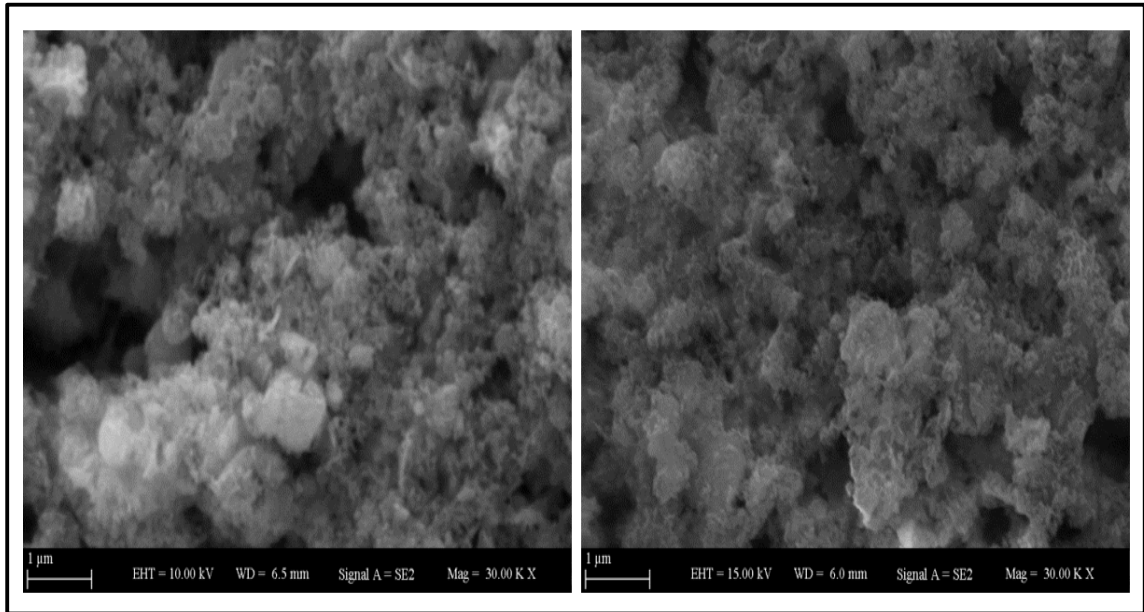


Figure 9.4 SEM microscopy images of SC-A-G1

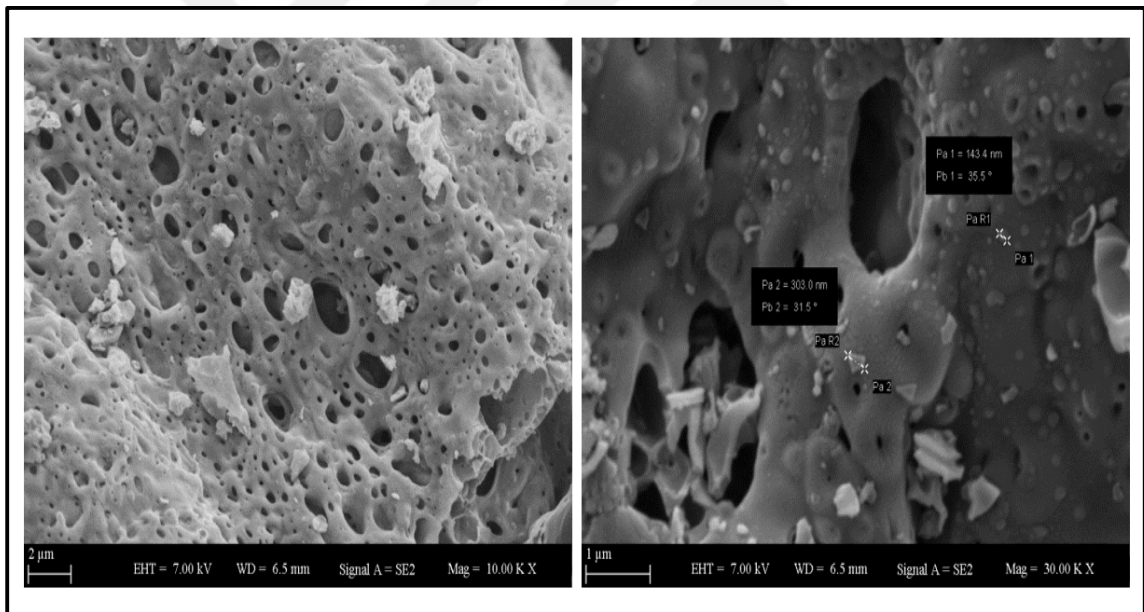


Figure 9.5 SEM microscopy images of SC-A-G2

9.1.3 Thermogravimetric/Differential Thermal Analysis

Thermogravimetric and differential thermal analysis (TG/DTA) were performed with the synthesized samples without calcination. The analyses were performed from ambient temperature to 1200 °C in air atmosphere.

TG/DTA analysis of SC-A-U1 synthesized by solution combustion method using 50 % of stoichiometric amount of urea as a fuel was shown in Figure 9.6. According to TG and DTG curves, SC-A-U1 showed rapid mass loss approximately 33 % from 25 to 280 °C, corresponding to the evaporation of the adsorbed water. DTA curve showed an endothermic peak at about 280 °C, corresponding to the evaporation of the constitution water in the aluminium hydroxide and AlOOH as stated by Huang et al. (2007) [99]. Additionally, between 280 and 500 °C, a mass loss observed approximately 18.9 %. This can be related with the conversion of boehmite into γ -Al₂O₃ as stated by Lucio-Ortiz et al. (2011) [100] in their study. According to DTA curve, some extra endothermic effects were observed at the temperatures between 890 and 1115 °C. This may be attributed to the transformation of γ -Al₂O₃ to α -Al₂O₃ as stated by Rogoan et al. (2011) [101] in their study.

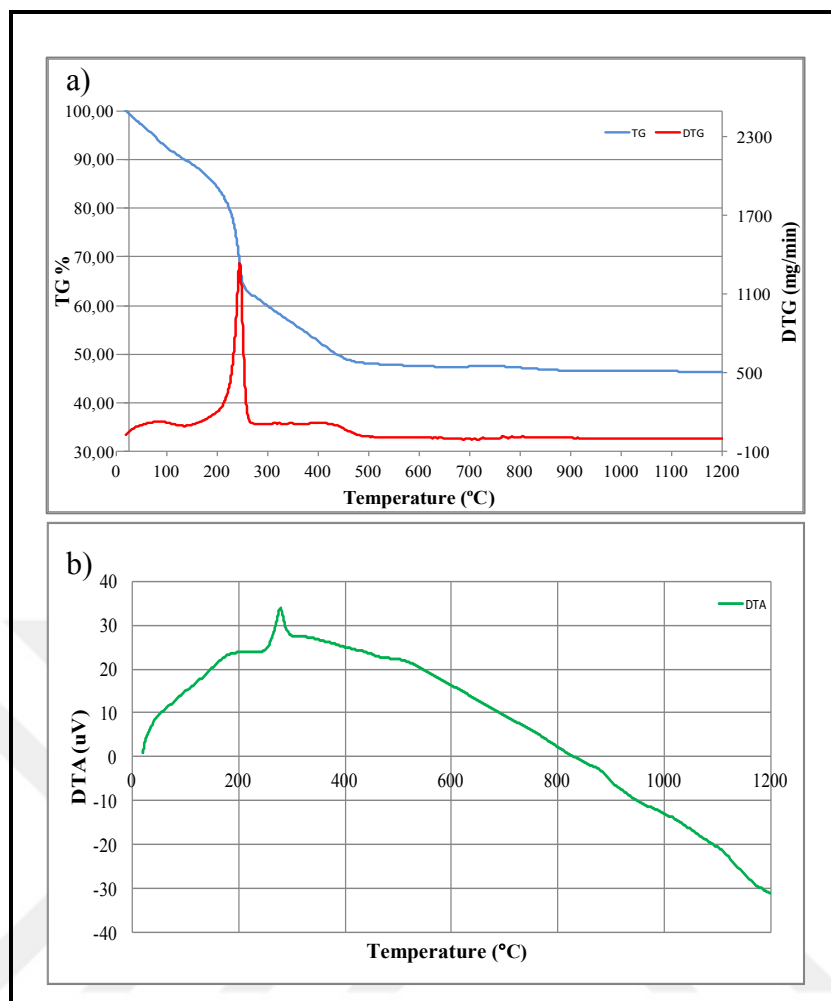


Figure 9.6 a) TG/DTG and b) DTA curves of SC-A-U1

TG/DTA analysis of SC-A-U2, synthesized by solution combustion method, using stoichiometric amount of glycine as a fuel (100 %) were shown in Figure 9.7. According to TG and DTG curves, the significant mass loss was detected in two regions. In the first region, 10 % of mass loss was occurred at the temperatures between 25 and 200 °C, this can be attributed to absorbed water in SC-A-U2. In the second region, the greater mass loss (53 %) was observed at the temperatures from 200 to 325 °C. This can be associated with removal of residues and water. In addition, 6.7 % mass loss was observed between 325 and 500 °C, which corresponds to conversion of boehmite into γ -Al₂O₃ as stated by Lucio-Ortiz et al. (2011) [100] in their study and this transition state were represented in Equation (9.1).



The extra endothermic reaction was appeared in between 970 and 1120 °C. This may be attributed to the transformation of γ -Al₂O₃ to α -Al₂O₃ as stated by Rogojan et al. (2011) [101] in their study.

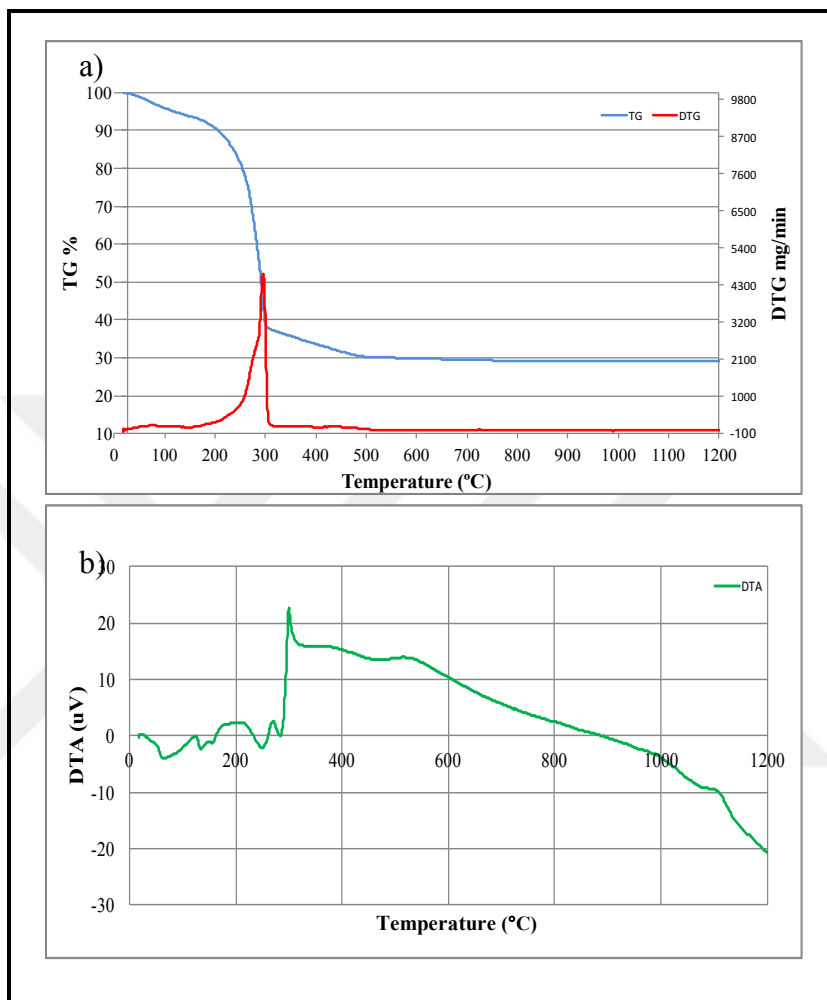


Figure 9.7 a) TG/DTG and b) DTA curves of SC-A-U2

TG/DTA analysis of SC-A-G1, synthesized by solution combustion method, using 50 % of stoichiometric amount of glycine as a fuel was shown in Figure 9.8. According to TG and DTG curves, total mass loss of SC-A-G1 was 27.2 %. The endothermic effect at 130 °C, corresponding to the evaporation of the adsorbed water. From DTA curve, the endothermic peak at about 450 °C, corresponding to the evaporation of constitution water in aluminium hydroxide and AlOOH. According to DTA curve, the peak was observed at approximately 1141 °C. This may be attributed to the transformation of polymorphous θ -Al₂O₃ to α -Al₂O₃ as stated by Huang et al. (2007) [99].

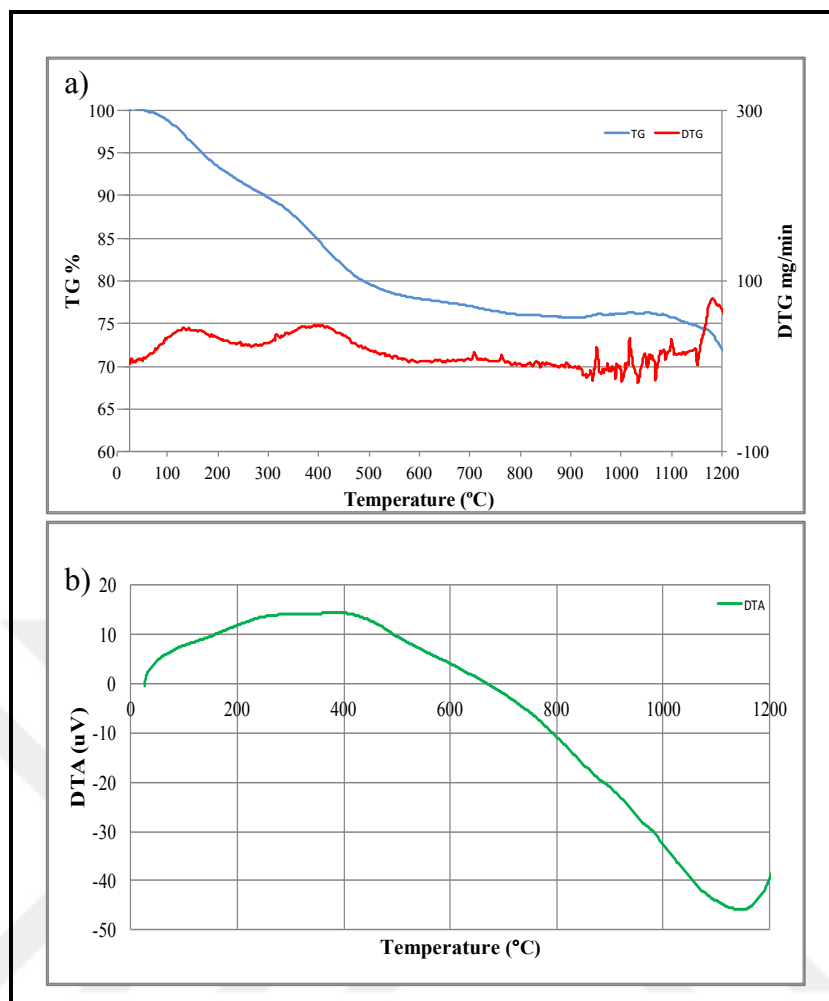


Figure 9.8 a) TG/DTG and b) DTA curves of SC-A-G1

TG/DTA analysis of SC-A-G2, synthesized by solution combustion method, using stoichiometric amount of glycine a fuel (100 %) was shown in Figure 9.9. According to TG and DTG curves, SC-A-G2 showed that it lost great part of its mass about 42 % from ambient temperature to 600 °C. This can be related with the dehydration of water and decomposition of organic components as stated by Lucio-Ortiz et al. (2011) [100] in their study. As shown in Figure 8.3d, before calcination sample of SC-A-G2 contains some amount of carbon residue. The total mass loss of SC-A-G2 was about 45 % from ambient temperature to 1200 °C. The endothermic peaks appeared at approximately 1150 °C may be associated with the conversion of $\gamma\text{-Al}_2\text{O}_3$ to $\alpha\text{-Al}_2\text{O}_3$ as similar results found by Huang et al. (2007) [99].

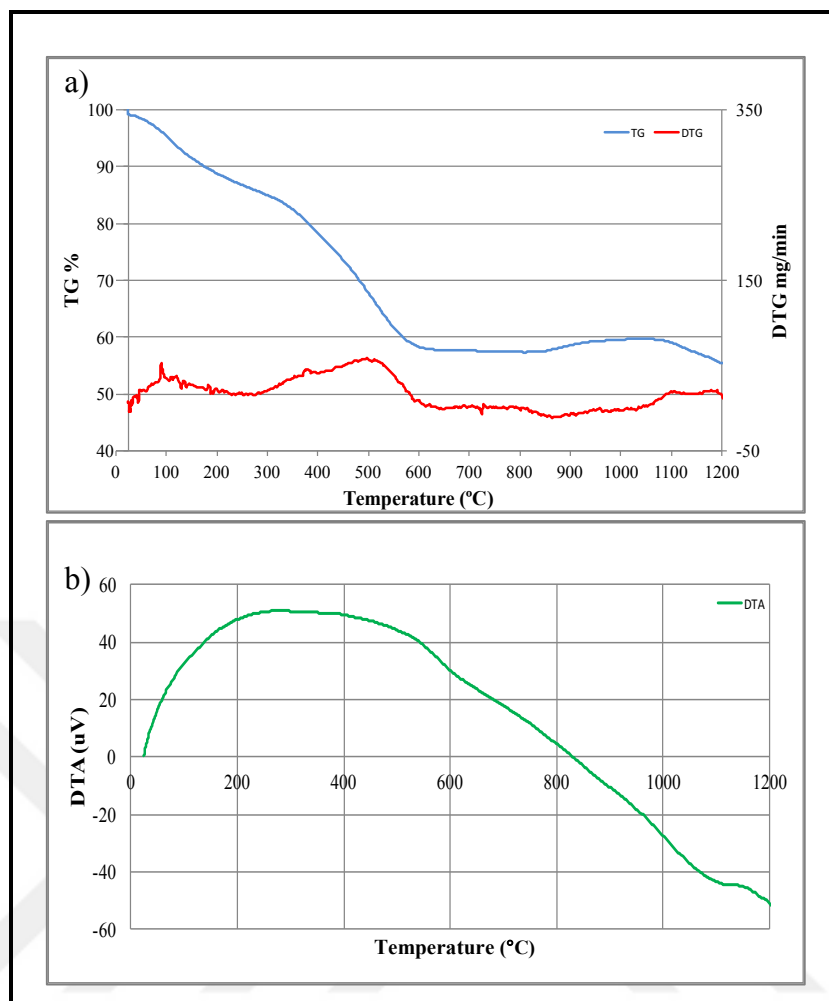


Figure 9.9 a) TG/DTG and b) DTA curves of SC-A-G2

9.2 Characterization Studies of Iron Based Magnetic Aluminium Oxide Nanocomposites

The iron based magnetic aluminium oxide nanocomposites were synthesized by solution combustion method, using three fuel types (urea, glycine and sucrose) with two fuel amounts (stoichiometrically 50 and 100 %) for each types of fuel. The chemical and physical properties of synthesized composites were characterized using XRD, SEM-EDS, TG/DTA and BET surface area and porosity analysers.

- XRD analyses of the samples were carried out for determining their chemical compositions and identification of phases formed.
- The surface structures, morphologies and compositional analysis of the samples were analysed with SEM-EDS micrographs.

- The thermal behaviours of the samples before calcination were analysed by TG/DTA.
- The surface area, pore volume and average pore diameter were examined by BET surface area and porosity analyser.

9.2.1 X-ray Diffraction Analysis

The X-ray diffraction peaks of SC-FA-U1, SC-FA-U2 and SC-FA-U2-H samples were shown in Figure 9.10a-c, respectively.

XRD analysis of SC-FA-U1, synthesized by solution combustion method, using 50 % of stoichiometric amount of urea as a fuel, and it was identified that very low crystallization was developed (Figure 9.10a).

The X-ray diffraction peaks of SC-FA-U2, synthesized by solution combustion method, using stoichiometric amount of urea as a fuel (100 %) were presented in Figure 9.10b. XRD analysis suggested of the sample produced is Fe₃O₄ (magnetite) (96-900-2328 entry number) and Al₂O₃ (96-152-8428 entry number). The data obtained from XRD analysis showed that the composition of SC-FA-U2 sample was 43.4 % Al₂O₃ and 56.6 % Fe₃O₄.

The X-ray diffraction peaks of SC-FA-U2-H, synthesized by solution combustion method, using stoichiometric amount of urea as a fuel (100 %) then calcined in a furnace and reduced under hydrogen atmosphere, was presented in Figure 9.10c. The diffraction peaks were displayed at 2θ values of 25.52°, 35.09°, 37.68°, 43.27°, 52.57°, 57.47°, 66.46°, 68.16° and 76.85°. XRD analysis suggested that the sample produced is α-Al₂O₃ (96-900-7497 entry number). Moreover, the diffraction peaks were displayed at 2θ values of 44.61°, 64.93° and 82.25° and XRD analysis suggested that the sample produced is iron (Fe) (96-901-3473 entry number). The data obtained from XRD analysis showed the composition of SC-FA-U2-H sample was 48.1 % α-Al₂O₃ and 51.9 % Fe.

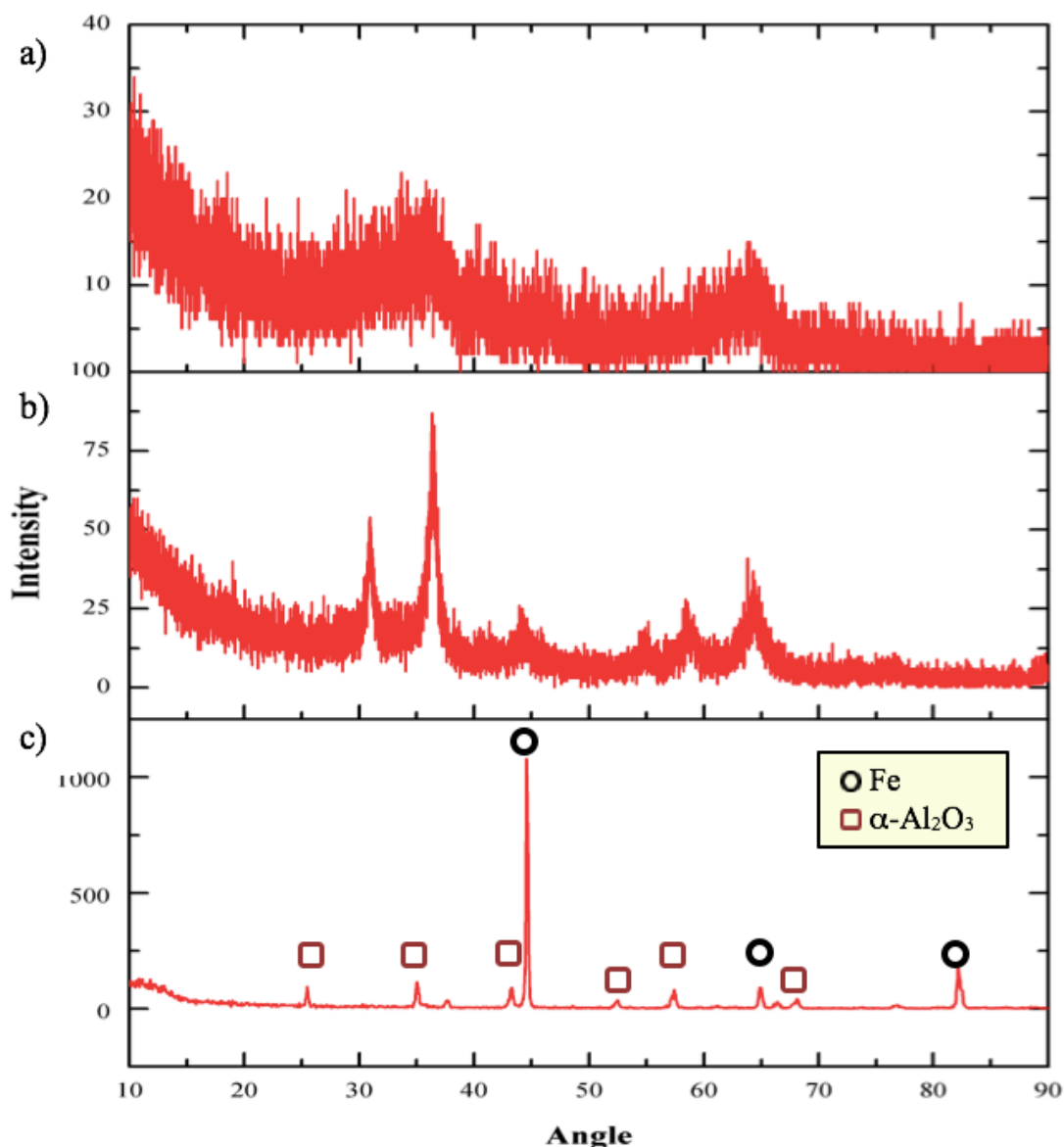


Figure 9.10 XRD patterns of synthesized samples of a) SC-FA-U1, b) SC-FA-U2 and c) SC-FA-U2-H

The X-ray diffraction peaks of SC-FA-G1, SC-FA-G2 and SC-FA-G2-H were shown in Figure 9.11a-c, respectively.

The X-ray diffraction peaks of synthesized SC-FA-G1 by solution combustion method using 50 % of stoichiometric amount of glycine as a fuel were presented in Figure 9.11a. X-ray analysis suggested that the sample produced is Fe_3O_4 (magnetite) (96-900-2327 entry number) and $\theta\text{-Al}_2\text{O}_3$ (96-120-0006 entry number). The data obtained from XRD analysis showed that the composition of SC-FA-G1 sample was 38.7 % $\theta\text{-Al}_2\text{O}_3$ and 61.3 % Fe_3O_4 .

The X-ray diffraction peaks of synthesized SC-FA-G2 sample by solution combustion method using stoichiometric amount of glycine as a fuel (100 %) were presented in Figure 9.11b. XRD analysis suggested that the sample produced is Fe_3O_4 (magnetite) (96-900-2331 number number) and Al_2O_3 (96-810-3515 number number). The data obtained from XRD analysis showed that the composition of SC-FA-G2 sample was 51 % Al_2O_3 and 49 % Fe_3O_4 . From X-ray patterns of synthesized samples, SC-FA-G1 crystallinity was less than SC-FA-G2 (Figure 9.11a and b).

The X-ray diffraction of SC-FA-G2-H, synthesized by solution combustion method, using stoichiometric amount of glycine (100 %) as a fuel, then calcined in a furnace and reduced under hydrogen atmosphere, was presented in Figure 9.11c. The diffraction peaks were displayed at 2θ values of 25.60° , 35.09° , 37.79° , 43.34° , 52.58° , 57.48° , 66.52° and 66.22° . From these peaks, XRD analysis suggested that the sample produced is $\alpha\text{-Al}_2\text{O}_3$ (96-900-7497 entry number). Moreover, the diffraction peaks at 2θ values of 44.63° , 64.90° and 82.19° . From these peaks, XRD analysis suggested that the sample produced is iron (Fe) (96-901-3473 entry number). The data obtained from XRD analysis showed that the composition of SC-FA-G2-H sample was 64.1 % $\alpha\text{-Al}_2\text{O}_3$ and 35.9 % Fe.

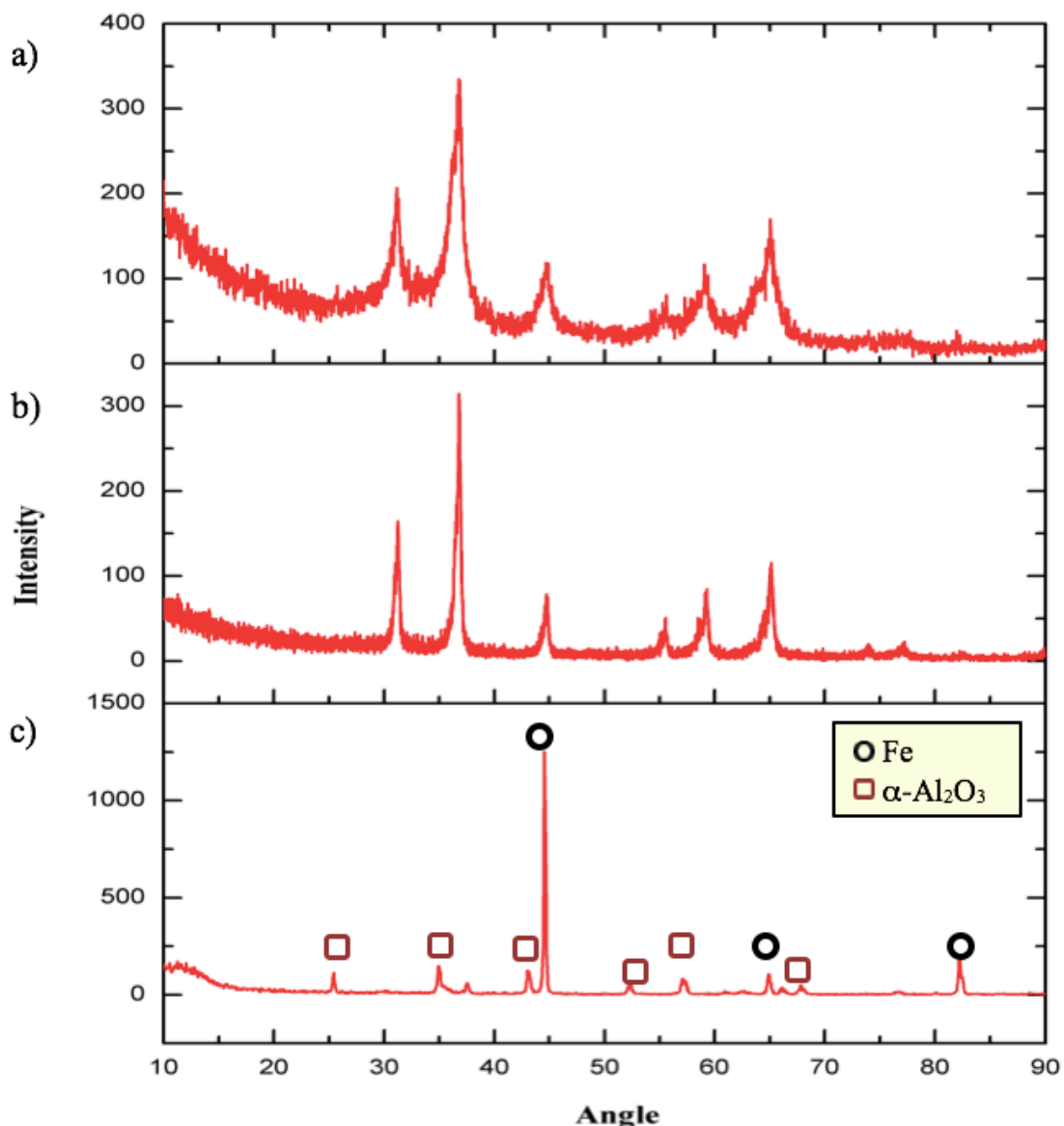


Figure 9.11 XRD patterns of synthesized samples of a) SC-FA-G1, b) SC-FA-G2 and c) SC-FA-G2-H

The X-ray diffraction peaks of SC-FA-S1, SC-FA-S2 and SC-FA-S2-H were shown in Figure 9.12, respectively.

The X-ray diffraction peaks of SC-FA-S1 and SC-FA-S2, synthesized by solution combustion method, using 50 % of stoichiometric amount of sucrose and stoichiometric amount of sucrose as a fuel (100 %), respectively, were presented in Figure 9.12a-b. XRD analysis suggested that the sample produced seem to be amorphous structure.

The X-ray diffraction peaks of SC-FA-S2-H synthesized by solution combustion method using stoichiometric amount of sucrose as a fuel (100 %) then calcined in a

furnace and reduced under hydrogen atmosphere, was presented in Figure 9.12c. The X-ray patterns of SC-FA-S2-H were similar to SC-FA-U2-H and SC-FA-G2-H. The diffraction peaks at 2θ values of 25.57° , 35.15° , 37.72° , 43.33° , 52.56° , 57.51° , 61.17° and 66.43° . From these peaks, XRD analysis suggested that the sample produced is α - Al_2O_3 (96-900-9784 entry number). Moreover, the diffraction peaks at 2θ values of 44.75° , 65.10° and 82.39° . From these peaks, XRD analysis suggested that the sample produced is iron (Fe) (96-411-3932 entry number). The data obtained from XRD analysis showed that the composition of SC-FA-S2-H samples was 60.7 % Al_2O_3 and 39.3 % Fe.

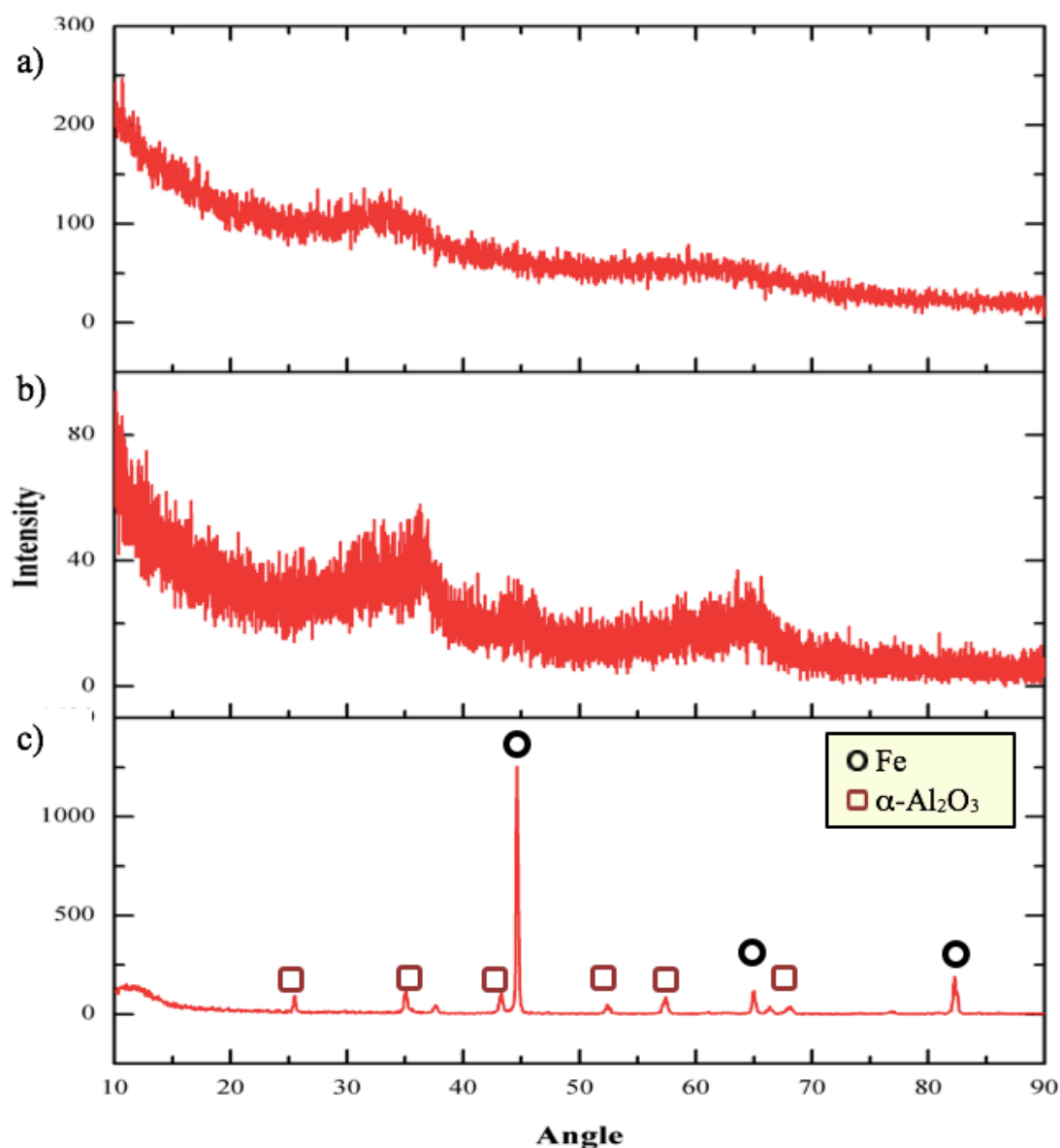


Figure 9.12 XRD patterns of synthesized samples of a) SC-FA-S1, b) SC-FA-S2 and c) SC-FA-S2-H

9.2.2 Scanning Electron Microscopy Analysis

The morphology and particle size of iron based magnetic aluminium oxide nanocomposites were analysed by Scanning Electron Microscopy (SEM).

The SEM images of SC-FA-U2-H, synthesized by solution combustion method, using stoichiometric amount of urea as a fuel (100 %) then calcined in furnace and reduced under hydrogen atmosphere, was shown in Figure 9.13. From SEM images, the composites were synthesized successfully in nanoscale, by using urea as a fuel. The particle sizes of SC-FA-U2-H were obtained in the range of 200 and 300 nm (Figure 9.13).

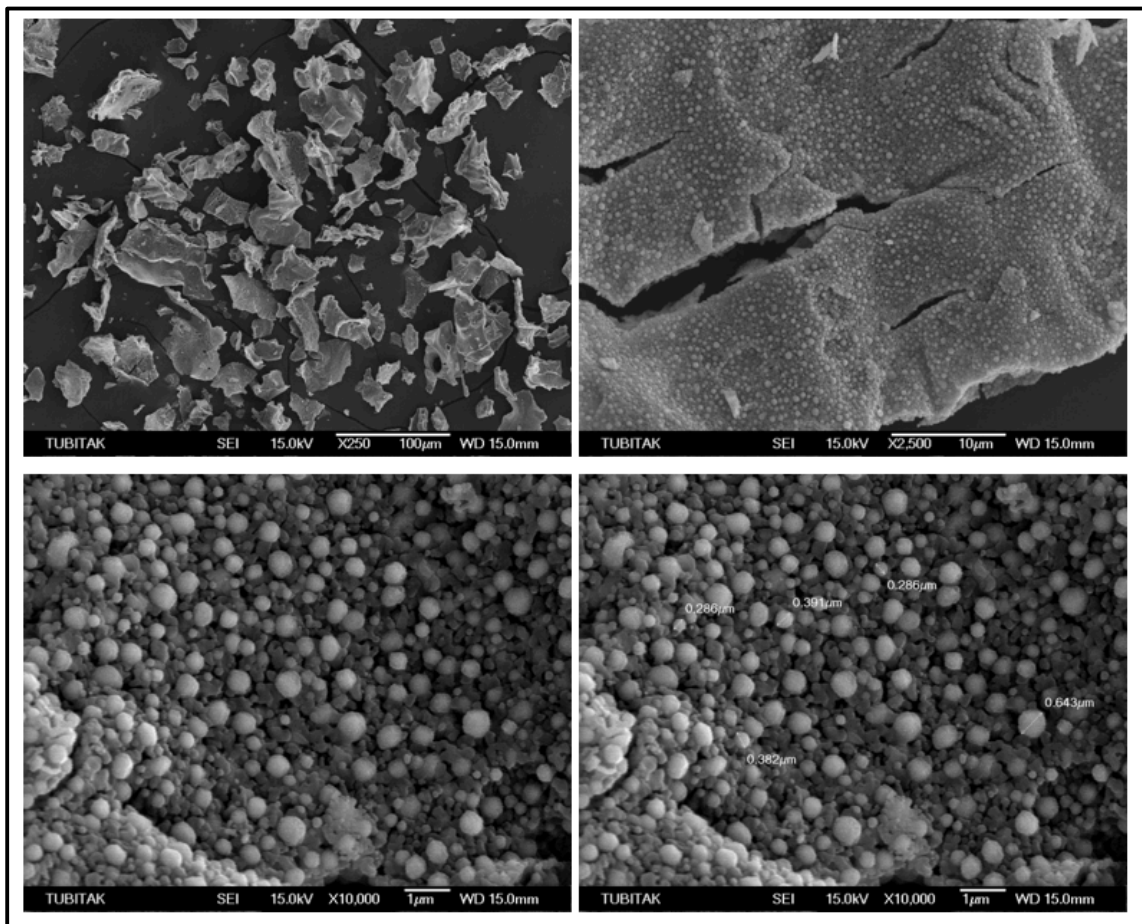


Figure 9.13 SEM microscopy images of SC-FA-U2-H

The SEM images of SC-FA-G2-H, synthesized by solution combustion method, using stoichiometric amount of glycine as a fuel (100 %) then calcined in furnace and reduced under hydrogen atmosphere, was shown in Figure 9.13. From the SEM images of

SC-FA-G2-H it was observed that iron based magnetic aluminium oxide SC-FA-G2-H had smaller particle sizes around 200 nm. Besides, the sample also contains very small particles as seen in Figure 9.14. Moreover, SEM analysis shows the formation of porous and spherical particles.

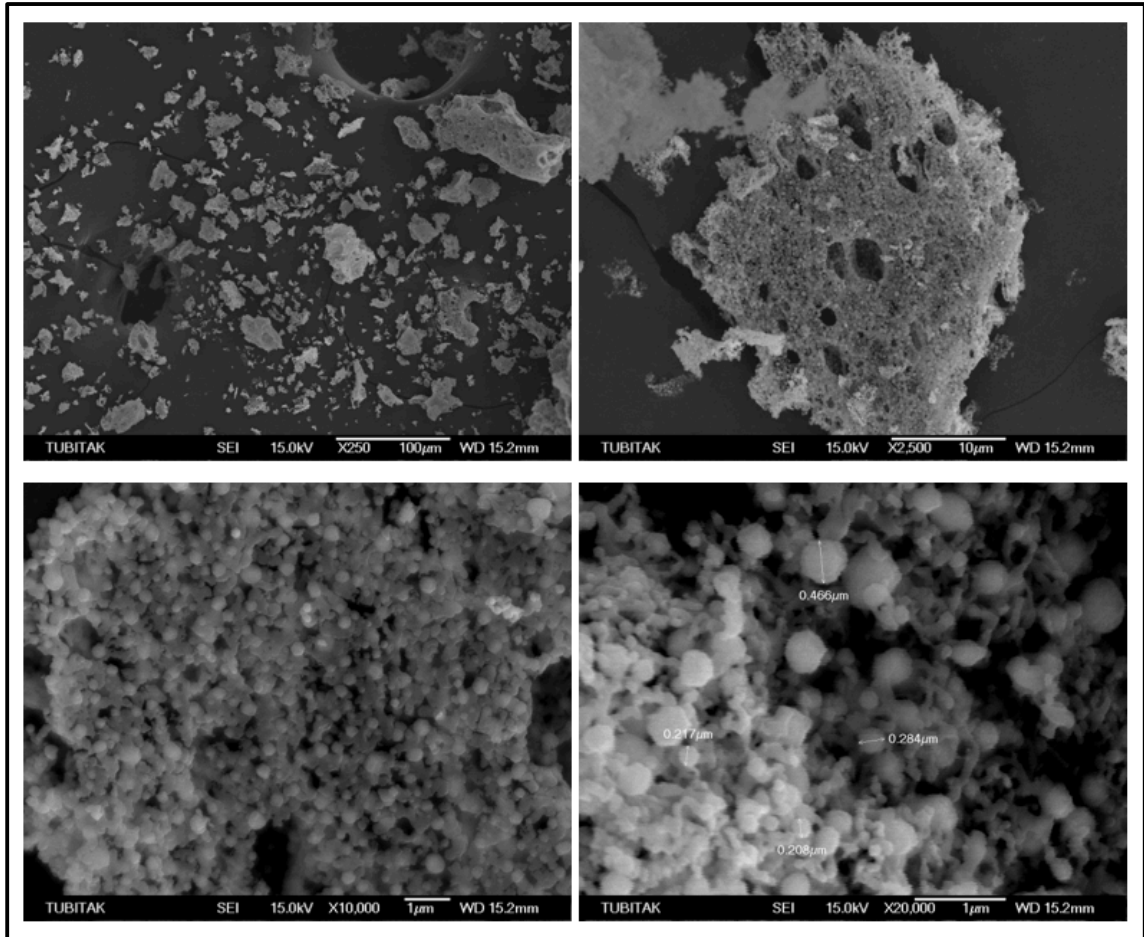


Figure 9.14 SEM microscopy images of SC-FA-G2-H

The SEM images of SC-FA-S2-H, synthesized by solution combustion method, using stoichiometric amount of sucrose as a fuel (100 %) then calcined in a furnace and reduced under hydrogen atmosphere, was shown in Figure 9.14. From SEM images of SC-FA-S2-H, homogenous particle size distribution was obtained. Average particle size of sample was determined as approximately 300 nm, and the particle morphology was spherical (Figure 9.15).

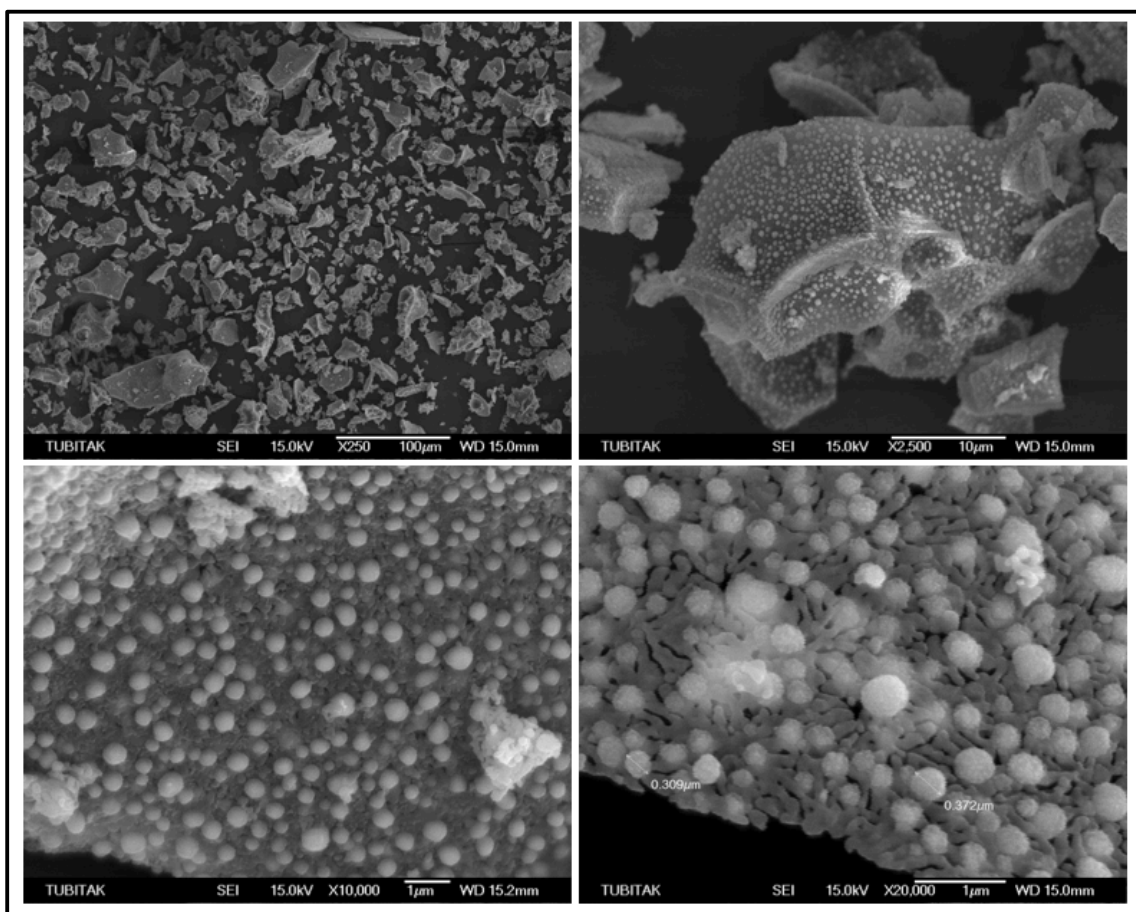


Figure 9.15 SEM microscopy images of SC-FA-S2-H

The SEM microscopy images of other synthesized samples such as SC-FA-U1, SC-FA-U2, SC-FA-G1, SC-FA-G2, SC-FA-S1 and SC-FA-S2 were given in Appendix A.

9.2.3 Scanning Electron Microscopy (SEM) – Energy Dispersive X-ray Spectroscopy (EDS) Analysis

The SEM-EDS analysis of SC-FA-U2-H, SC-FA-G2-H and SC-FA-S2-H, synthesized by solution combustion method, using stoichiometric amount of urea, glycine and sucrose (100 %) as a fuel respectively, then calcined in a furnace and reduced under hydrogen atmosphere, were shown in Figure 9.16a-c.

SC-FA-U2-H, SC-FA-G2-H and SC-FA-S2-H were synthesized to contain 50 % by weight of Fe. From EDS analysis, SC-FA-U2-H, SC-FA-G2-H and SC-FA-S2-H were included 59.2, 60.08 and 46.6 % weight percentages of Fe, respectively. The compositional analysis of synthesized samples of SC-FA-U2-H, SC-FA-G2-H and

SC-FA-S2-H obtained from Energy Dispersive X-ray Spectroscopy (EDS) analysis were given in Table 9.1.

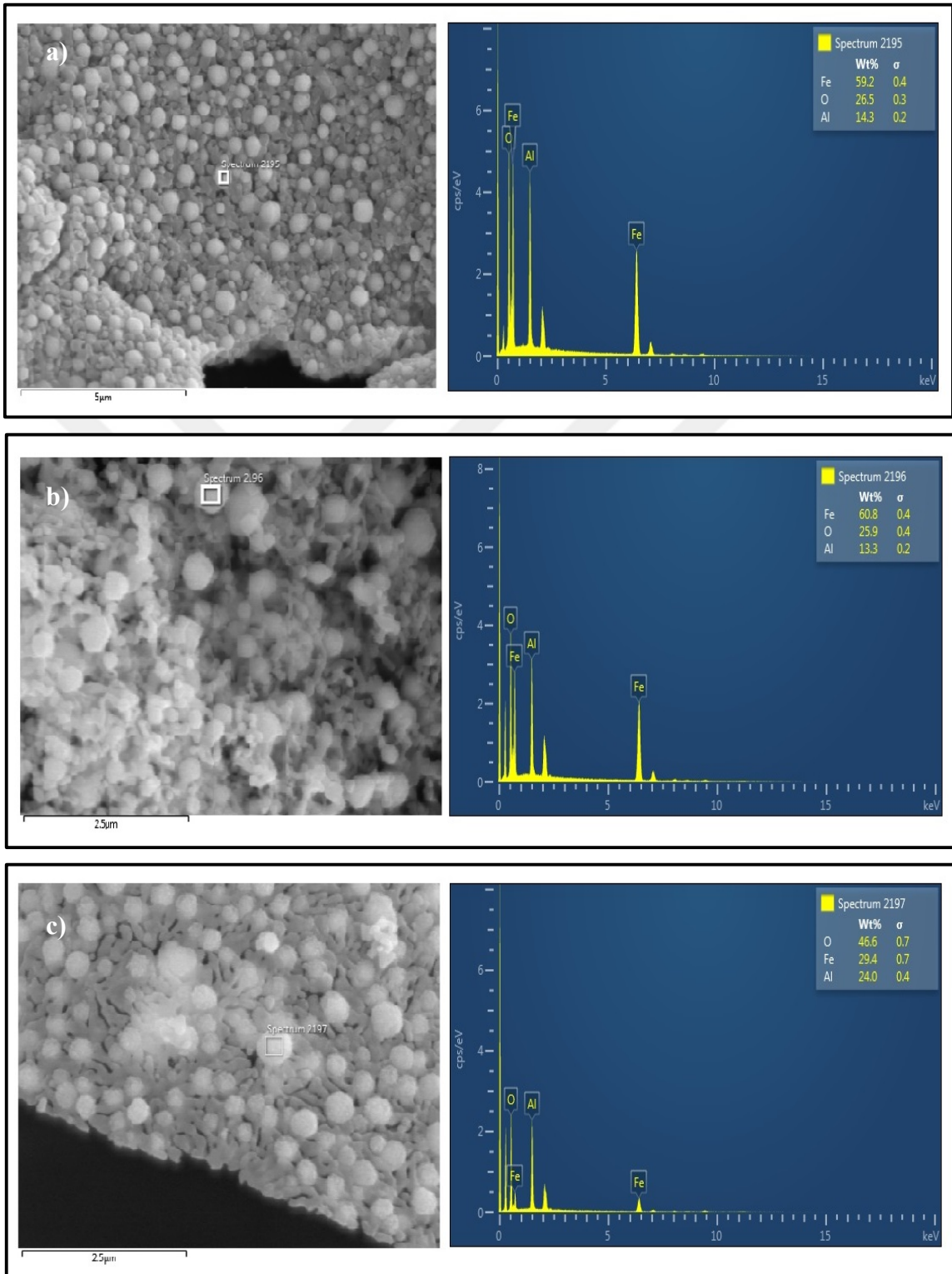


Figure 9.16 SEM micrographs and EDS analysis of synthesized samples of a) SC-FA-U2-H, b) SC-FA-G2-H and c) SC-FA-S2-H

Table 9.1 The compositional analysis of synthesized samples of SC-FA-U2-H, SC-FA-G2-H and SC-FA-S2-H obtained from EDS analysis

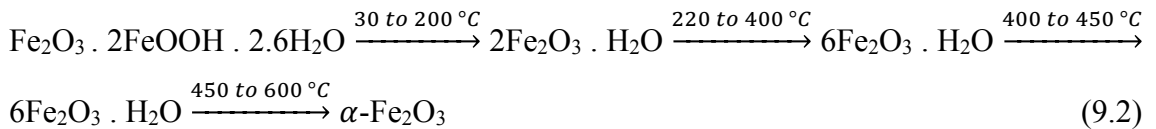
Sample name	Fe (wt %)	O (wt %)	Al (wt %)
SC-FA-U2-H	59.2	26.5	14.3
SC-FA-G2-H	60.08	25.9	13.3
SC-FA-S2-H	46.6	29.4	24.0

9.2.4 Thermogravimetric/Differential Thermal Analysis

Thermogravimetric and differential thermal analysis (TG/DTA) were performed with the synthesized samples without calcination. The analyses were performed from ambient temperature to 1200 °C in air atmosphere.

TG/DTA analysis of SC-FA-U1, synthesized by solution combustion method, using 50 % of stoichiometric amount of urea as a fuel was shown in Figure 9.17. According to TG and DTG curves, initial mass loss of 14.2 % from room temperature to 205 °C, corresponding to the evaporation of absorbed water [102]. The second mass loss was observed as 10.4 % at the temperature range of 205 to 700 °C. Lucio-Ortiz et al. (2011) [100] suggested that the mass loss can be related to the rest of nitrates and the boehmite transformation into aluminium oxide.

As seen in Figure 9.17a, very small amount of mass increase was occurred at around 770 °C for sample of SC-FA-U1. This could be related with the adsorption of oxygen on the particle surface or thermal transformation of iron (III) oxide hydrate as stated by Kalska-Szostko et al. (2015) [103]. Prasad et al. [104] explained the thermal transformation of iron (III) oxide hydrate using Equation (9.2) as follows;



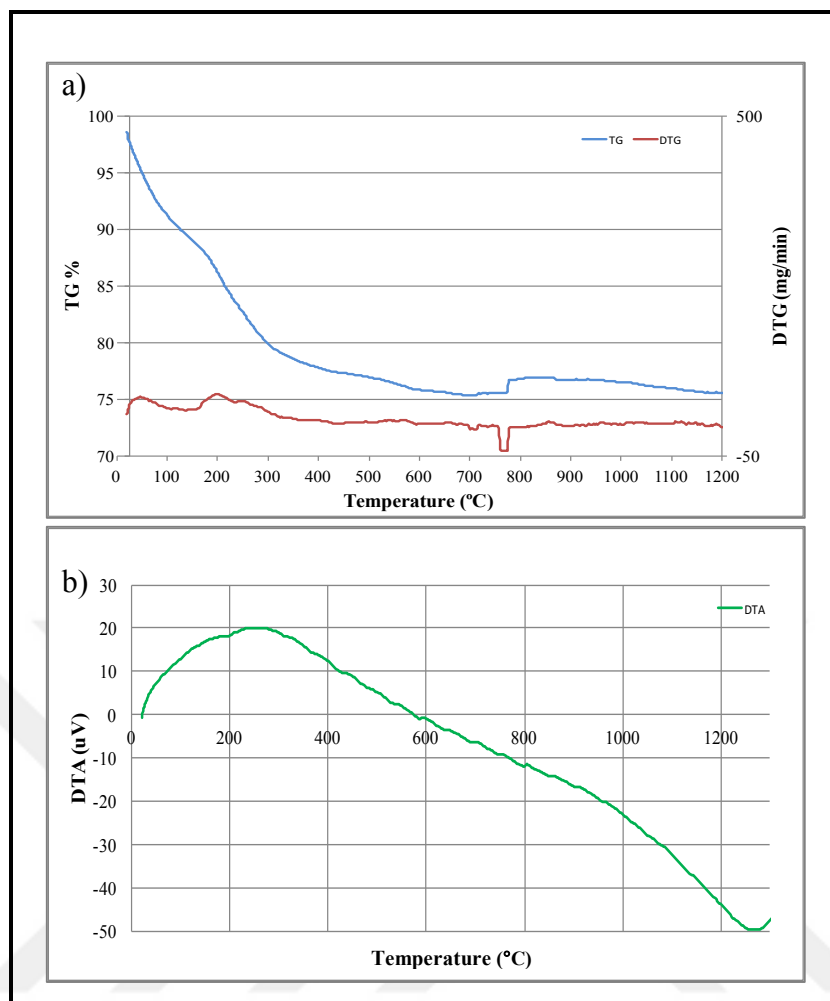


Figure 9.17 a) TG/DTG and b) DTA curves of SC-FA-U1

TG/DTA analysis of SC-FA-U2, synthesized by solution combustion method, using stoichiometric amount of urea as a fuel (100 %) was shown in Figure 9.18. According to TG and DTG curves of SC-FA-U2, initial mass loss of 7 % between ambient temperatures to 215 °C can be attributed to physically absorbed water. The second mass loss was detected as 5.7 % at the temperature range of 215 to 400 °C due to the decomposition of nitrates, boehmite-aluminium oxide conversion and formation of iron oxide as stated by Maldonado et al (2014) [102]. A slight increase of mass was observed for SC-FA-U2 in Figure 9.18a. The reason of the mass gain can be explained by the adsorption of oxygen on the particle surface or thermal transformation of iron (III) oxide hydrate as stated by Kalska-Szostko et al. (2015) [103] Prasad and Rao (1984) [104] in their study.

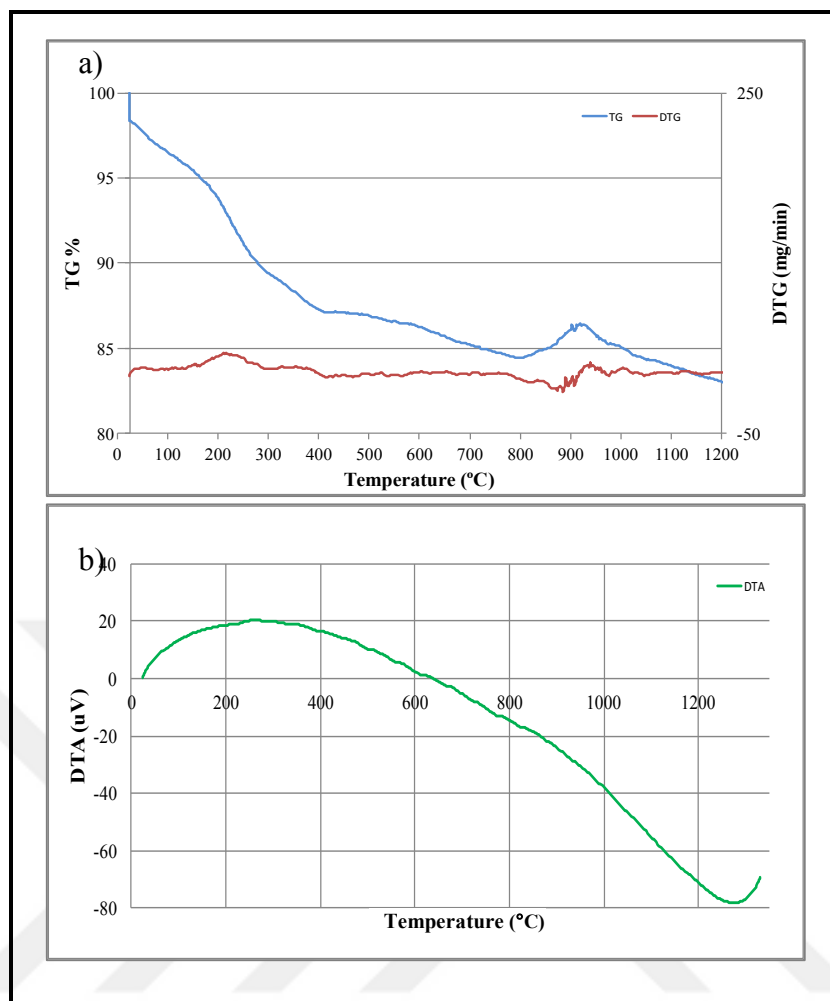


Figure 9.18 a) TG/DTG and b) DTA curves of SC-FA-U2

TG/DTA analysis of SC-FA-G1, synthesized by solution combustion method, using 50 % of stoichiometric amount of glycine as a fuel was shown in Figure 9.19. According to TG and DTG curves of SC-FA-G1, initial mass loss of 10 % between room temperature to 261 °C can be attributed to physically absorbed water. The second mass loss was 4 % at the temperature range of 261 to 410 °C, corresponding to the decomposition of nitrates, boehmite aluminium oxide conversion and formation of iron oxide as stated by Maldonado et al. (2014) [102] in their study. A slight increase of mass was observed for SC-FA-G1 in Figure 9.19a. The cause of the mass gain may be adsorption of oxygen on the particle surface or phase transformation of iron oxide as stated by Kalska-Szostko et al. (2015) [103] in their study. In addition to this, the colour of SC-FA-G1 changed after thermogravimetric analysis.

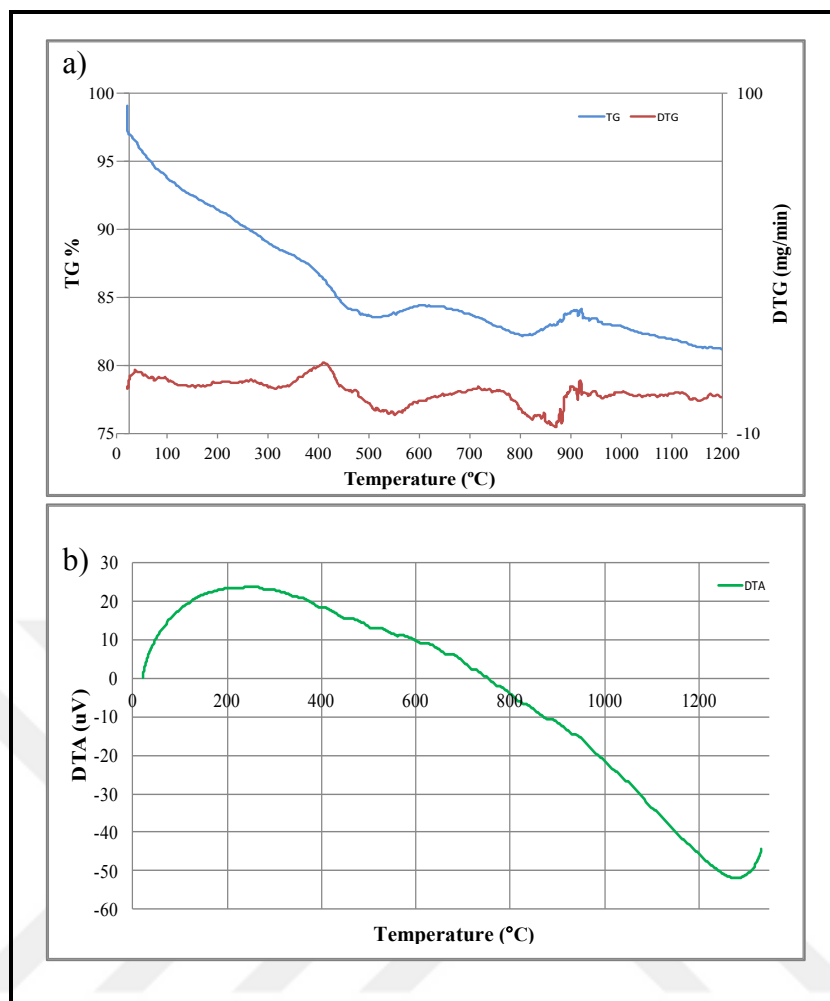


Figure 9.19 a) TG/DTG and b) DTA curves of SC-FA-G1

TG/DTA analysis of SC-FA-G2, synthesized by solution combustion method, using stoichiometric amount of glycine as a fuel (100 %) was shown in Figure 9.20. According to TG and DTG curves of SC-FA-G2, the mass loss was 6 % between ambient temperature and 450 °C, corresponding to evaporation of physically absorbed water, boehmite aluminium oxide conversion and formation of iron oxide by Maldonado and et al. [102]. From TG curve of SC-FA-G2, a slight increase of mass was observed. The reason of the mass gain may be adsorption of oxygen on the particle surface or phase transformation of iron oxide as stated by Kalska-Szostko et al. (2015) [103] in their study.

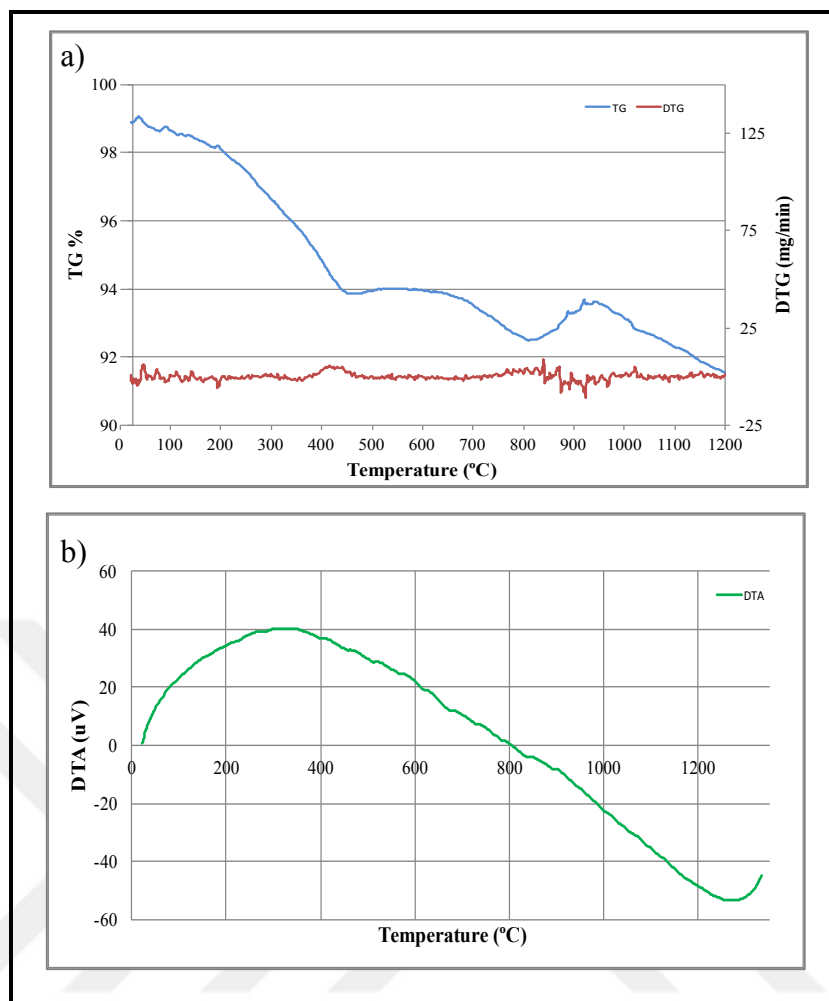


Figure 9.20 a) TG/DTG and b) DTA curves of SC-FA-G2

TG/DTA analysis of SC-FA-S1, synthesized by solution combustion method, using 50 % of stoichiometric amount of sucrose as a fuel was shown in Figure 9.21. According to TG and DTG curves of SC-FA-S1, the mass loss region (25-350 °C), endothermic reaction was occurred. And this could be attributed to the evaporation of absorbed water, formation of iron oxide and boehmite-aluminium oxide conversion as stated by Maldonado et al. (2014) [102]. Besides, the total mass loss of SC-FA-S1 was obtained as 32 %.

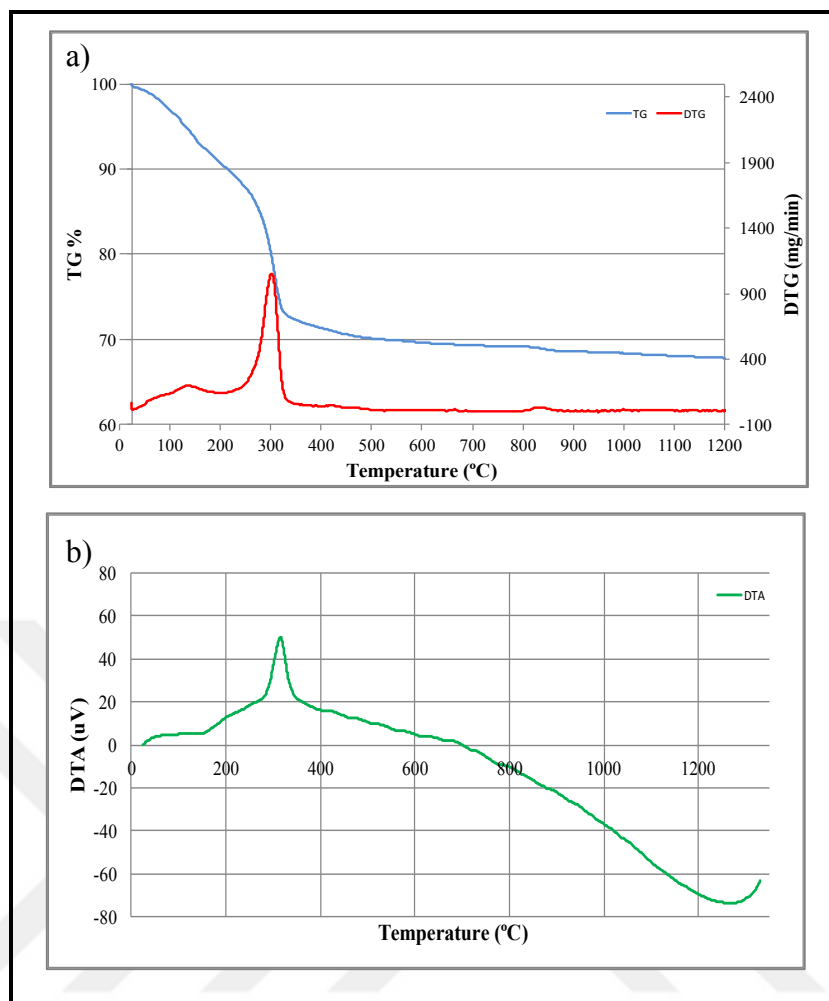


Figure 9.21 a) TG/DTG and b) DTA curves of SC-FA-S1

TG/DTA analysis of SC-FA-S2, synthesized by solution combustion method, using stoichiometric amount of sucrose as a fuel (100 %) was shown in Figure 9.22. According to TG and DTG curves of SC-FA-S2, the significant mass loss was detected in three regions. In the first region, 11 % of mass loss occurred at the temperature of between 25 and 200 °C, this can be attributed to removal of absorbed water. In the second region, 3.5 % mass loss was observed at the temperature from 200 to 315 °C. This can be associated with decomposition of nitrates and evaporation of water. In the final region, 7.5 % mass loss was observed between 315 and 450 °C, corresponding to the conversion of boehmite into γ -Al₂O₃ and formation of iron oxide as stated by Maldonado et al. (2014) [100] and Lucio-Ortiz et al. (2011) [102] in their study.

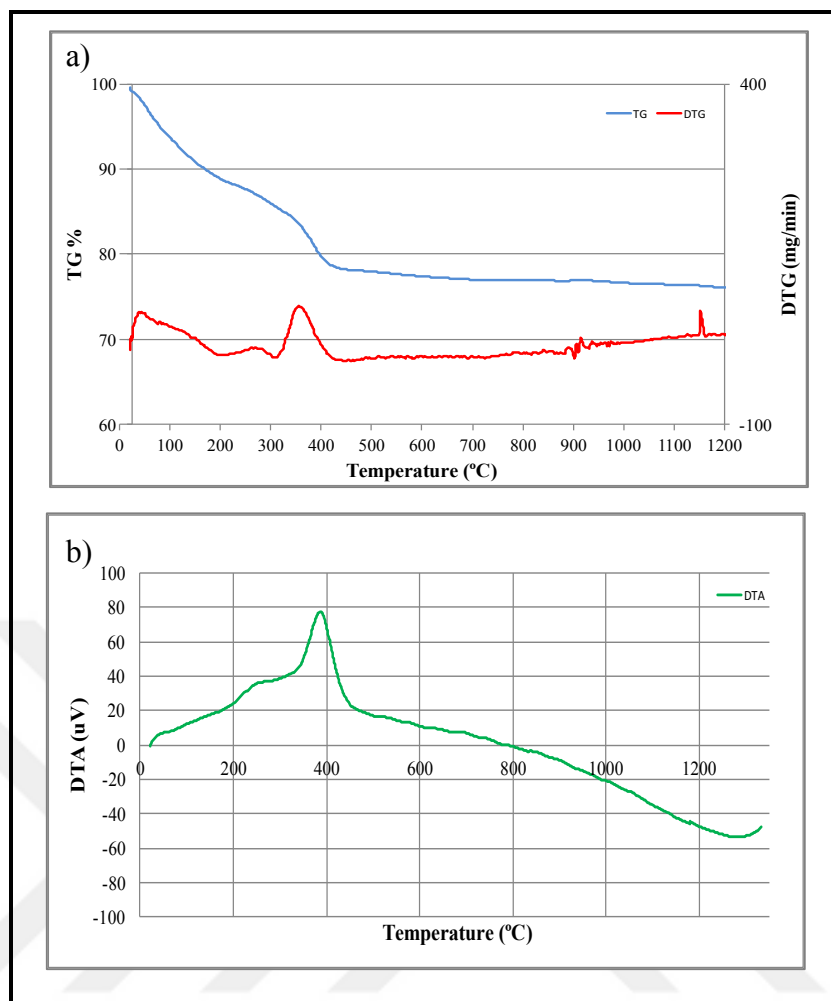


Figure 9.22 a) TG/DTG and b) DTA curves of SC-FA-S2

9.2.5 Surface Area and Porosity Analysis

Among other synthesized samples examined according to the results obtained from XRD and SEM analysis, only the sample of SC-FA-G2 was shown more porosity. So that, SC-FA-G2 sample was chosen for further analysis of the surface area and porosity. The adsorption-desorption isotherms and pore volume analysis by BJH desorption method of SC-FA-G2 sample were shown in Figure 9.23.

From IUPAC classifications of adsorption isotherms, the Type II isotherm (Figure 5.3) was found as the best adsorption-desorption isotherms for SC-FA-G2. Type II isotherm obtained with a non-porous or macroporous adsorbent as stated by Alothman (2012) [105]. The BET surface area of SC-FA-G2 was found as 19.6956 m²/g. Moreover, Type II(b) isotherm exhibit Type H3 hysteresis loop. Similar hysteresis loop was also obtained in the present study with SC-FA-G2 in the partial pressure range of 0.45 to 0.98 (Figure 9.23a). The narrow hysteresis loop is the result of inter-particle capillary condensation, usually within a nonrigid aggregate as stated by Rouquerol et al. (2013) [62].

The pore size analysis of SC-FA-G2 was presented in Figure 9.23b. The pore size values were approached to 18.7428 and 14.8318 nm after adsorption and desorption analysis by the BJH method, respectively. Surface area and porosity analysis of SC-FA-G2 were given in Table 9.2.

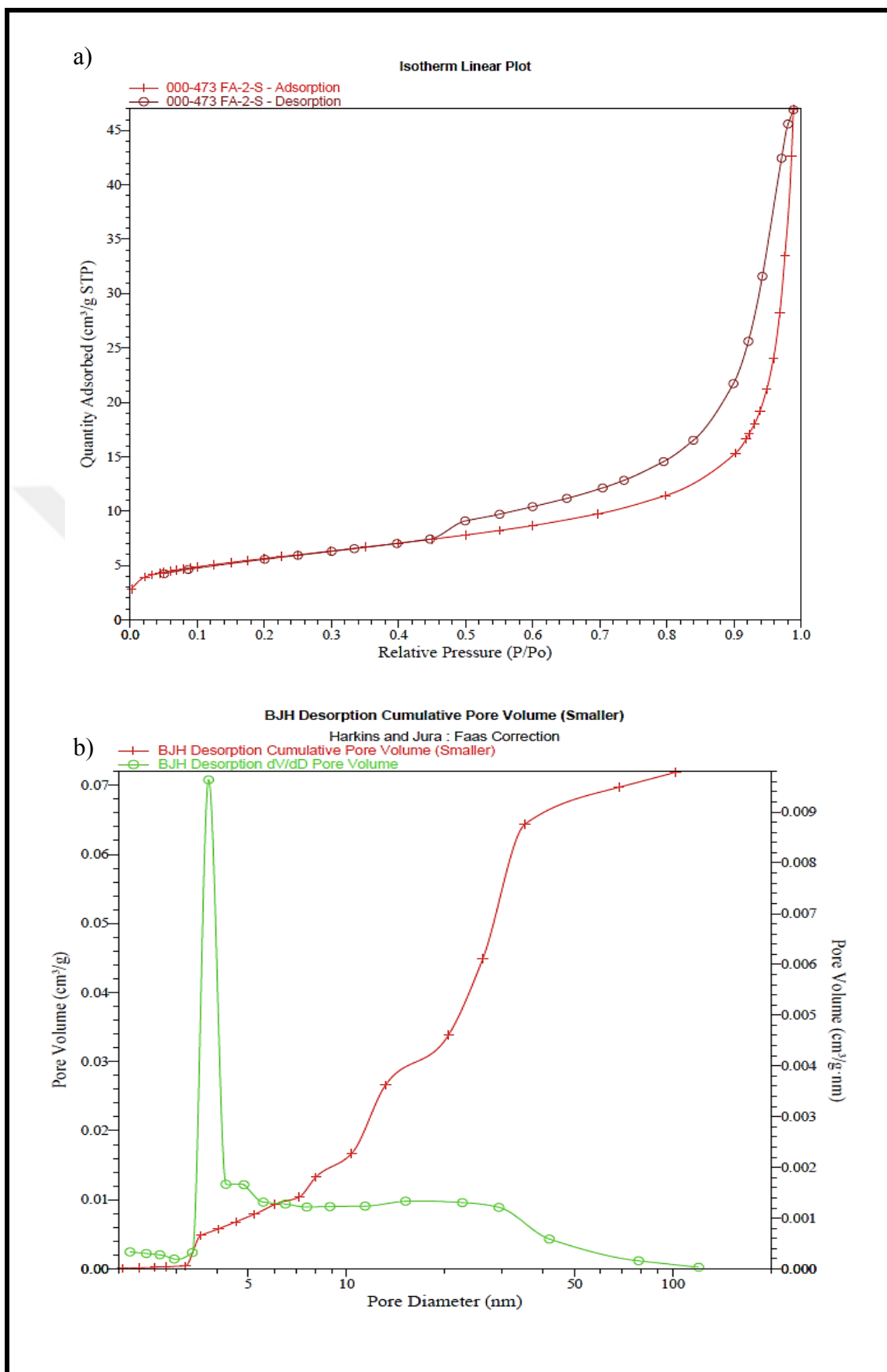


Figure 9.23 a) The adsorption-desorption isotherms and b) Pore volume analysis by BJH desorption method of SC-FA-G2

Table 9.2 Surface area and porosity analysis of SC-FA-G2

S_{BET} (m²/g)	19.6956
Pore volume_(BJH adsorption) (cm³/g)	0.06932
Pore volume_(BJH desorption) (cm³/g)	0.07188
V_{micropore} (cm³/g)	0.002338
Pore size_(BJH adsorption) (nm)	18.7428
Pore size_(BJH desorption) (nm)	14.8318
Average particle size (nm)	304.6369

9.3 Reactive Blue 19 Dye Removal by Iron Based Magnetic Aluminium Oxide Nanocomposites

According to the data obtained from the characterization studies including surface area and porosity analysis, only the sample of SC-FA-G2 was decided to choose as an adsorbent for Reactive Blue 19 dye removal for further studies. The experimental design was performed by using a Design Expert 11.0 experimental design programme to optimize the process conditions of RB19 dye adsorption. For this purpose, Box-Behnken design method was applied to investigate the effects of parameters on adsorption of RB19 dye onto iron based magnetic aluminium oxide SC-FA-G2 nanocomposite. The factor levels were coded as -1 (low), 0 (central point) and 1 (high). The process parameters chosen for experimental design of RB19 dye adsorption were shown in Table 9.3. According to Box-Behnken Design, 17 experiments were performed to optimize the process parameters such as pH, temperature and adsorbent amount on the RB19 dye removal efficiency.

Table 9.3 The parameters chosen for experimental design of RB19 dye adsorption

	Low (-1)	Centre (0)	High (+1)
pH	2	4	6
Temperature (°C)	25	35	45
Adsorbent amount (mg/50 mL)	200	400	600

9.3.1 Box-Behnken Design Method Analysis

According to the experiments defined by using Box-Behnken design method, Reactive Blue 19 removal percentages were presented in Table 9.4. The removal percentages of five experiments at centre point (pH of 4, 35 °C and 400 mg SC-FA-G2/50 mL) were found to close each other and associated with minimization of experimental errors. The minimum dye removal was determined as 25 % at the following conditions; pH of 6, 35 °C and 200 mg SC-FA-G2/50 mL. The maximum dye removal was determined as 100 % at the following conditions;

- pH of 2, 25 °C and 400 mg SC-FA-G2/50 mL,
- pH of 2, 35 °C and 600 mg SC-FA-G2/50 mL,
- pH of 2, 45 °C and 400 mg SC-FA-G2/50 mL

Due to its lower energy requirement, the temperature of 25 °C was chosen as the optimum value.

Table 9.4 Box-Behnken experimental design matrix and experimental responses of RB19 dye adsorption onto sample of SC-FA-G2

Run	X ₁ (pH)	X ₂ (T °C)	X ₃ (mg/50 mL)	Dye removal (%)
1	6	45	400	65
2	6	35	600	95
3	4	35	400	58
4	4	35	400	60
5	4	35	400	63
6	2	35	200	93
7	4	45	200	48
8	2	25	400	100
9	2	45	400	100
10	6	25	400	40
11	4	35	400	66
12	2	35	600	100
13	6	35	200	25
14	4	25	600	90
15	4	35	400	68
16	4	45	600	96
17	4	25	200	36

According to the Box-Behnken design method, the Equation (9.1) was developed using Design Expert 11.0 experimental design programme. The analysis of variance (ANOVA) was given in Table 9.5 for the model developed.

$$Y_{SC-FA-G2} = - 21.00*X_1 + 5.38*X_2 + 22.38*X_3 + 6.25*X_1*X_2 + 15.75*X_1*X_3 - 1.50*X_2*X_3 + 12.00*X_1^2 + 1.25*X_2^2 + 3.75*X_3^2 + 63.00 \quad (9.1)$$

Table 9.5 ANOVA analysis data for the model developed

Source	Sum of Squares	df	Mean Square	F-value	P-value
Model	9610.31	9	1067.81	35.13	<0.0001
A-pH	3528.00	1	3528.00	116.08	<0.0001
B-Temp.	231.13	1	231.13	7.60	0.0282
C-Ads. Amount	4005.13	1	4005.13	131.78	<0.0001
AB	156.25	1	156.25	5.14	0.0577
AC	992.25	1	992.25	32.65	0.0007
BC	9.00	1	9.00	0.2961	0.6032
A²	606.32	1	606.32	19.95	0.0029
B²	6.58	1	6.58	0.2165	0.6559
C²	44.47	1	44.47	1.46	0.2657
Residual	212.75	7	30.39		
Lack of Fit	144.75	3	48.25	2.84	0.1697
Pure Error	68.00	4	17.00		
Cor Total	9823.06	16			

The analysis of variance is essential to test significance and adequacy of the model. As shown in Table 9.5, the Model F-value of 35.13 implies the model is significant. The significance of each term was determined by P-value. P values less than 0.001 indicated the model terms were significant. The terms X_1 , X_2 , X_3 , $X_1.X_3$ and X_1^2 were significant, with very small P-values (P-values < 0.05). The other term coefficients were not significant (P-values > 0.05). The Lack of Fit F-value of 2.84 is not significant as the P-value is >0.05. The non-significance lack of fit F-value showed that the model was valid for the present work, as stated by Mourabet et al. (2017) [106] in their study.

From Equation (9.1), it can be seen that the temperature and adsorbent amount have positive effect on RB19 dye removal percentage. The coefficient of determination R^2 and adjusted R^2 of the model were obtained as 0.9783 and 0.9505, respectively. The difference between the predicted and experimental data were small indicated that the adequacy of the model to the response (Fig 9.24).

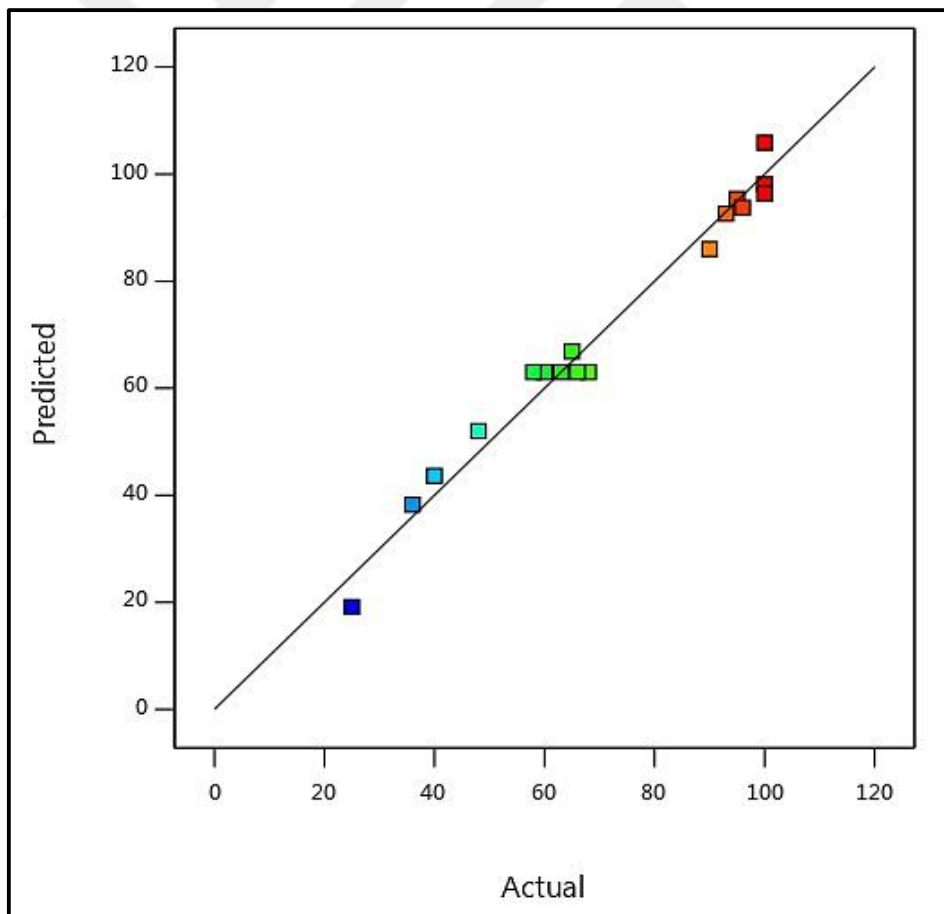


Figure 9.24 Predicted data versus experimental data of RB19 dye removal (%)

Three-dimensional response surface plots were constituted with the Design Expert 11.0 experimental design programme presenting the effects and their interactions on the parameters of RB19 dye adsorption process (Figures 9.25-9.27).

As can be seen from Figures 9.25 and 9.26, the decrease in pH resulted in the increase for RB19 dye removal percentage. From Figures 9.26 and 9.27, the removal percentage of RB19 dye increased with increasing adsorbent amount due to the availability of more surface area of the adsorbent for adsorption. The pH and adsorbent amount were found the most effective parameters influencing the dye removal percentage. In addition, the effect of temperature was found insignificant on RB19 dye removal.

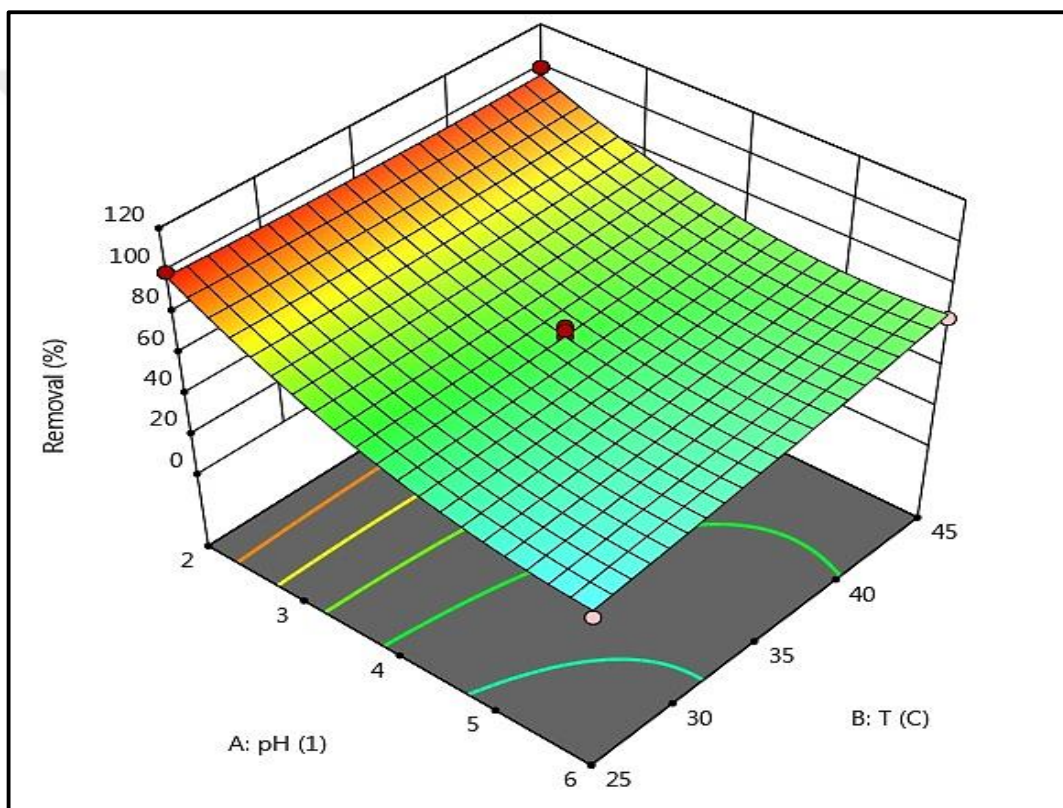


Figure 9.25 Response surface plot for the combined effects of pH and temperature on RB19 dye removal (%)

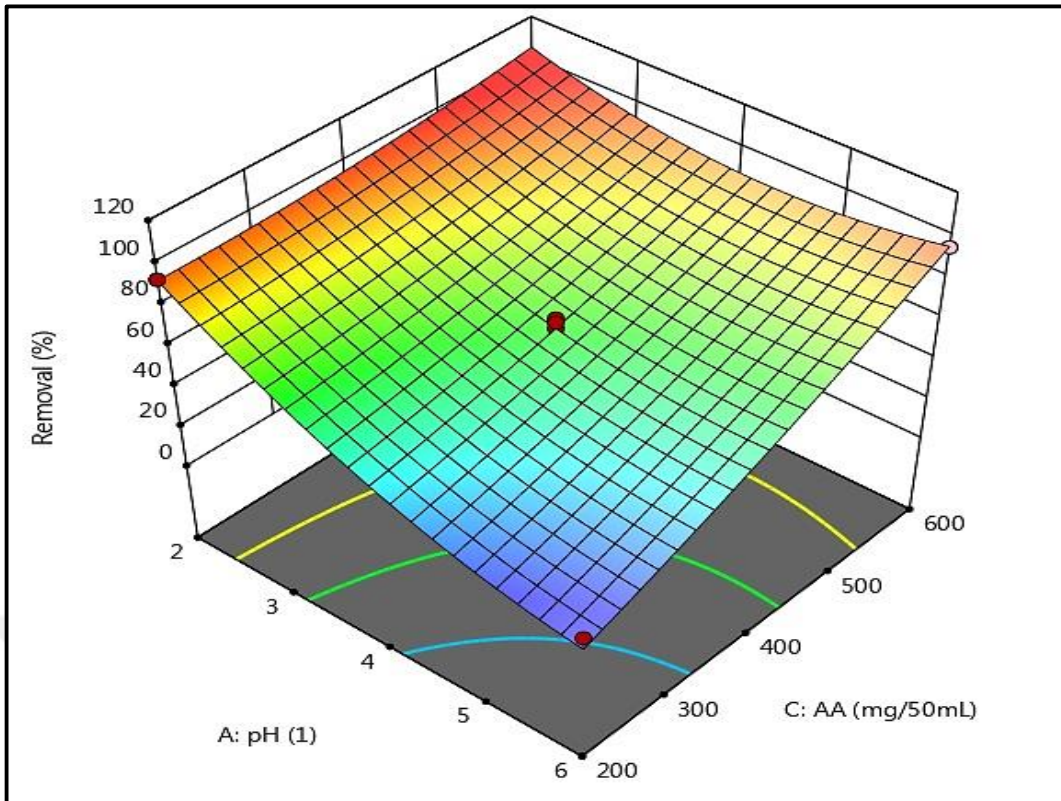


Figure 9.26 Response surface plot for the combined effects of pH and adsorbent amount on RB19 dye removal (%)

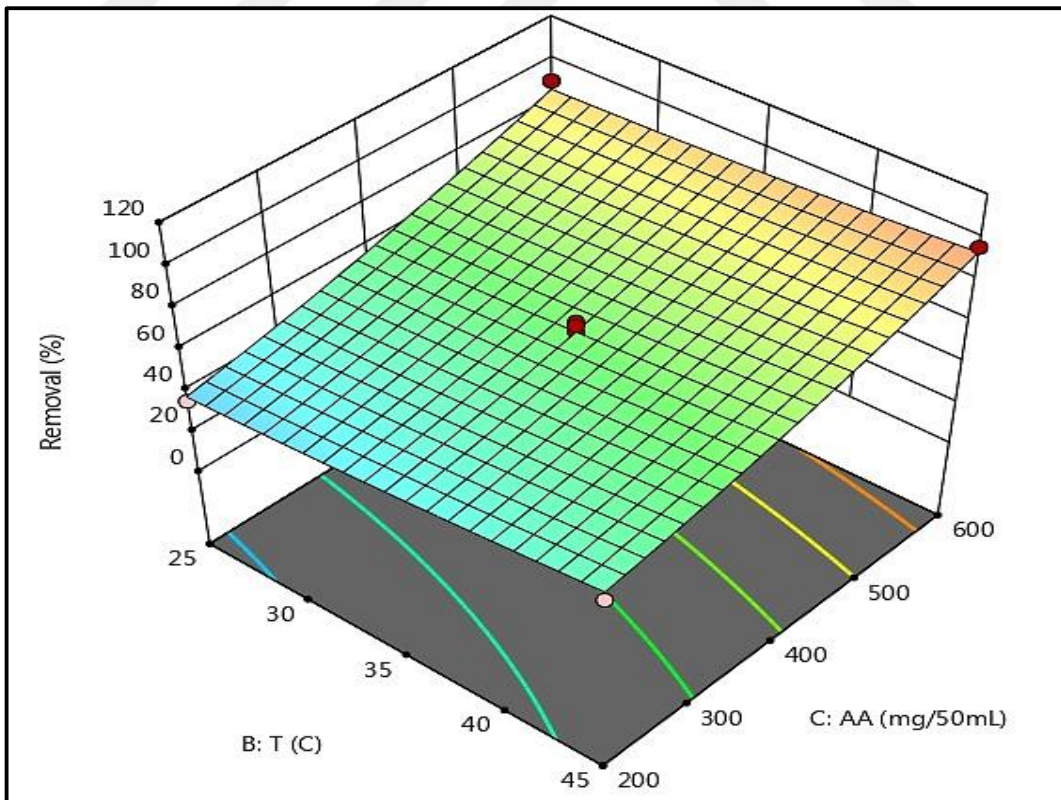


Figure 9.27 Response surface plot for the combined effects of temperature and adsorbent amount on RB19 dye removal (%)

9.3.2 Adsorption Isotherm Models

The adsorption isotherm is very important to evaluate the adsorption capacity. The convenience of three most common adsorption models; Langmuir, Freundlich and Temkin for RB19 dye adsorption onto SC-FA-G2 were investigated. The experiments were pursued at optimum conditions, pH of 2, 25 °C at various adsorbent amounts from 50 to 400 mg SC-FA-G2/50 mL. The estimated parameters and the statistical values of the models examined were presented in Table 9.6.

Table 9.6 The estimated parameters and statistical values of adsorption isotherm models

Adsorption Isotherm Models	Estimated parameters			
	Langmuir	Q_{\max} (mg/g)	b (L/mg)	R^2
55.2486		0.4067	0.9956	0.0275
Freundlich	K_F ($\text{mg}^{1-1/n}\text{L}^{1/n}\text{g}^{-1}$)	n	R^2	σ
	17.6617	3.2884	0.9768	0.1076
Temkin	A_T (L/g)	b_T (J/mol)	R^2	σ
	8.7938	284.0308	0.9982	0.8497

According to the results obtained, Langmuir isotherm model was determined as the most appropriate model with the high values of correlation coefficient (R^2) and low value of the standard deviation (σ), (Figure 9.28). From Table 9.6, even though Temkin isotherm model have high correlation coefficient value. But, it did not describe very well the data of RB19 dye adsorption onto SC-FA-G2, because of its high standard deviation value. Similarly, Freundlich isotherm model was not suitable for describing the adsorption data of RB19 dye removal.

The Curve Expert Professional 2.6.5 was used to determine parameters. The data obtained from the experiments of RB19 dye adsorption onto SC-FA-G2 were given in Table B.1 in Appendix-B section.

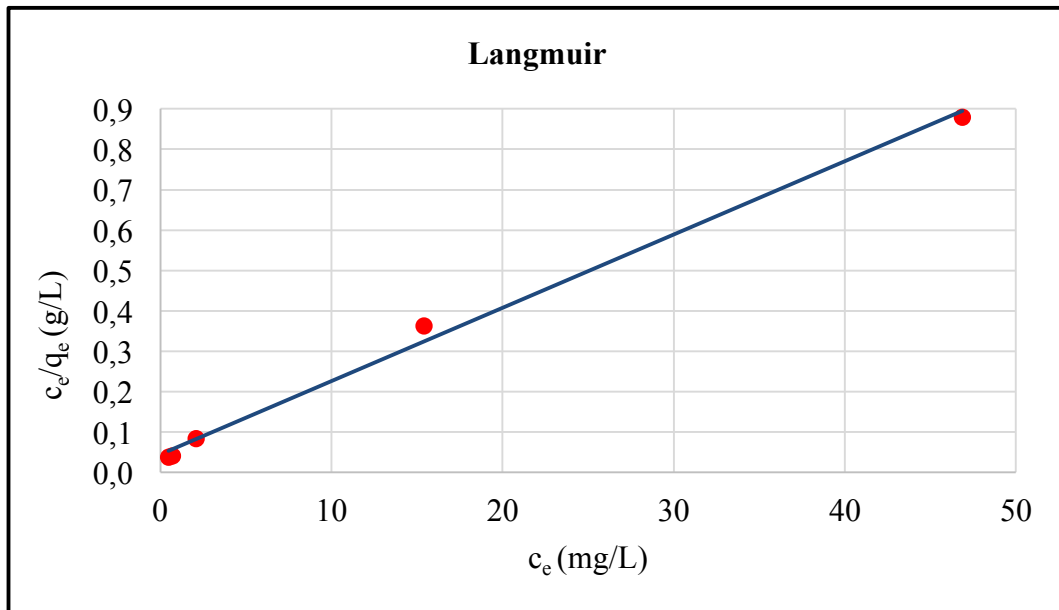


Figure 9.28 Langmuir adsorption isotherm model data of RB19 dye removal onto SC-FA-G2

9.3.3 Adsorption Kinetic Models

Determination of the adsorption kinetic is very important to plan and control of the adsorption process. For this reason, four adsorption kinetic models such as pseudo-first order, pseudo- second order, Elovich and the intra-particle diffusion models were used for the examination of RB19 dye removal onto SC-FA-G2 by adsorption. The estimated parameters and the statistical data of the models examined were presented in Table 9.7. Among other models examined, the most appropriate one was observed as pseudo-second order kinetic model due to its higher R^2 and lower σ values (Figure 9.29). The data obtained from the kinetic experiments of RB19 dye adsorption onto SC-FA-G2 were presented in Tables C.1-3 in Appendix-C section.

Table 9.7 The estimated parameters and statistical values of adsorption kinetic models

Kinetic Model Equation	Estimated Parameters	Adsorbent Amount (mg)		
		50	200	400
Pseudo-First Order	k_1 (min^{-1})	0.0599	0.1559	0.0778
	R^2	0.9277	0.8732	0.5929
	σ	0.1222	0.2781	0.4085
Pseudo-Second Order	k_{p2} ($\text{g}\cdot\text{mg}^{-1}\cdot\text{min}^{-1}$)	0.0184	0.0911	0.3333
	R^2	0.9972	0.9999	0.9999
	σ	0.0185	0.0045	0.0077
Elovich	α ($\text{mg}\cdot\text{g}^{-1}\cdot\text{min}$)	407.5982	3.1×10^9	7.3×10^{31}
	β ($\text{g}\cdot\text{mg}^{-1}$)	0.1546	1.0403	6.3816
	R^2	0.9459	0.9151	0.9617
	σ	0.2571	0.3220	0.2163
Intra Particle Diffusion	k_i ($\text{mg}\cdot\text{g}^{-1}\cdot\text{min}^{-2}$)	3.3443	0.4573	0.0821
	c_i ($\text{mg}\cdot\text{g}^{-1}$)	29.8260	21.6460	11.8550
	R^2	0.9154	0.7497	0.9561
	σ	0.6119	1.0525	0.4408

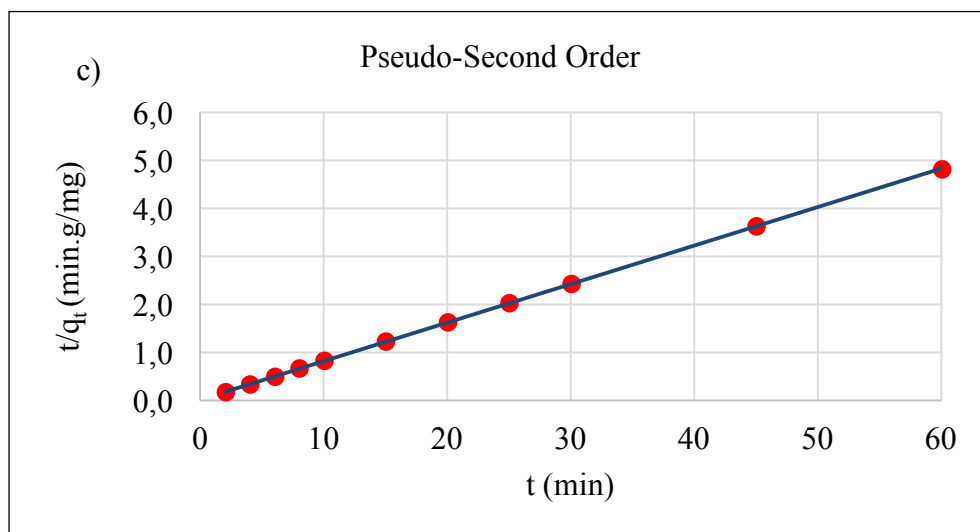
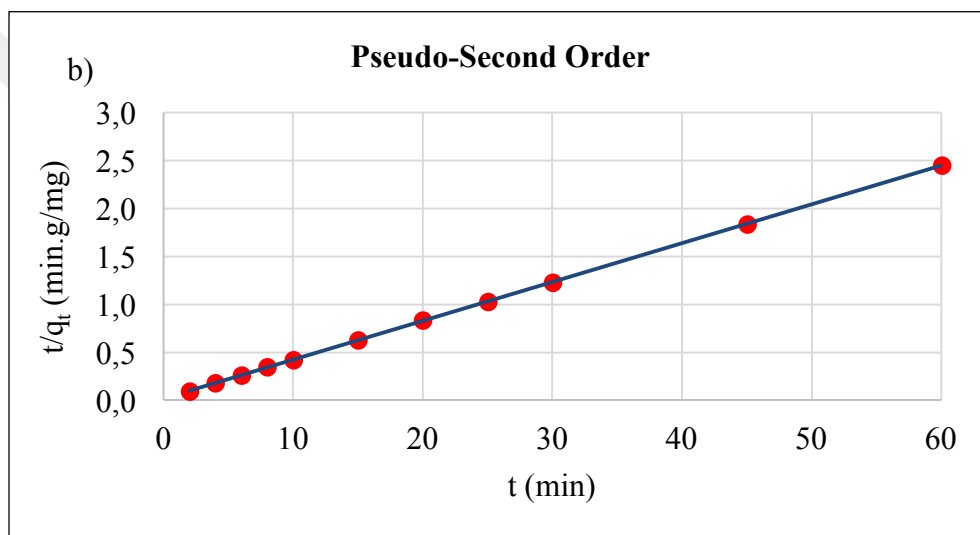
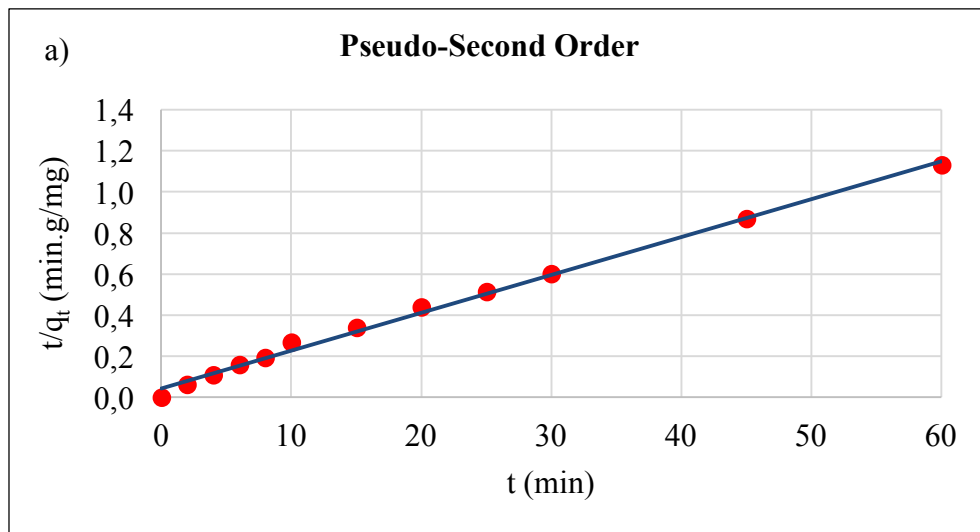


Figure 9.29 The linearized pseudo-second order kinetic model at various adsorbent amounts of a) 50 mg, b) 200 mg and c) 400 mg

CONCLUSIONS

Aluminium oxide nanoparticles and iron based magnetic aluminium oxide nanocomposites are widely used in many areas. There are several studies carried out for synthesis of nanoparticles and nanocomposites using various synthesis methods such as precipitation, sol-gel, hydrothermal synthesis, spray pyrolysis, solution combustion method and etc. In the present study, aluminium oxide nanoparticles and iron based magnetic aluminium oxide nanocomposites were synthesized by solution combustion method using various fuel types and amounts. Synthesized samples were characterized using devices such as XRD, SEM-EDS, TG/DTA and BET surface area and porosity analyser. According to the data obtained from the characterization studies, only the sample of SC-FA-G2, synthesized by solution combustion method using stoichiometric amount of glycine (100 %) as a fuel, was chosen to use as an adsorbent for dye removal. For this purpose, RB19 dye was chosen to investigate as it is one of the dyestuffs widely used in the textile industry.

The experimental set of RB19 dye removal was planned by using a Design Expert 11.0 experimental design programme according to Response Surface Methodology (RSM). According to Box-Behnken Design, 17 experiments were performed under various process conditions such as pH, temperature and adsorbent amount. RSM was used for optimizing and modelling of adsorption process of RB19 dye removal. The data obtained from the adsorption experiments of RB19 dye removal at the optimum process conditions were used for examination of most appropriate adsorption isotherm model and kinetic model.

The major findings of the present study were given as follows;

Aluminium Oxide Nanoparticles Synthesis:

- Aluminium oxide nanoparticles were synthesized by solution combustion method using two fuel types (urea and glycine) at two fuel amounts (stoichiometrically 50 and 100 %) (Table 10.1). The chemical compositions, morphologies and thermal behaviours of the samples synthesized (SC-A-U1, SC-A-U2, SC-A-G1 and SC-A-G2) were compared according to data obtained from characterization studies.
- XRD analysis of SC-A-U1 and SC-A-U2, synthesized by solution combustion method using 50 % of stoichiometric amount and stoichiometric amount of urea as fuel, respectively, and calcined 1000 °C for 1 h, showed α -Al₂O₃ formation. This result was also confirmed by thermogravimetric and differential thermal analysis data of SC-A-U1 and SC-A-U2 samples before calcination.
- However, SC-A-G1 and SC-A-G2, synthesized by solution combustion method using 50 % of stoichiometric and stoichiometric amount of glycine as fuel, respectively, and calcined 1000 °C for 1 h, showed θ -Al₂O₃ and γ -Al₂O₃ formation, respectively. This result was also confirmed by thermogravimetric and differential thermal analysis data of SC-A-G1 and SC-A-G2 samples before calcination.
- SEM images of SC-A-U1, SC-A-U2, SC-A-G1 and SC-A-G2, urea as a fuel promotes agglomeration of particles, whereas glycine as a fuel promotes the formation of small size and porous particle.
- Usage of glycine as a fuel may cause more vigorous reaction resulted in higher porosity compared to usage of urea as a fuel.

Iron Based Magnetic Aluminium Oxide Nanocomposites Synthesis:

- Iron based magnetic aluminium oxide nanocomposites were synthesized by solution combustion method using three fuel types (urea, glycine and sucrose) at two fuel amounts (stoichiometrically 50 and 100 %) (Table 10.2). The chemical compositions, morphologies, thermal behaviours, surface area, pore volume and average pore diameter of the samples synthesized were compared according to data obtained from characterization studies.
- XRD analysis of SC-FA-U1, synthesized by solution combustion method using 50 % of stoichiometric amount of urea fuel showed amorphous character. On the other

hand, XRD analysis of SC-FA-U2, synthesized by solution combustion method using stoichiometric amount of urea fuel showed crystalline structure of nanocomposite (Fe_3O_4 and Al_2O_3) formation.

- XRD analysis of SC-FA-G1 and SC-FA-G2 synthesized by solution combustion method using 50 % of stoichiometric and stoichiometric amount of glycine as a fuel, respectively, showed the crystalline structure. SC-FA-G1 comprises of Fe_3O_4 and $\theta\text{-Al}_2\text{O}_3$, whereas SC-FA-G2 comprises of Fe_3O_4 and Al_2O_3 .
- From XRD analysis of SC-FA-S1 and SC-FA-S2, synthesized by solution combustion method using 50 % of stoichiometric and stoichiometric amount of sucrose as a fuel developed amorphous structure respectively.
- In addition, XRD analysis of SC-FA-U2-H, SC-FA-G2-H and SC-FA-S2-H, synthesized by solution combustion method using stoichiometric amount of urea, glycine and sucrose fuel, respectively, calcined and then reduced under hydrogen atmosphere, showed that all the samples have $\alpha\text{-Al}_2\text{O}_3$ and Fe formation.
- Magnetic attraction of synthesized samples was checked by commercially available neodymium magnet (NdFeB). Upon checking, the samples of SC-FA-U2, SA-FA-U2-H, SC-FA-G1, SC-FA-G2, SA-FA-G2-H, SA-FA-S2-H and SA-FA-S2-H showed that they have magnetic attraction.
- According to SEM images, nanosize composites were synthesized by solution combustion method. However, the sample synthesized using glycine as fuel have narrow range of particle distribution and porous morphology compared to other synthesized samples. SEM images of SC-FA-G2 showed smaller particle sizes at around 200 nm.
- SC-FA-U2-H, SC-FA-G2-H and SC-FA-S2-H samples were found to have 50 % of Fe by weight.
- From SEM-EDS analysis of SC-FA-U2-H, SC-FA-G2-H and SC-FA-S2-H, the samples were found to have 59.2, 60.08 and 46.6 % of Fe by weight, respectively.
- The results obtained from TG/DTA analyses of synthesized samples were also confirmed by XRD analysis. However, mass gain was observed at the samples synthesized using urea and glycine as fuel. The mass gain is thought to be the result of oxidation of the particles, and this could be investigated with further studies.
- From surface area and porosity analysis of SC-FA-G2 synthesized by solution combustion method using stoichiometric amount of glycine, it was found that the

sample has 19.6956 m²/g BET surface area. Zhang et al. (2012) [81] in their study also synthesized iron based magnetic aluminium oxide composites by solution combustion method using urea as fuel and they found that the sample has 4.01 m²/g BET surface area. This is the only study related with the present study found in the literature so far. The main difference between two studies is the fuel type used during the synthesis. BET surface area and porosity analysis of the present study (glycine used as fuel) and the results of Zhang et al. (2012) [81] (urea used as fuel) were given in Table 9.2.

Table 10.1 Comparison of BET surface area and porosity analysis between the present study and Zhang et al.2012 [81]

Specifications	The present study	Zhang et al. 2012
S_{BET} (m²/g)	19.6956	4.0100
Pore volume_(BJH adsorption) (cm³/g)	0.06932	0.03260
Pore volume_(BJH desorption) (cm³/g)	0.07188	-
V_{micropore} (cm³/g)	0.00234	-
Pore size_(BJH adsorption) (nm)	18.7428	64.76
Pore size_(BJH desorption) (nm)	14.8318	-
Average particle size (nm)	304.6369	-

Adsorption Studies of RB19 Dye Removal onto Iron Based Magnetic Aluminium Oxide Nanocomposites:

- After evaluation the data obtained from the characterization studies, SC-FA-G2 was chosen as an adsorbent for Reactive Blue 19 dye removal by adsorption. The Design Expert 11.0 experimental design programme was used to plan the experimental set by Response Surface Methodology. As a result, 17 experiments were carried out under process conditions of pH (2, 4 and 6), temperature (25, 35 and 45 °C) and adsorbent amounts (200, 300 and 400 mg/50 mL) to investigate their effects on the adsorption process.
- The maximum RB19 dye removal (%100) was observed under conditions as follows; pH of 2, 25 °C and 400 mg SC-FA-G2/50 mL (Table 10.3).

- The quadratic model was found using Box-Behnken design method explaining the relationship between the process parameter and process response. The model developed was given as follows;

$$Y_{\text{SC-FA-G2}} = - 21.00*X_1 + 5.38*X_2 + 22.38*X_3 + 6.25*X_1*X_2 + 15.75*X_1*X_3 - 1.50*X_2*X_3 + 12.00*X_1^2 + 1.25*X_2^2 + 3.75*X_3^2 + 63.00 \quad (9.1)$$

- The pH and adsorbent amount were found to be the most effective parameters on RB19 dye removal. But, the effect of temperature was found insignificant on RB19 dye removal.
- After evaluation of the data obtained from adsorption experiments of RB19 dye onto SC-FA-G2, among the adsorption isotherm models examined, the Langmuir adsorption isotherm model was found as the most appropriate model with higher value of correlation coefficient ($R^2= 0.9956$) and lower value of standard deviation ($\sigma= 0.0275$). The maximum adsorption capacity value (Q_{max}) of SC-FA-G2 was calculated as 55.248 mg/g.
- After evaluation of the data obtained from adsorption experiments of RB19 dye onto SC-FA-G2, among the adsorption kinetic models examined, the Pseudo-second order kinetic model was found as the most appropriate model with higher value of correlation coefficient ($R^2= 0.9999$) and lower value of standard deviation ($\sigma= 0.0045$).

Table 10.1 Present study on synthesis of aluminium oxide nanoparticles by solution combustion method

Reference	Starting Materials		Stoich. fuel (%)	Combustion Reaction Parameters			Calcination Temp. (°C)	Characterization studies	
	Oxidizer	Fuel		Heating System	Temp. / Power	Time (min)		XRD Analysis	Particle Size ^(a) (nm)
Present study (2018)	Al(NO ₃) ₃	Urea	50	Hot plate	400 °C	-	1000	α-Al ₂ O ₃	151 - 735
			100	Hot plate	400 °C	-	1000	α-Al ₂ O ₃	100 - 300
		Glycine	50	Hot plate	400 °C	-	1000	θ-Al ₂ O ₃	-
			100	Hot plate	400 °C	-	1000	γ-Al ₂ O ₃	143 - 303

^(a) Particle size according to SEM images.

Table 10.2 Present study on synthesis of iron based magnetic aluminium oxide nanocomposites by solution combustion method

Reference	Starting Materials		Stoich. fuel (%)	Combustion Reaction Parameters			Calcination Temp. (°C)	Characterization studies		
	Oxidizer	Fuel		Heating System	Temp. / Power	Time (min)		XRD Analysis	Particle Size ^(a) (nm)	
Present study (2018)	Al(NO ₃) ₃	Urea	50	Hot plate	400 °C	-	-	-	-	
			100	Hot plate	400 °C	-	-	Al ₂ O ₃ , Fe ₃ O ₄	-	
			100	Hot plate	400 °C	-	1000 ^(b)	Fe, α-Al ₂ O ₃	~200	
		Glycine	50	Hot plate	400 °C	-	-	-	θ-Al ₂ O ₃ , Fe ₃ O ₄	-
			100	Hot plate	400 °C	-	-	-	Al ₂ O ₃ , Fe ₃ O ₄ .	-
			100	Hot plate	400 °C	-	1000 ^(b)	Fe, α-Al ₂ O ₃	~200	
		Sucrose	50	Hot plate	400 °C	-	-	-	-	-
			100	Hot plate	400 °C	-	-	-	-	-
			100	Hot plate	400 °C	-	1000 ^(b)	Fe, α-Al ₂ O ₃	~200	

^(a) Particle size according to SEM images.

^(b) Calcined and then reduced under hydrogen atmosphere



Table 10.3 Present study on the adsorption of Reactive Blue 19 dye

References	Adsorbent	Optimum Conditions						Adsorption Isotherm Model	Adsorption Kinetic Model
		Adsorbent Amount (g/L)	Initial Dye Conc. (mg/L)	Time (min)	Temp. (°C)	pH	Removal (%)		
Present study (2018)	SC-FA-G2	8	100	60	25	2	100	Langmuir	Pseudo-second order
		8			45				
		12			35				

To sum up, in the present study, aluminium oxide nanoparticles and iron based magnetic aluminium oxide nanocomposites were synthesized successfully by solution combustion method, as an easy and favourable method compared to the other synthesis methods, using various fuel types and fuel amounts. According to the literature survey, there is no documentation was found about usage of glycine as fuel for the synthesis of iron based magnetic aluminium oxide nanocomposites by solution combustion method. Moreover, no study was found about usage of iron based magnetic aluminium oxide nanocomposites for RB19 dye removal from aqueous solutions. According to data obtained, the maximum RB19 dye removal (%100) was observed at pH of 2, 25 °C and 400 mg SC-FA-G2/50 mL. The maximum adsorption capacity value (Q_{max}) was calculated as 55.248 mg/g.

Future Work

- Aluminium oxide nanoparticles and iron based magnetic aluminium oxide nanocomposites can be synthesized by solution combustion method using various fuel types, amounts or combinations. A study can be carried out to characterize these synthesized nanosize materials for their chemical structure, particle size, porosity and etc.
- Iron based magnetic nanocomposites synthesized by solution combustion method using stoichiometric amount of glycine as fuel, can be used removal of pesticides, heavy metals or other environmental pollutants from aqueous solutions.
- On the other hand, iron based magnetic nanocomposites could be utilized in various application areas such as biotechnology, especially for drug delivery systems and etc.

REFERENCES

- [1] Manivasakan, P., (2014). Synthesis of Al₂O₃, ZrO₂, TiO₂ nanoparticles from natural minerals for industrial applications, Ph.D Thesis, Anna University of Technology, Coimbatore.
- [2] Lashanizadegan, M., Farz, G., Nasrin, E. N., (2014). "Synthesis and surface modification of aluminum oxide nanoparticles", Journal of Ceramic Processing Research, 5:316-319.
- [3] Song, X., Qu, P., Yang, H. P., He, X., Oui, G. Z., (2005). "Synthesis of γ -Al₂O₃ nanoparticles by chemical precipitation method", Journal of Central South University of Technology, 12(5):536-541.
- [4] Karakassides, M. A., Gournis, D., Bourlinos, A. B., Pantelis N. T., Thomas, B., (2003). "Magnetic Fe₂O₃-Al₂O₃ composites prepared by a modified wet impregnation method", Journal of Materials Chemistry, 13:871-876,
- [5] Munoz, M., Pedro, Z. M., Menendez, N., Casasa J. A., Rodriguez, J. J., (2013). "A ferromagnetic γ -alumina-supported iron catalyst for CWPO. Application to chlorophenols", Applied Catalysis B: Environmental, 136(137):218-224.
- [6] Sahu D. and Madhushree, (2012). Synthesis and characterisation of alumina-iron oxide mixed nanocomposite for removal of Congo red dye, Master of Science in Chemistry, National Institute of Technology, Department of Chemistry, Rourkela.
- [7] Chu, W., (2001). "Dye removal from textile dye wastewater using recycled alum sludge", Water Research, 35(13):3147-3152.
- [8] Crini, G., (2006). "Non-conventional low-cost adsorbents for dye removal: a review", Bioresource technology, 97(9):1061-1085.
- [9] Mimani, T. and Patil, K. C., (2001). "Solution combustion synthesis of nanoscale oxides and their composites", Materials Chemistry and Physics, 4:134-137.
- [10] Varma A., Mukasyan, A. S., Rogachev A. S., Manukyan, K. V., (2016). "Solution Combustion Synthesis of Nanoscale Materials", Chemical reviews, 116(23):14493-14586.
- [11] Ghorbani, H. R., (2014). "A Review of Methods for Synthesis of Al Nanoparticles", Oriental Journal of Chemistry, 30(4):1941-1949.

- [12] Haq S., and Raval, R., (2007). “NO and dichloroethene reactivity on single crystal and supported Cu nanoparticles: just how big is the materials gap”, *Physical Chemistry Chemical Physics*, 9:3641-3647.
- [13] Alivisatos, A. P., (1996). “Perspectives on the Physical Chemistry of Semiconductor Nanocrystals”, *The Journal of Physical Chemistry*, 100:13226-13239.
- [14] Nguyen, H. L., Nguyen, H. N., Nguyen, H. H., Luu M. Q., Nguyen, M. H., (2015). “Nanoparticles: synthesis and applications in life science and environmental technology”, *Advances in Natural Sciences: Nanoscience and Nanotechnology*, 6:1-9.
- [15] Djerdj, I., Arcon, D., Jaglicic Z., Niederberger, M., (2008). “Nonaqueous synthesis of metal oxide nanoparticles: Short review and doped titanium dioxide as case study for the preparation of transition metal-doped oxide nanoparticles”, *Journal of Solid State Chemistry*, 181:1571– 1581.
- [16] Oskam, G., (2006). “Metal oxide nanoparticles: synthesis, characterization and application”, *Journal of Sol-Gel Science and Technology*, 37, 161–164.
- [17] Piriya Wong, V., Thongpool, V., Asanithi P., Limsuwan, P., (2012). “Preparation and Characterization of Alumina Nanoparticles in Deionized Water Using Laser Ablation Technique”, *Journal of Nanomaterials*, 1-6.
- [18] Lateef, A., and Nazir, R., (2017). “Metal Nanocomposites: Synthesis, Characterization and their Applications”, *Science and applications of Tailored Nanostructures*, 239-256.
- [19] Introduction of Nanoscience, Study Guide,
<http://www.nanoscienceworks.org/publications/books/4/9781420048056/ITNS-STUDYGUIDE-Chap4-Fabrication.pdf>, 06.02.2018.
- [20] Raab, C., Simkó, M., Fiedeler, U., Nentwich, M., Gzásó, A., (2011). “Production of nanoparticles and nanomaterials”, *NanoTrust-Dossier*, 6:1-4.
- [21] Parida, K., Pradhan, A. C., Das, J., Sahu, N., (2009). “Synthesis and characterization of nano-sized porous gamma-alumina by control precipitation method”, *Materials Chemistry and Physics*, 113:244–248.
- [22] Banerjee, S., (2016). “Alumina Nanoparticles and Alumina-Based Adsorbents for Wastewater Treatment”, *Nanomaterials for Wastewater Remediation*, 239-272.
- [23] Poursani, A. S., Nilchi, A., Hassani, A. H., Shariat M., Nouri, J., (2015). “A novel method for synthesis of nano- γ -Al₂O₃: study of adsorption behavior of chromium, nickel, cadmium and lead ions”, *International Journal of Environmental Science and Technology*, 12(6):2003–2014.
- [24] Suchanek, W. L., (2010). “Hydrothermal Synthesis of Alpha Alumina (α -Al₂O₃) Powders: Study of the Processing Variables and Growth Mechanisms”, *Journal of the American Ceramic Society*, 2:399–412.

- [25] Zhou, J., Wang, L., Zhang, Z., Yu, J., (2013). “Facile synthesis of alumina hollow microspheres via trisodium citrate-mediated hydrothermal process and their adsorption performances for p-nitrophenol from aqueous solutions”, *Journal of Colloid and Interface Science*, 394:509–514.
- [26] Afre, R. A., Soga, T., Jimbo, T., Kumar, M., Ando, Y., Sharon, M., Somani, P. R., Umeno, M., (2006). “Carbon nanotubes by spray pyrolysis of turpentine oil at different temperatures and their studies”, *Microporous and Mesoporous Materials*, 96:184–190.
- [27] Alves, A., Bergmann, C. P., Berutti, F. A., (2013). *Novel Synthesis and Characterization of Nanostructured Materials*, Springer-Verlag, Berlin Heidelberg.
- [28] Jadhav, L., Patil, S., Chavan, A., Jamale, A., Puri, V., (2011). “Solution combustion synthesis of Cu nanoparticles: a role of oxidant-to-fuel ratio”, *The Institution of Engineering and Technology*, 6(9):812-815.
- [29] Singanahally, T. A., and Alexander, S. M., (2008). “Combustion synthesis and nanomaterials”, *Current Opinion in Solid State and Materials Science*, 12:44-50.
- [30] Dey, S., “Synthesis and Application of γ -Alumina Nanopowders, Master of Science in Chemistry, National Institute of Technology, Department of Chemistry, Rourkela.
- [31] Doğan, İ., (2008). *Fabrication and Characterization of Aluminum Oxide and Silicon/Aluminum Oxide Films with Si Nanocrystals Formed by Magnetron Co-Sputtering Technique*, The degree of Master of Science in Physics, Middle East Technical University, The Graduate School of Natural and Applied Sciences, Ankara.
- [32] Shirai, T., Watanabe, H., Fuji M., Takahashi, M., (2009). “Structural Properties and Surface Characteristics on Aluminum Oxide Powders”, *Ceramics Research Lab*, 9:23-31.
- [33] Aswad, M. A., (2012). *Residual Stress and Fracture in High Temperature Ceramics*, Doctor of Philosophy, The University of Manchester, Faculty of Engineering and Physical Sciences, Manchester.
- [34] Kamboj, N. K., (2016). *The template-assisted wet-combustion synthesis of mesoporous core-shell structured materials*, Master Thesis, Tallinn University of Technology, Materials and Processes of Sustainable Energetics, Tallinn.
- [35] Halim, N. H. A., (2009). *Synthesis of Mesoporous Alumina Nanoparticle Using Agarose Template for Lewis Acid Catalyst*, Universiti Teknologi Malaysia.
- [36] SkySpring I., (2016). *Nanomaterials, Aluminum Oxide Nanoparticles/Nanopowder*, http://ssnano.com/inc/sdetail/aluminum_oxide_nanoparticles_nanopowder__alumina__alpha_al2o3__99_9__50_nm_/397, 06.02.2018.
- [37] Gupta, A., (2016). *Aluminium-Aluminum Nanoparticles*, <https://www.nanoshel.com/aluminium-aluminum-nanoparticles/>, 04.02.2018.

- [38] AZoNano, Aluminium/Aluminum Nanoparticles - Properties, Applications, <https://www.azonano.com/article.aspx?ArticleID=3257>, 08.02.2018.
- [39] Kudr, J., Haddad, Y., Richtera, L., Cernak, M., Adam V., Zitka, O., (2017). "Magnetic Nanoparticles: From Design and Synthesis to Real World Applications", *Nanomaterials*, 7(243):1-29.
- [40] Drbohlavova, J., Hrdy, R., Adam, V., Kizek, R., Schneeweiss, O., Hubalek, J., (2009). "Preparation and Properties of Various Magnetic Nanoparticles", *Sensors*, 9:2352-2362.
- [41] Akbarzadeh, A., Samiei, M., Davaran, S., (2012). "Magnetic nanoparticles: preparation, physical properties, and applications in biomedicine", *Nanoscale Research Letters*, 7(144):1-13.
- [42] Mohammed, L., Gomaa, H. G., Ragab, D., Zhu, J., (2017). "Magnetic nanoparticles for environmental and biomedical applications: A review", *Particuology*, 30:1-14.
- [43] Behrens, S. and Appel, I., (2016). "Magnetic nanocomposites", *Nanobiotechnology*, 39:89-96.
- [44] Gupta, P., Kumar, D., Quraishi, M., Parkash, O., (2015). "Effect of Sintering Parameters on the Corrosion Characteristics of Iron-Alumina Metal Matrix Nanocomposites", *Journal of Materials and Environmental Science*, 6(1):155-167.
- [45] Huang, Y., Xue, D., Zhou, P., Maa, Y., Li, F., (2003). " α -Fe-Al₂O₃ nanocomposites prepared by sol-gel method", *Materials and Engineering A*, 359:332-337.
- [46] Liu, W., Zhong, W., Jiang, H., Tang, N., Wu, X., Du, Y., (2006). "Highly stable alumina-coated iron nanocomposites synthesized by wet chemistry method", *Surface & Coatings Technology*, 200:5170 – 5174.
- [47] Kakooei, S., Rouhi, J., Dehzangi, A., Mohammadpour, E., Alimanesh, M., "Synthesis and Characterization of Al₂O₃: Fe Nanoparticles Prepared via Aqueous Combustion", *Caspian Journal of Applied Sciences Research*, 1(12):1-7.
- [48] Kobayashi, S., Kaneko, S., Ohshima, M. A., Kurokawa, H., Miura, H. (2012). "Effect of iron oxide on isobutane dehydrogenation over Pt/Fe₂O₃-Al₂O₃ catalyst", *Applied Catalysis A: General*, 417(418):306– 312.
- [49] Peng, Y., Yi, Y., Li, L., Yi, J., Nie, J., Bao, C., (2016). "Iron-based soft magnetic composites with Al₂O₃ insulation coating produced using sol-gel method", *Materials and Design*, 109:390–395.
- [50] Pattanayak, B. C., (2010). Synthesis and Characterization of Alumina/Iron Oxide Mixed Nanocomposite, Master of Science in Chemistry, National Institute of Technology, Department of Chemistry, Rourkela.
- [51] Worch, E., (2012). Adsorption Technology in Water Treatment, Walter de Gruyter GmbH & Co. KG, Dresden.

- [52] Salleh, M. A. M., Mahmoud, D. K., Karim W. A. W. A., Idris, A., (2011). "Cationic and anionic dye adsorption by agricultural solid wastes: A comprehensive review", *Desalination*, 280:1–13.
- [53] Zdravkov, B. D., Cermak, J. J., Sefara, M., Jank, J., (2007). "Pore classification in the characterization of porous materials: A perspective", *Central European Journal of Chemistry*, 5(2):385–395.
- [54] Dubinin, M., (1979). "Micropore structures of charcoal adsorbents. 1. A general characterization of micro- and supermicropores in the fissure model", *Proc. Acad. Sci USSR*, 8:691–1696.
- [55] Cheremskoj, P., (1985). *Metodi izsledovania poresti tvurdi tel.*, Energoatomizdat, Russian.
- [56] Kodikara, J., Barbour, S., Fredlund, D., (1999). "Changes in clay structure and behaviour due to wetting and drying", *Proceedings 8th Australia New Zealand Conference on Geomechanics: Consolidating Knowledge*, 179-185.
- [57] Králik, M., (2014). "Adsorption, chemisorption, and catalysis", *Chemical Papers*, 68, (12):1625–1638.
- [58] Arıkan, S., (2016). *Investigation Of Arsenic Adsorption Performance of The Modified Natural Materials*, Degree of Doctor of Philosophy, Dokuz Eylül University, Graduate School of Natural And Applied Sciences, İzmir.
- [59] Rouquerol, F., Rouquerol, J., Sing, K. S., Maurin, G., Llewellyn, P., (2013). *Adsorption by Powders and Porous Solids: Principles, Methodology and Applications*, Academic Press, France.
- [60] Sing, K. S. W., Everett, D. H., Haul, R. A. W., Moscou, L., Pierotti, R. A., Rouquerol, J., Siemieniewska, T., (1985). "Reporting physisorption data for gas/solid systems - with special reference to the determination of surface area and porosity", *International Union of Pure and Applied Chemistry*, 57(4):603-619.
- [61] Yang, C., (1998). "Statistical mechanical study on the freundlich isotherm equation", *Journal of Colloid Interface Science*, 208(2)379-387.
- [62] Foo, K. and Hameed, B., (2010). "Insights into the modeling of adsorption isotherm systems", *Chemical Engineering Journal*, 156:2–10.
- [63] Ramachandran, P., Vairamuthu, R., Ponnusamy, S., (2011). "Adsorption Isotherms, Kinetics, Thermodynamics and Desorption Studies of Reactive Orange 16 on Activated Carbon Derived from Ananas Comosus (L.) Carbon", *ARNP Journal of Engineering and Applied Sciences*, 6(11):15-26.
- [64] Allen, S. J., and Koumanova, B., (2005). "Decolourisation of Water/Wastewater Using Adsorption", *Journal of the University of Chemical Technology and Metallurgy*, 40(3):175-192.
- [65] Nandi, B., Goswami, A., Purkait, M. (2009). "Adsorption characteristics of brilliant green dye on kaolin", *Journal of Hazardous Materials*, 161:387-395.

- [66] Bevilacqua, A., Corbo1, M.R., Sinigaglia, M. (2010). “Design of experiments: a powerful tool in food microbiology”, *Current Research, Technology and Education Topics in Applied Microbiology and Microbial Biotechnology*, 1419-1429.
- [67] Mäkelä, M., (2017). “Experimental design and response surface methodology in energy applications: A tutorial review”, *Energy Conversion and Management*, 151:630-640.
- [68] Ravikumara, K., Pakshirajanb, K., Swaminathanc, T. (2005). “Optimization of Batch Process Parameters Using Response Surface Methodology for Dye Removal by A Novel Adsorbent”, *Chemical Engineering Journal*, 105:131-138.
- [69] Wang, J., Wan, W., (2009). “Experimental design methods for fermentative hydrogen production: A review”, *International Journal of Hydrogen Energy*, 34:235-244.
- [70] Design of Experiment (DOE),
<https://www.moresteam.com/toolbox/design-of-experiments.cfm>, 02.05.2018.
- [71] Aslan, N., and Cebeci, Y. (2007). “Application of Box–Behnken design and response surface methodology for modeling of some Turkish coals”, *Fuel*, 86:90-97.
- [72] Fazli, M., Tafreshi, M. J., Bustan Afruz, F., Rahmani, A., (2016). “Fuel effects on properties of alumina nanoparticles synthesized by combustion technique”, *Indian Journal of Pure & Applied Physics*, 54: 406-410.
- [73] Farahmandjou, M. and Golabiyani, N. (2015). “Solution Combustion Preparation of Nano-Al₂O₃: Synthesis and Characterization”, *Trans. Phenom. Nano Micro Scales*, 3(2):100-105.
- [74] Sharma, A., Rani, A., Singh, A., Modi O. P., Gupta, G. K., (2014). “Synthesis of alumina powder by the urea–glycine–nitrate combustion process: a mixed fuel approach to nanoscale metal oxides”, *Applied Nanoscience*, 4:315–323.
- [75] Ramesh, G., Mangalaraja, R. V., Ananthakumar, S. Manohar, P., (2013). “Influence of fuel in the microwave assisted combustion synthesis of nano α -alumina powder”, *International Journal of Physical Sciences*, 8(34):1729-1737.
- [76] Sherikar, B. N., and Umarji, A. M., (2013). “Synthesis of γ -Alumina by Solution Combustion Method using Mixed Fuel Approach (Urea+Glycine Fuel)”, *International Journal of Research in Engineering and Technology*, 434-438.
- [77] Sharma, A., Modi, O. P., Gupta, G. K., (2012). “Effect of fuel to oxidizer ratio on synthesis of Alumina powder using Solution Combustion Technique- Aluminium Nitrate & Glycine combination”, *Advances in Applied Science Research*, 3(4):2151-2158.
- [78] Moreno-Marcelino, J. E., Granados-Correa, F., Pfeiffer, H., Bulbulian, S., (2012). “Synthesis of MgO, ZnO and Al₂O₃ by Solid and Solution Combustion Processes and Study of Their Performances in Co²⁺ Uptake”, *Ceramics-Silikáty*, 56(3):254-260.

- [79] Saket, S., Rasouli, S., Ghasemi, E., Tahmasebi, K., (2010). "Solution Combustion Synthesis of Nano-Crystalline Alumina Powders", *Journal of Materials Science and Engineering*, 4(8):80-84.
- [80] Freitas, N. L., Fagury-Neto, E., Lira, H. L., Gama, L., Kiminami, R. H. G. A., Costa, A. C. F. M., (2006). "Combustion Synthesis of α -Al₂O₃ Powders", *Materials Science Forum Vols. 530-531*:631-636.
- [81] Zhang, J., Guo, Q., Liu, Y., Cheng, Y., (2012). "Preparation and Characterization of Fe₂O₃/Al₂O₃ using the Solution Combustion Approach for Chemical Looping Combustion", *Industrial & Engineering Chemistry Research*, 51:12773–12781.
- [82] Wang, B., Yan, R., Lee, D. H., Zhenga, Y., Zhao, H., Zheng, C., (2011). "Characterization and evaluation of Fe₂O₃/Al₂O₃ oxygen carrier prepared by sol-gel combustion synthesis", *Journal of Analytical and Applied Pyrolysis*, 91:105-113.
- [83] Xu, B., Zheng, H., Zhou, H., Wang, Y., Luo, K., Zhao, C., Peng, Y., Zheng, X., (2018). "Adsorptive removal of anionic dyes by chitosan-based magnetic microspheres with pH-responsive properties", *Journal of Molecular Liquids*, 256: 424-432.
- [84] Mustafa, M. M., Jamal, P., Alkhatib, M. F., Mahmod, S. S., Jimat, D. N., Ilyas, N. N., (2017). "Panus tigrinus as a potential biomass source for Reactive Blue decolorization: Isotherm and kinetic study", *Electronic Journal of Biotechnology*, 26:7-11.
- [85] Demirhan, E., (2017). "Removal of Reactive Blue 19 From Aqueous Solution by Peanut Shell: Optimization by Response Surface Methodology", *Selcuk Univ. J. Eng. Sci. Tech*, 5(3):312-321.
- [86] Mousa, K. M., and Taha, A. H., (2016). "Adsorption of Reactive Blue Dye onto Natural and Modified Wheat Straw", *American Journal of Chemical Engineering*, 4(1):9-15.
- [87] Ciobanu, G., Barna, S., Harja, M., (2016). "Kinetic and equilibrium studies on adsorption of Reactive Blue 19 dye from aqueous solutions by nanohydroxyapatite adsorben", *Archives of Environmental Protection*, 42(2):3-11.
- [88] El-Bindary, A., Abd El-Kawi, M., Hafez, A., Rashed, I., Aboelnaga, E., (2016). "Removal of reactive blue 19 from aqueous solution using rice straw fly ash", *Journal of Materials and Environmental Science*, 7(3):1023-1036.
- [89] Balaraka, D., Mahdavib, Y. Joghataeic, A., (2015). "The Application of Low-Cost Adsorbent for Reactive Blue 19 Dye Removal from Aqueous Solution: Lemna Minor", *Archives of Hygiene Sciences*, 4(4):199-207.
- [90] Dehvari, M., Ghaneian, M. T., Ebrahimi, A., Jamshidi, B., Mootab, M., (2015). "Removal of reactive blue 19 dyes from textile wastewater by pomegranate seed powder: Isotherm and kinetic studies", *International Journal of Environmental Health Engineering*, 4(4):1-9.

- [91] Khoshhesab, Z. M. and Ahmadi, M., (2015). "Removal of reactive blue 19 from aqueous solutions using NiO nanoparticles: equilibrium and kinetic studie", *Desalination and Water Treatment*, 1-12.
- [92] Ghaneian, M. T., Ehrampou, M. H., Sahlabadi, F., Mootab, M., Rezapour, I., Jasemizad, T., (2014). "Reactive Blue 19 Dye Adsorption Behavior on Jujube Stems Powder from Synthetic Textile Wastewater: Isotherm and Kinetic Adsorption Studies", *Journal of Community Health Research*, 3(1):67-78.
- [93] Nguyen, V. C., and Pho, Q. H., (2014). "Preparation of Chitosan Coated Magnetic Hydroxyapatite Nanoparticles and Application for Adsorption of Reactive Blue 19 and Ni²⁺ Ions", *The Scientific World Journal*, 1-9.
- [94] Rafiee, M., and Jahangiri-rad, M., (2014). "Adsorption of Reactive Blue 19 from Aqueous Solution by Carbon Nano Tubes: Equilibrium, Thermodynamics and Kinetic Studies", *Research Journal of Environmental Sciences*, 8(4):205-214.
- [95] Radaei, E., Moghaddam, M. R. A., Arami, M., (2014). "Removal of reactive blue 19 from aqueous solution by pomegranate residual-based activated carbon: optimization by response surface methodology", *Journal of Environmental Health Science & Engineering*, 12(65):1-8.
- [96] Asgher, M., and Bhatti, H. N., (2012). "Removal of Reactive Blue 19 and Reactive Blue 49 Textile Dyes by Citrus Waste Biomass From Aqueous Solution: Equilibrium and Kinetic Study", *The Canadian Journal of Chemical Engineering*, 90:412-419.
- [97] Ahmed, S. A. S., Khalil, L. B., El-Nabarawy, T., (2012). "Removal of Reactive Blue 19 dye from Aqueous Solution Using Natural and Modified Orange Peel", *Carbon Letters*, 13(4):212-220.
- [98] Wieczorek-Ciurowa, K., and Kozak, A. J., (1999). "The Thermal Decomposition of Fe(NO₃)₃.9H₂O", *Journal of Thermal Analysis and Calorimetry*, 58:647-651.
- [99] Huang, K. L., Yin, L. G., Liu, S. Q., Li, C. J., (2007). "Preparation and formation mechanism of Al₂O₃ nanoparticles by reverse microemulsion", *Trans. Nonferrous Met. Soc. China*, 17:633-637.
- [100] Lucio-Ortiz, C. J., Rosa, J. R. D., Ramirez, A. H., Heredia, J. A. D. I. R., Angel, P. D., Munoz-Aguirre, S., Leon-Covian, L. M. D., (2011). "Synthesis and characterization of Fe doped mesoporous Al₂O₃ by sol-gel method and its use in trichloroethylene combustion", *Journal of Sol-Gel Science and Technology*, 58:374-384.
- [101] Rogoan, R., Andronescu, E., Ghițulică, C., Vasile, B. Ș., (2011). "Synthesis and Characterization of Alumina Nano-Powder Obtained by Sol-Gel Method", 73(2):69-76.
- [102] Maldonado, C. S., Rosa, J. R. D., Lucio-Ortiz, C. J., Hernández-Ramírez, A., Barraza, F. F. C., Valente, J. S., (2014). "Low Concentration Fe-Doped Alumina Catalysts Using Sol-Gel and Impregnation Methods: The Synthesis, Characterization and Catalytic Performance during the Combustion of

Trichloroethylene”, *Materials*, 7:2062-2086.

- [103] Kalska-Szostko, B., Wykowska, U., Satula D., Nordblad, P., (2015). “Thermal treatment of magnetite nanoparticles”, *Beilstein Journal of Nanotechnology*, 6:1385–1396.
- [104] Prasad, S. V. S., and Rao, V. S., (1984). “Thermal transformation of iron (III) oxide hydrate gel”, *Journal of Materials Science*, 19:3266-3270.
- [105] Alothman, Z. A., (2012). “A Review: Fundamental Aspects of Silicate Mesoporous Materials”, *Materials*, 5:2874-2902.
- [106] Mourabet, M., El Rhilassi, A., Boujaady, H. E., Bennani-Ziatni, M., Taitai, A., (2017). “Use of response surface methodology for optimization of fluoride adsorption in an aqueous solution by Brushite”, *Arabian Journal of Chemistry*, 10:3292–3302.



SCANNING ELECTRON MICROSCOPY IMAGES

The SEM microscopy images of synthesized samples such as SC-FA-U1, SC-FA-U2, SC-FA-G1, SC-FA-G2, SC-FA-S1 and SC-FA-S2 were given in Figure A.1-A.6.

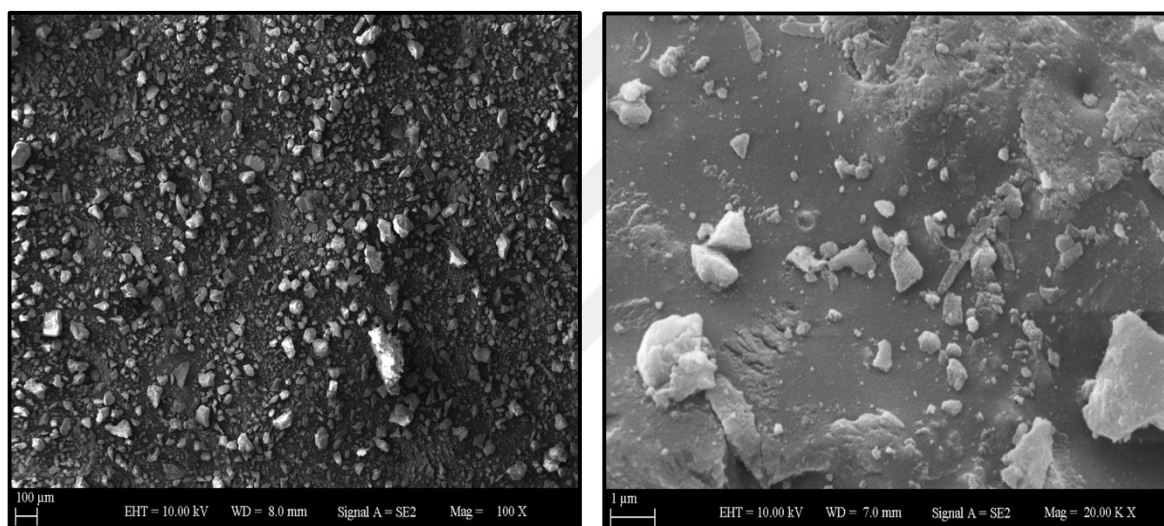


Figure A.1 SEM microscopy images of SC-FA-U1

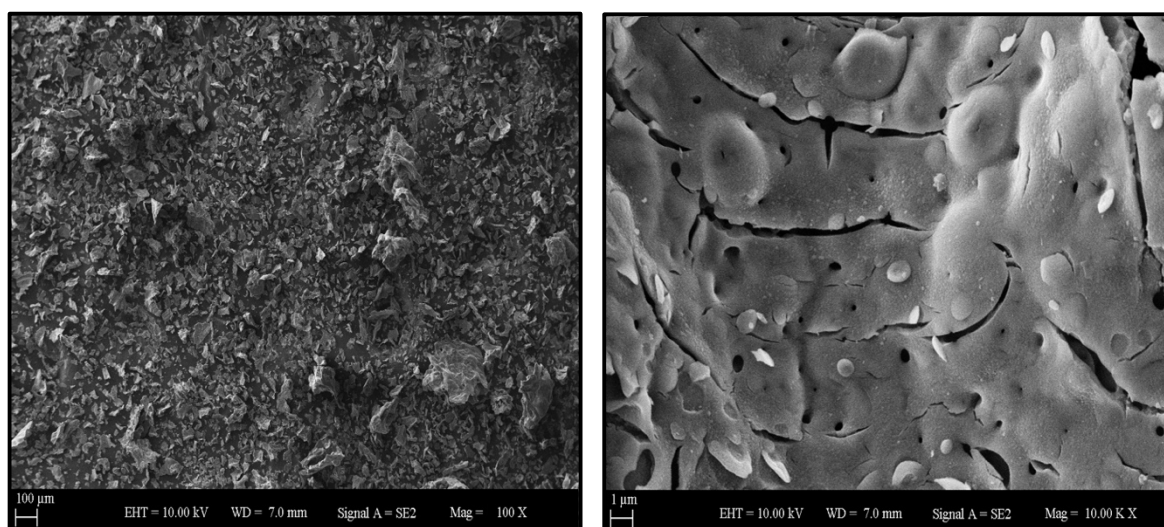


Figure A.2 SEM microscopy images of SC-FA-U2

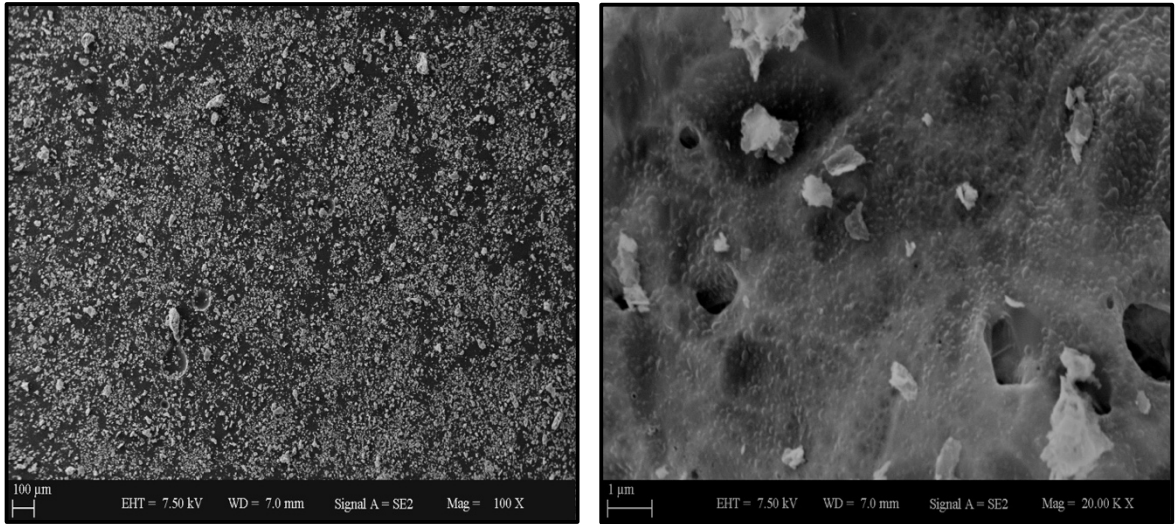


Figure A.3 SEM microscopy images of SC-FA-G1

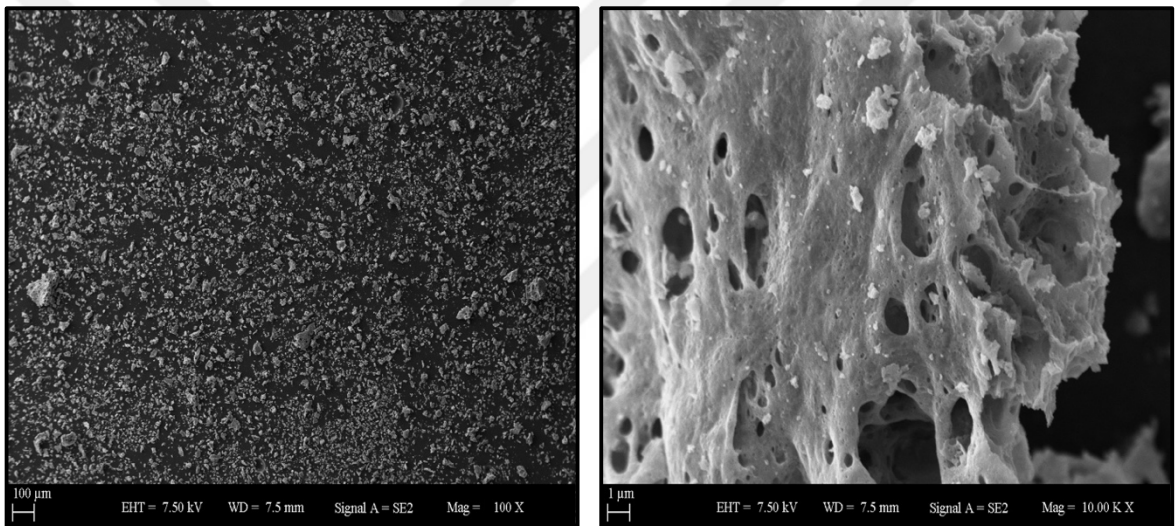


Figure A.4 SEM microscopy images of SC-FA-G2

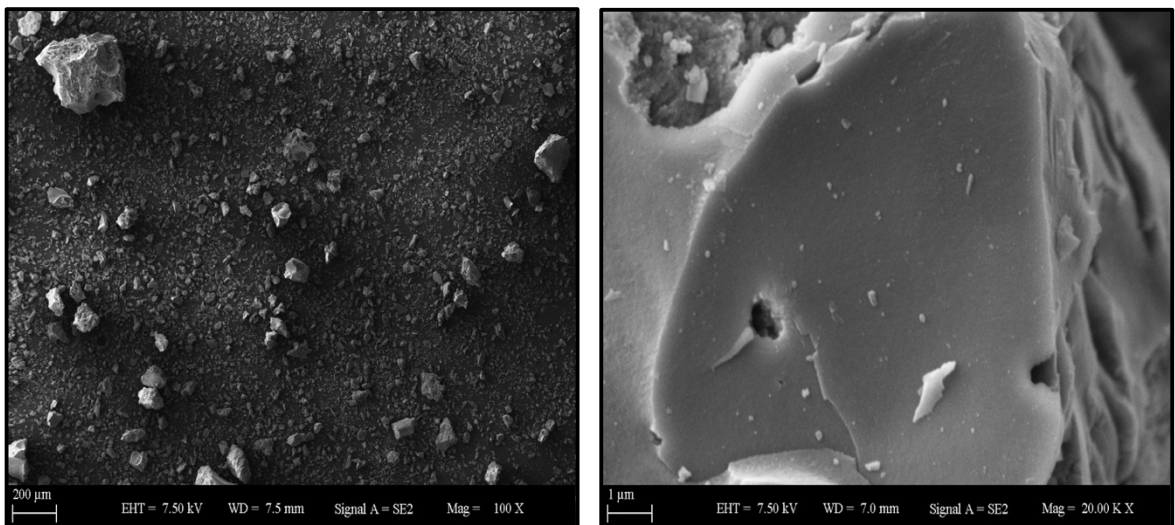


Figure A.5 SEM microscopy images of SC-FA-S1

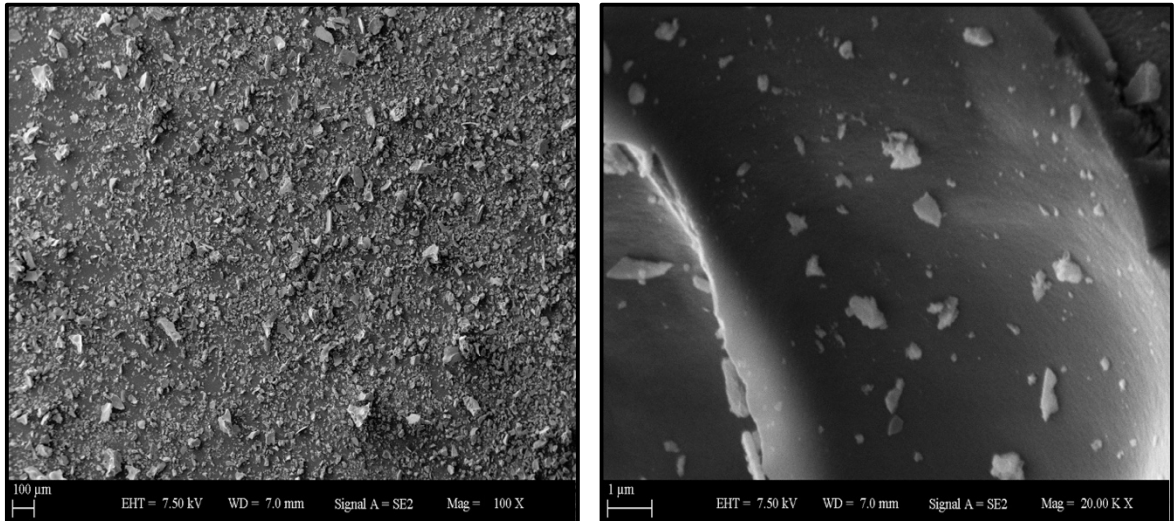


Figure A.6 SEM microscopy images of SC-FA-S2



APPENDIX-B

DATA OF ADSORPTION ISOTHERM MODELS

The data obtained from adsorption experiments of RB19 dye onto SC-FA-G2 as an adsorbent were shown in Table B.1.

Table B.1 The data obtained from adsorption experiments of RB19 dye onto SC-FA-G2

Adsorbent Amount (mg)	q_e (mg/g)	c_e (mg/L)
50	53.147	46.853
100	42.490	15.420
200	24.479	2.083
300	16.552	0.690
400	12.441	0.475

DATA OF ADSORPTION KINETIC MODELS

The data obtained from adsorption kinetic experiments of RB19 dye onto SC-FA-G2 were given in Tables C.1-C.3.

Table C.1 The data obtained from adsorption kinetic experiments of RB19 dye onto 50 mg of SC-FA-G2

t (min)	q_e (mg/g)
0	0.000
2	31.701
4	37.063
6	37.995
8	41.725
10	37.296
15	44.056
20	45.687
25	48.718
30	49.883
45	51.748
60	53.147

Table C.2 The data obtained from adsorption kinetic experiments of RB19 dye onto 200 mg of SC-FA-G2

t (min)	q_e (mg/g)
0	0.000
2	21.296
4	22.049
6	22.975
8	23.264
10	23.669
15	23.843
20	23.901
25	24.364
30	24.421
45	24.479
60	24.479

Table C.3 The data obtained from adsorption kinetic experiments of RB19 dye onto 400 mg of SC-FA-G2

t (min)	q_e (mg/g)
0	0.000
2	11.936
4	12.025
6	12.055
8	12.084
10	12.084
15	12.173
20	12.262
25	12.322
30	12.352
45	12.381
60	12.441

CURRICULUM VITAE

PERSONAL INFORMATION

Name Surname : Merve PEHLİVAN
Date of birth and place : 24.02.1993 / Istanbul
Foreign Languages : English
E-mail : mervep70@gmail.com

EDUCATION

Degree	Department	University	Date of Graduation
Master	Chemical Engineering	Yıldız Technical University	2018
Undergraduate	Chemical Engineering	Yıldız Technical University	2015
High School		Pendik Fatih Anatolian High School	2011

WORK EXPERIENCE

Year	Corporation/Institute	Enrolment
2016 -	Istanbul Gedik University, Engineering Department	TUBITAK Project Assistant

PUBLISHERMENTS

Conference Papers

1. **Pehlivan, M.,** Şimşek Kekevi, S., Özbek, S. and Özbek, B., (2018). “Characterization Study on Alumina Nanoparticles Synthesised by Solution Combustion Method”, Proceedings of Academic Conference Network (ACN) International Conference, International Conference on Environment, Agriculture and Biotechnology (ICEABT), 20 February 2018, İstanbul, Turkey.
2. **Pehlivan, M.,** Şimşek Kekevi, S., Özbek, S. and Özbek, B., (2018). “Effects of Synthesis Method on Al₂O₃ Nanoparticle Generation”, Proceedings of Academic Conference Network (ACN) International Conference, International Conference on Environment, Agriculture and Biotechnology (ICEABT), 20 February 2018, İstanbul, Turkey.
3. **Pehlivan, M.,** Şimşek Kekevi, S., Özbek, S. and Özbek, B., (2018). “Synthesis and characterization of Fe-Al₂O₃ nanoparticles by solution combustion method”, 23rd International Congress of Chemical and Process Engineering (CHISA 2018), 25-29 August 2018, Prague, Czech Republic (Accepted for oral presentation).
4. **Pehlivan, M.,** Şimşek Kekevi, S., Özbek, S. and Özbek, B., (2018). “An optimization study on the adsorption of Reactive Blue dye onto iron based magnetic alumina from aqueous solutions”, 23rd International Congress of Chemical and Process Engineering (CHISA 2018), 25-29 August 2018, Prague, Czech Republic (Accepted for poster presentation).

Projects

1. Özbek, S., Project Coordinator, “Yüksek Kaynak Özelliklerine Sahip Nanopartikül Alaşımli Özlü Kaynak Tellerinin Geliştirilmesi”, Scientific and Technological Research Council of Turkey (TUBITAK), Grant No: **International ERA.Net RUS Plus - 315M495**, (2016 – Halen).